

Title of my master thesis

Franziska Hellmuth



Thesis submitted for the degree of
Master in Meteorology
60 credits

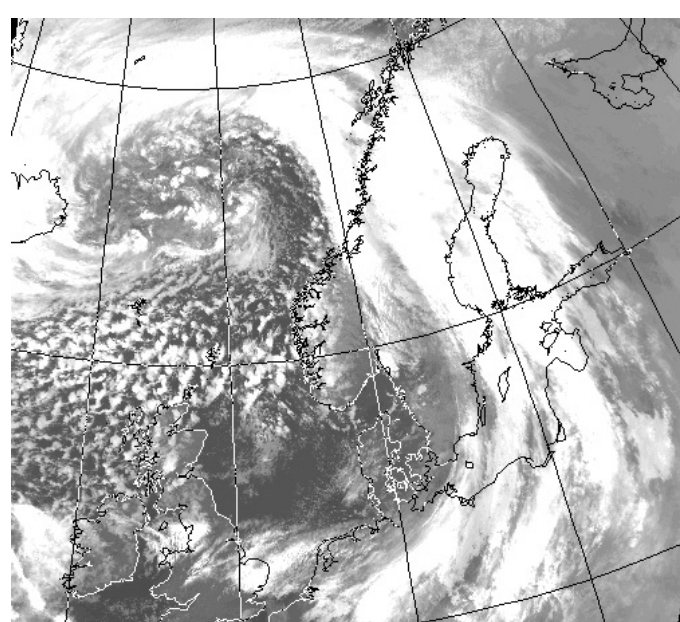
Department of Geoscience
Faculty of Mathematics and Natural Sciences

UNIVERSITY OF OSLO

Spring 2018

Title of my master thesis

Franziska Hellmuth



© 2018 Franziska Hellmuth

Title of my master thesis

<http://www.duo.uio.no/>

Printed: X-press printing house

ABSTRACT

This abstract needs to be updated.

TABLE OF CONTENTS

LIST OF ABBREVIATIONS	III
CHAPTER 1: INTRODUCTION	1
CHAPTER 2: SITE, INSTRUMENTATION, DATA, AND METHODOLOGY	4
2.1 Haukeliseter site	4
2.2 Climate at Haukeliseter	6
2.3 Instruments	7
2.3.1 Double Fence	9
2.3.2 MRR - Micro Rain Radar	10
2.3.3 PiP - Precipitation Imaging Package	13
2.3.4 MASC - Multi-Angular Snowfall Camera	14
2.4 Optimal Estimation Retrieval Algorithm	14
2.4.1 Forward model	16
2.4.2 Snowfall retrieval scheme	18
2.4.3 Presence of snow	19
2.4.4 Size distribution	21
2.4.5 Snowfall rate at the surface	22
2.5 MetCoOp Ensemble Prediction System	22
2.5.1 AROME - MetCoOP	22
2.5.2 Meso-NH and the ICE3 scheme	24
2.5.3 Adjustment of ICE3 inside MEPS	26
2.6 Numerical data transformation	27
2.6.1 Layer thickness in MEPS	27
2.6.2 Snow water content	28
2.6.3 Snow water path	29
2.6.4 Ensemble mean and Coefficient of Variation	30
2.6.5 Dew point temperature for Skew-T log-P Diagram	30

CHAPTER 3: ANALYSIS OF THE CHRISTMAS STORM 2016	31
3.1 Extreme weather	31
3.2 Dynamic Tropopause map	32
3.3 Thickness, Sea level pressure, moisture, and wind at 250 hPa	34
3.4 Atmospheric River map	38
3.5 Observations at the weather mast	40
3.6 Radiosonde from Stavanger	41
3.7 Large scale circulation	41
CHAPTER 4: RESULTS AND DISCUSSION	46
4.1 Agreement between surface observations	46
4.2 Observation of large scale weather phenomena at the surface	49
4.3 Surface snowfall accumulation	59
4.4 Observation of large scale weather phenomena in the vertical	67
4.5 Orographic influence on precipitation	73
CHAPTER 5: SUMMARY AND CONCLUSION	76
REFERENCES	77
APPENDIX A: SYNOPTIC WEATHER SITUATION	84
A.1 Skew-T log-P diagram from Stavanger	84
APPENDIX B: FORWARD MODEL	88
B.1 Scattering Model	88
APPENDIX C: RESULTS	91
C.1 48 h surface observations and MEPS forecasts	91
C.2 Mean error and mean absolute error	93
C.3 Hourly averages ensemble member zero and one	95
C.4 Vertical SWC - ensemble member 0 to 9	97

LIST OF ABBREVIATIONS

ACC	Accretion
AGG	Aggregation
AR	Atmospheric River
AROME	Applications of Research to Operations at Mesoscale
AUT	Autoconversion
BER	Bergeron-Findeisen process
C3VP	Canadian CloudSat-CALIPSO Validation Project
CFR	Contact Freezing of Raindrops
CPR	Cloud Profiling Radar
CV	Coefficient of Variation
CVM	Conversion-melting
DEP	Deposition
DRY	Dry processes
DT	Dynamic Tropopause
ECMWF	European Centre for Medium-Range Weather Forecasts
EPS	Ensemble Prediction System

FMI	Finnish Meteorological Institute
HEN	Heterogeneous Nucleation
HON	Homogeneous Nucleation
IVT	Integrated Vapour Transport
LWC	Liquid Water Content
MASC	Multi-Angular Snowfall Camera
MEPS	MetCoOp Ensemble Prediction System
Meso-NH	Mesoscale Non-Hydrostatic model
Met-Norway	Norwegian Meteorological Institute
MetCoOp	Meteorological Co-operation on Operational NWP
MLT	Melting
MRR	Micro Rain Radar
MSLP	Mean Sea Level Pressure
NWP	Numerical Weather Prediction
PIP	Precipitation Imaging Package
PSD	Particle Size distribution
RIM	Riming
SMHI	Swedish Meteorological and Hydrological Institute
SWC	Snow Water Content
SWP	Snow Water Path
WCB	Warm Conveyor Belt

WET Wet processes

WMO World Meteorological Organization

CHAPTER 1: INTRODUCTION

One of the challenges in current forecast research is the understanding and prediction of extreme weather events, such as heavy precipitation. Extreme winter storms with heavy precipitation can have large influence on the local infrastructure and the personal safety. Large amounts of precipitation combined with temperature changes can lead to danger in the Norwegian mountains. A better understanding of the microphysical processes in storms is crucial to better predict extreme storms.

Storms of this kind are expected to occur on average every five years [Olsen and Granerød, 2017].

The financial costs associated with 'Urd' are estimated to about 180 million Norwegian kroner. 'Urd' led to major traffic problems for cars, trains, ferries and air planes. Most mountain crossings were kept closed during Christmas 2016. A temperature change and therefore change of precipitation from solid to liquid followed an increase in avalanche danger. In addition, there was a power breakout of around 70.000 households and 40 emergency power stations failed during the extreme weather (Figure 1.0.1).

This Christmas storm, might not have led to the same damages as some of the extreme weather events of recent years. But since people are affected by extreme weather (Figure 1.0.1) it is important to predict storms, associated precipitation, wind, and temperature changes as accurately as possible. Having accurate observations, will lead to better performing models which rely on observations. [include a reference here](#)

Figure 1.0.1 shows that precipitation and strong winds can influence in certain ways the infrastructure. To predict and measure snowfall accumulation as accurately as possible is important since snowfall has impact on avalanches, freshwater release into water systems in spring, and extra economical expenses for local infrastructure as well as climatological effects.

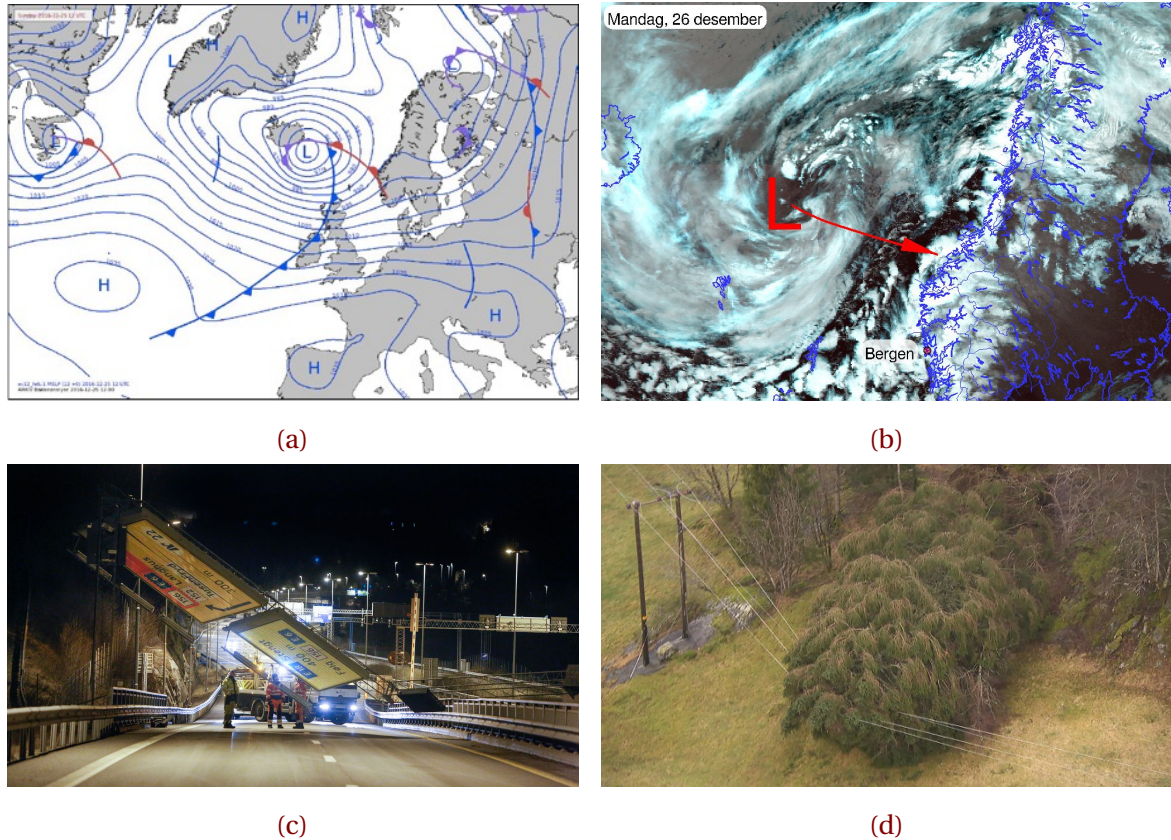


Figure 1.0.1: In **a**: Weather situation Sunday 25 December 2016 at 12 UTC, [Olsen and Granerød, 2017]. **b**: Tweet from Meteorologene [2016]: Here comes #Urd! The low pressure centre will hit Møre og Romsdal, but the strongest wind comes south of Stad. #SørNorge. **c**: This traffic sign, ten meter long and four meter high was blown down during the storm, [Ruud et al., 2016]. **d**: Trouble maker: The extreme weather during Christmas created problems for the local infrastructure. 80.000 households were without electricity during the storm, [Farestveit, 2016].

It is crucial to study the vertical structure of different synoptic storms and predict as accurately as possible.

Since November 2016, the Meteorological Cooperation on Operational Numerical Weather Prediction (MetCoOP) Ensemble Prediction forecast (MEPS) is operational at the Meteorological Institute of Norway (Met-Norway). The ensemble prediction system uses the previous deterministic AROME-MetCoOp, a version of the Météo-France Applications of

Research to Operations at Mesoscale and initialises in addition ten perturbed ensemble members. The use of an ensemble prediction system will give the possibility to analyse the variation of snowfall precipitation in the vertical and at the surface. Microphysical processes in weather models are still not well understood and therefore are mostly parametrised [Müller et al., 2017]. Furthermore, high latitude regions are not well represented in meteorological models. In this study, the newly developed ensemble prediction systems (EPS) from Met-Norway is used to analyse the extreme winter storm during Christmas 2016. It will be shown if the EPS is able to forecast the variation of an extreme winter storms such as 'Urd' and if it is able to predict large scale effects as well as local effects. This work focuses on the measurement site Haukeliseter in Southern Norway. During winter 2016 state of the art ground measurements were installed to estimate the vertical snow water content in the atmosphere. The usage of a snowfall retrieval with ground-based measurements will give an insight to the microphysical structure of the extreme event.

Snowfall is important in the Norwegian mountains for safety and drinking water resources. The aim of this thesis is to evaluate the regional forecast model MEPS by using local observations from a mountain side in Norway. This thesis will examine research questions: How well will the model predict the surface snowfall at the measurement site? Does the regional model cover local affects associated with the topography around the side? Will precipitation transitions from snow to rain to snow forecasted by the regional model?

The thesis is structured as following: Chapter 2 will present the synoptic analysis of the extreme storm, which will later be used to evaluate MEPS. The third chapter will give an overview of the measurement site Haukeliseter and its instrumentation. Chapter 4 and 5 covers the optimal estimation snowfall retrieval and regional model, respectively. After this will Chapter 6 present the results and discussion. The daily MEPS runs will be compared to the observed surface accumulation and the vertical retrieved snow water content. Furthermore, precipitation characteristics such as wind influence and rain segments will be discussed. The final Chapter summarises the results and findings and suggests future research which has to be done.

CHAPTER 2: SITE, INSTRUMENTATION, DATA, AND METHODOLOGY

This chapter describes the site, instruments, the optimal estimation retrieval and the regional forecast model used in the scope of this study, to determine the snow water content in the vertical. The determination of required parameters from the measuring instruments in relation to the optimal estimation retrieval will be explained. The purpose of this study is to compare the vertical observations from the Haukeliseter measurement site and the output from the operational forecast model at the Norwegian Meteorological Institute for the extreme weather event during Christmas 2016. The last section will give an insight on how the data was analysed to compare the different systems.

2.1 HAUKELISETER SITE

Haukeliseter, shown in Figure 2.1.1 is a mountain plateau 991 m above sea level, located in the Norwegian county 'Telemark' (59.8° N, 7.2° E, Figure 2.1.1). The station measures precipitation, temperature, snow depth and wind. It has served as a measurement site for snow accumulation since the winter of 2010/2011 [Wolff et al., 2010, 2013, 2015] and serves as WMO (World Meteorological Organization) station.

The study site is surrounded by mountain tops being 100 m to 500 m higher than the flat area. As seen in Figure 2.1.1c is Haukeliseter more open to the south and the south-west and the closest mountain top (situated to the NE) has an altitude of 1162 masl, [Wolff et al., 2015]. The mountains west to north exceed elevations of 1600 m.

A detailed setting of the measurement site is shown in Figure 2.3.1 with precipitation sensors perpendicular to the predominant wind. Additional measurements of other

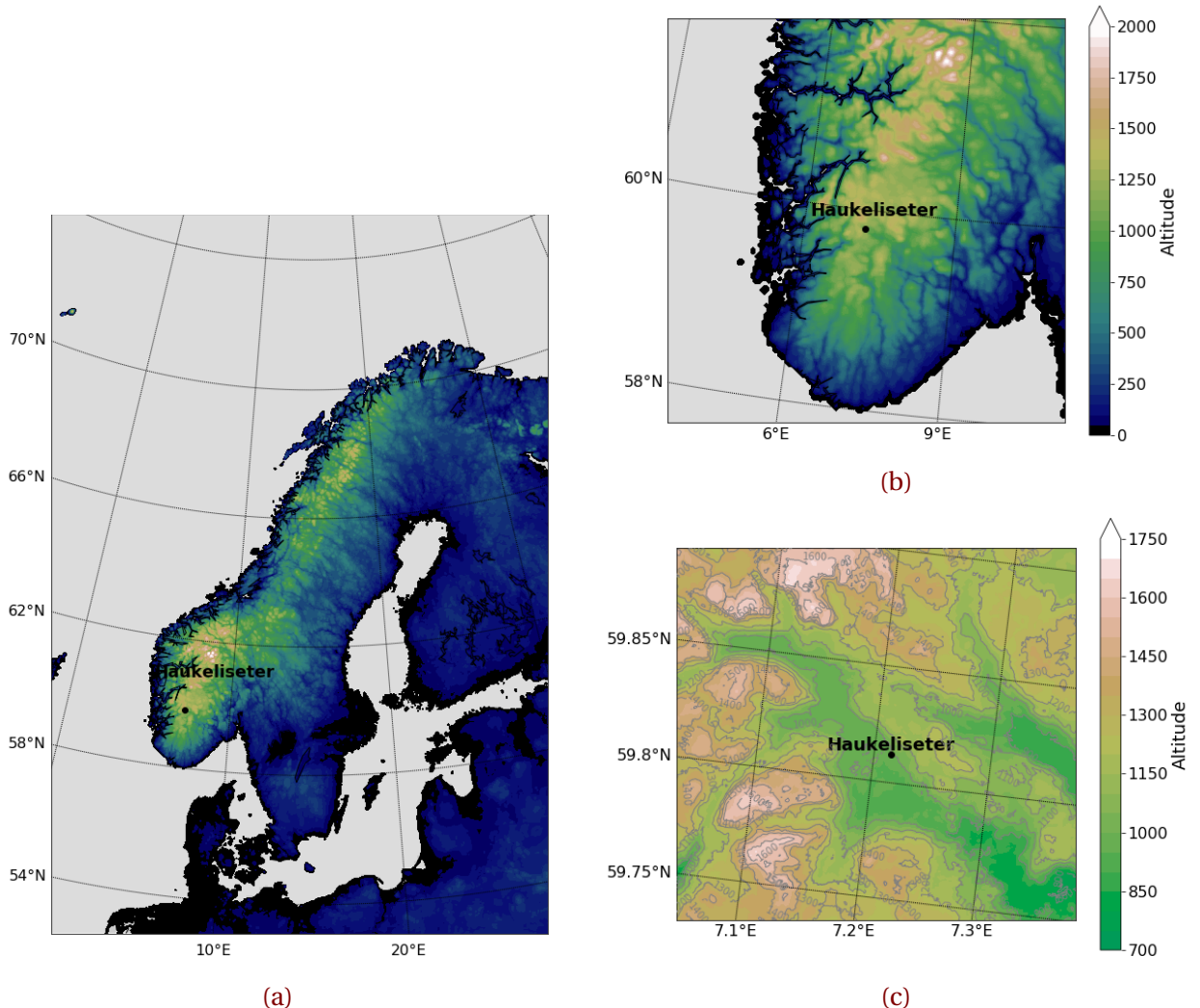


Figure 2.1.1: Model elevation map of Northern Europe (a) and South Norway (b). **a** Shows the model domain of MEPS in Lambert projection. Elevation in **a**, **b** according to the shading in **b**. **c**: Topographical map of the measurement site. Contours and shading presented with DTM 10 Terrain Model (UTM33) from [Geonorge \[2018\]](#).

meteorological parameters such as temperature, wind, and pressure are used to get the large-scale weather situation into a connection with the local measurements. The data is provided by [eklima \[2016\]](#), where the temperature is measured at double fence height. The hourly value of temperature is represented by the last minute value of the previous hour measurement. The 10 m wind is measured by an ultrasonic wind sensor from Gill,

mounted at the tower close to the double fence. The data represents the averaged 10 min wind prior to the full hour.

2.2 CLIMATE AT HAUKELISETER

The general climate at Haukeliseter can be defined with the updated Köppen-Geiger climate types presented in [Peel et al. \[2007\]](#). Figure 8 in [Peel et al. \[2007\]](#) shows, that Haukeliseter may lay in a transition zone and can be categorized as ET, a polar tundra climate type (hottest month temperature $T_{hot} \geq 0^{\circ}\text{C}$) or Dfc, a cold climate without dry season and cold summers. Haukeliseter presents a typical Norwegian climate condition. At the measurement site, frequent snow events combined with high wind speeds are observed during a six to seven-month winter period. In addition, a snow amount of about 2 m to 3 m can be expected, where 50 % of the yearly precipitation is solid in the form of snow, graupel or mixed-phase precipitation [[Wolff et al., 2010, 2013, 2015](#)].

The mean wind direction (Figure 2.3.1) for solid precipitation is from the west/east with maximum wind speeds above 15 ms^{-1} , observed during a 10-year winter period at a nearby station [[Wolff et al., 2010, 2015](#)]. In Figure 2.2.1, the green dashed line, represents the average December temperature of -6°C (30-yr period 1961 to 1990, value taken from [eklima \[2016\]](#)). December 2016 was warmer with an anomaly of +4.9 K above the climate mean. In 2016, the precipitation was 200 % more than the climate mean during December. This difference could be associated with the new installation of the double fence - Geonor gauge at Haukeliseter. In [Wolff et al. \[2015\]](#), Figure 5 shows that single fence precipitation gauges underestimate the amount of precipitation about 80 % during high wind speed events. Since the Double Fence construction was not in use before 2010/2011, this might have led to an observation of too little precipitation at Haukeliseter during winter and followed an incorrect climate statistic. The precipitation observed in the time period 21 December 2016 to 27 December 2016 where 56.9 % of the total accumulation in December 2016. Furthermore, a maximum wind of 22.3 ms^{-1} was observed in this period, which can be associated to a slight storm, which is further described in Section 3.5 and Table 3.5.1.

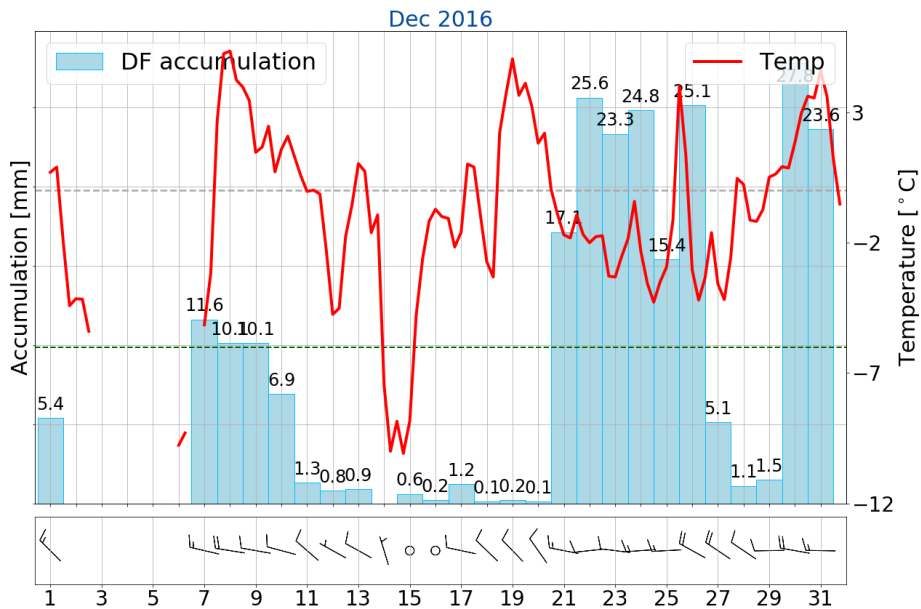


Figure 2.2.1: Observations at Haukeliseter weather mast for December 2016. Daily accumulation [mm] in light blue, mean temperature every six hours (red, [°C]), and daily maximum 10 m wind as barbs [m s^{-1}]. Gray dashed line indicates the freezing temperature. The monthly normal value is green dashed ($-6.0\text{ }^{\circ}\text{C}$), the values are taken from [eklima \[2016\]](#). Note, that no data was available from 2 December 2016 to 6 December 2016.

2.3 INSTRUMENTS

Many factors such as humidity and temperature contribute to snowflake geometry. The knowledge of snowflake habits, particle size distributions, and fall speed lead to a reduction of errors in optimal estimation retrievals.

This work is based on several datasets collected at the Haukeliseter measurement site, 59.8°N , 7.2°E . A composition of advanced ground-based observations and the CloudSat precipitation retrieval will help to get a better understanding of the vertical structure of the atmosphere.

A collaboration between the University of Utah, University of Wisconsin and Met-Norway made it possible to install three additional instruments at the measurement site during winter 2016/2017. A Multi-Angle Snowflake Camera (MASC) and a Precipitation Imaging Package (PiP) will be used to determine the snow habit, the snowfall particle size distribu-

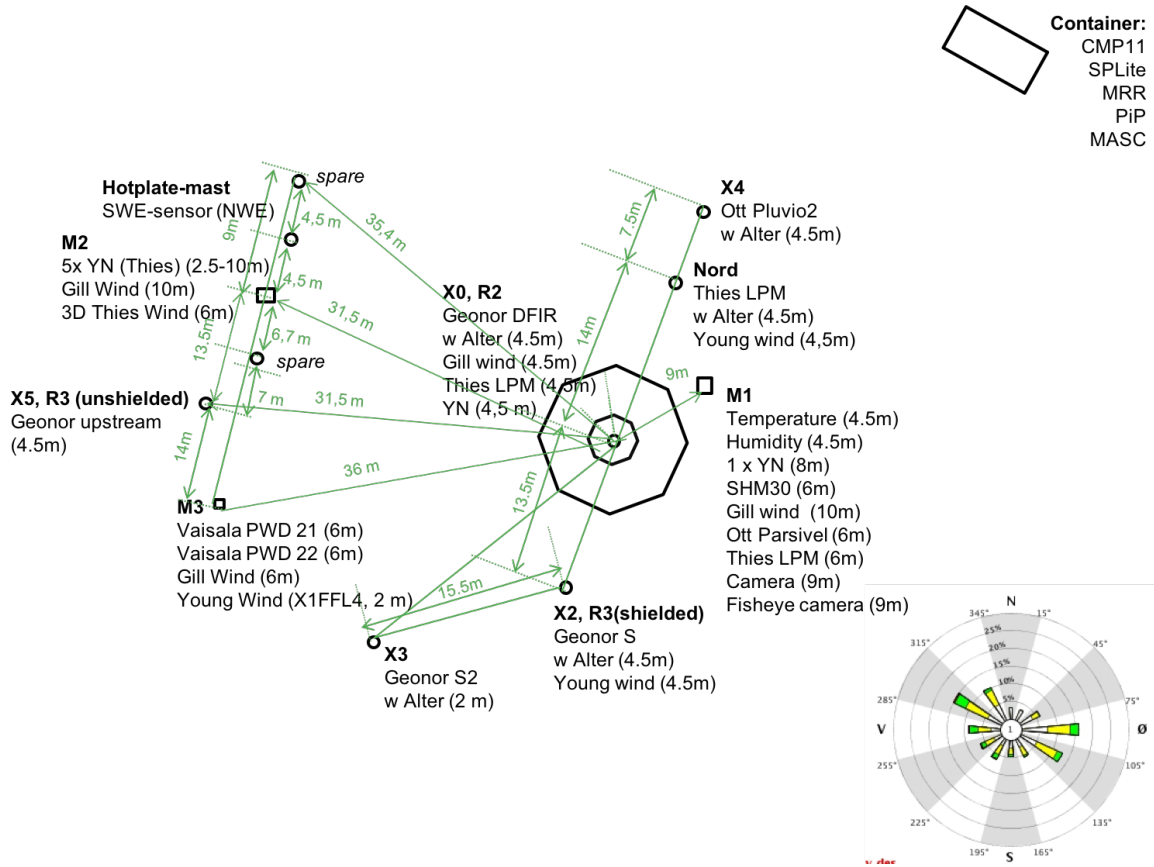


Figure 2.3.1: Instruments at the Haukeliseter measurement site during winter 2016/2017 [adapted from Wolff et al., 2015]. The windrose indicates the mean wind direction from either from west-north-west or east-south-east.

tion, and near-surface fall speed. Additionally, a Micro Rain Radar (MRR) is established to obtain fall speed and particle reflectivity aloft. Together with temperature observations at the surface, is this a good basis to reduce the non-uniqueness of snow accumulation in optimal estimation snowfall retrieval, described in Section 2.4.

A sketch of the instrumentation setting is presented in Figure 2.3.1. The octagonal indicates the double fence. The container is north-east from the double fence having the MRR, MASC and PiP mounted at the top. **M1** in Figure 2.3.1 is the 10 m weather mast, providing the hourly eklima [2016] temperature, pressure, and wind measurements. The mean wind direction from west-north-west and east-south-east are shown in the wind rose in Figure 2.3.1.

2.3.1 DOUBLE FENCE

Since the winter season 2010/2011 Haukeliseter is equipped with several precipitation gauges. The wind shielded gauges are placed perpendicular to the main wind direction (E/W wind).

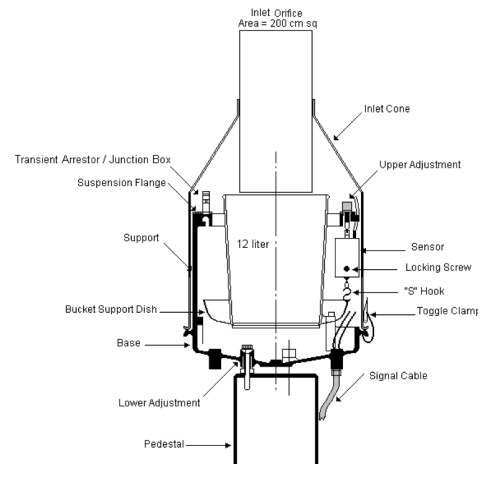
In a study by Wolff et al. [2015] the wind-induced under-catch of solid precipitation is determined. Dependent on the kind of precipitation the wind plays different roles in the amount of accumulation. For temperatures below -2°C the wind speed influences the falling snow. Where less precipitation can be observed at higher wind speeds or more precipitation can be measured if too much is blown into the gauge. The catch ratio between the standard Geonor precipitation gauge and the Double Fence - Geonor (Figure 2.3.2a) shows, that only 80 % of solid precipitation are observed at wind speeds of 2 m s^{-1} and only 40 % at 5 m s^{-1} , Wolff et al. [Figure 5 in 2015].

The precipitation gauge protected by an octagonal double fence (Figure 2.3.2a) is more accurate than the single fence and will be used as the reference to all surface accumulation measurements. The double fence creates an artificial calm wind and maximize the catch of precipitation, [Wolff et al., 2010, 2013, 2015]. The wind inside the double fence is measured to be not much higher than 5 m s^{-1} even if the winds outside exceed 20 m s^{-1} (occurred 26 December 2016).

This shows the need of a combination of ground-based observations together with an optimal estimation retrieval to verify the accuracy of MEPS. Wolff et al. [2015] introduced



(a)



(b)

Figure 2.3.2: a: Double fence and unprotected precipitation gauges at Haukeliseter, from Wolff et al. [2015]. The prevailing wind direction from east comes from the lower, left corner in the image and the west wind from the opposite site. b: Vertical cross section of T-200B precipitation gauge [Geonor Inc., 2015].

an adjustment function for the Geonor double fence, so that different precipitation under certain wind speeds are presented correctly and can be used as confidential data. For now, it is presumed that the average under catch inside a double fence is 20 % for wind speeds between 10 m s^{-1} and 20 m s^{-1} and 10 % for wind speeds under 9 m s^{-1} [Wolff, 2018].

Inside the double fence is a precipitation-weighing gauge Geonor T-200B3 [3-wire transducers, 1000 mm, [Geonor Inc., 2015](#)] with an Alter wind screen to reduce wind turbulence around the gauge. At Haukeliseter is the orifice height of the Geonor 4.5 m above the ground. This is due to an expected snow depth of 2 m to 3 m during a winter season and to reduce the likelihood of measuring drifting snow [[Wolff et al., 2013, 2015](#)].

A vertical cross section of the T-200B gauge is shown in Figure 2.3.2b. Precipitation particles fall through the 200 cm^2 orifice protected with a heated collar, into a cylindric bucket filled with frost protection. The bucket is placed on top of a Bucket Support Dish [Figure 2.3.2b, [Geonor Inc., 2015](#)]. This dish is connected with three wire sensors having an eigenfrequency changing with the weight inside the bucket. A formula provided by [Geonor Inc. \[2015\]](#) calculates the amount of precipitation from the frequency of each sensor. The three sensors provide a reduction of an error in connection with an unlevel installation. Met-Norway will average value of all three sensors and provide it as hourly data at [eklima](#).

2.3.2 MRR - MICRO RAIN RADAR

Radar are very useful to observe the vertical of the atmosphere. The instrument is able to detect mesoscale features and makes it possible to see the vertical structure of storms [[Markowski and Richardson, 2011](#)].

The principle of radar measurements is based on an electromagnetic wave, which is emitted from the radar transmitter and interacts with the hydrometeors along the beam. A fraction of the pulse energy is reflected back to the receiver of the radar. The quantity of scattering depends on the shape and structure of the reflected particle. Vertical profiles of reflectivity give information about the diameter of the target object.



Figure 2.3.3: Micro Rain Radar.

The Micro Rain Radar, in Figure 2.3.3, measures profiles of Doppler spectra [METEK, 2010]. The Doppler spectrum tells about the movement of the particle. The vertical pointing Doppler radar measures the energy that is returned from each interval and thus enabling the detection of the Doppler spectrum [L'Ecuyer, 2017]. The MRR measures at a frequency of 24 GHz and has a temporal and spatial resolution of 60 s and 100 m, respectively. The radar height range is from 100 m (because of ground clutter) to 3.000 m [METEK, 2010]. MRR radar reflectivity (Z) is transformed from $1 \text{ mm}^6/\text{m}^3$ to dBZ. The transformations are done with the following relationship;

$$Ze = 10 \log_{10} \left(\frac{Z}{1 \text{ mm}^6/\text{m}^3} \right) \quad [\text{dBZ}] \quad (2.3.1)$$

A transformation to rainfall rates can be performed by the $Z-R$ (reflectivity - rainfall) relationship. The rainfall rate in each layer can be estimated by the use of typical fall speeds and the Marshall-Palmer particle size distribution for liquid particles [Rinehart, 2010].

$$\begin{aligned} Z &= 200R^{\frac{8}{5}} \quad [\text{mm}^6\text{m}^{-3}] \\ R &= \left(\frac{10^{\frac{Ze}{10}}}{200} \right)^{\frac{5}{8}} \quad [\text{mmh}^{-1}] \end{aligned} \quad (2.3.2)$$

Table 2.3.1 represents the Z-R relationship if the Marshall-Palmer assumption (Equation (2.3.2)) is applied. Z-snowfall relationships are developed but are difficult to apply due to the variation of size and density of the particles [L'Ecuyer, 2017].

After the transformation to dBZ the reflectivity is averaged for every 200 m layer thickness, where only values above 300 m are taken. For instance, a reflectivity at 400 m represents the mean value of reflectivity between 300 m and 500 m.

Table 2.3.1: Typical reflectivity values, from [Doviak and Zrnic \[1993\]](#). The values are obtained from measurements, models and observations. The rainfall rate R is calculated with Equation (2.3.2).

	Ze [dBZ]	R [mm h ⁻¹]
Drizzle	<25	1.3
Rain	25 to 60	1.3 to 205.0
Snow		
dry, low density	<35	5.6
Crystal; dry, high density	<25	1.3
wet, melting	<45	23.7
Graupel		
dry	40 to 50	11.5 to 48.6
wet	40 to 55	11.5 to 99.9
Hail		
small; <2 cm, wet	50 to 60	48.6 to 205.0
large; >2 cm, wet	55 to 70	99.9 to 864.7
Rain & Hail	50 to 70	48.6 to 864.7

2.3.3 PiP - PRECIPITATION IMAGING PACKAGE

The precipitation imaging package (PiP) is a modification of the Snowflake Video Imager presented by [Newman et al. \[2009\]](#). The video distrometer is a construct of a halogen flood lamp and a video system (Figure 2.3.4). The instrument determines the habit of snowflakes from images at a frequency of 60 Hz. Lamp and lens have a distance of approximately 3 m which follows a field of view: 32 mm by 24 mm.

In front of the halogen lamp is a frosted window, so that the background light is uniform over all time. A falling particle appears as a 2-D shadow in the video image. Particle size distribution (PSD) and fall speed of precipitation can be determined from the black and white images of the system. [Newman et al. \[2009\]](#) describes in detail the algorithm applied to the system to get information about the snow-particle habit.

Winds have almost no effect on the result of the video distrometer [[Newman et al., 2009](#)]. To reduce eventual wind effects, was the distrometer oriented perpendicular to the mean wind.



Figure 2.3.4: Precipitation Imaging Package.

2.3.4 MASC - MULTI-ANGULAR SNOWFALL CAMERA

Instruments like the afore mentioned PiP has according to [Garrett et al. \[2012\]](#) coarser resolution and the determination of particle size can have larger errors. Hence, a new instrument was developed. The Multi-Angular Snowfall Camera (MASC) takes high-resolution images of hydrometeors in free fall and measures the fall-speed simultaneously.

The MASC consists of three cameras, three flashes, and two near-infrared sensors, pointing at a ring centre (Figure 2.3.5). A hydrometeor has to pass through the ring in a certain way to trigger the near-infrared sensors. At the same time the three cameras take a picture of the falling particle. Since the cameras take pictures from three different angles, the particles size, shape, and orientation can be specified from an algorithm applied to the image, described in [Garrett et al. \[2012\]](#). Furthermore, the form and heritage of the hydrometeor, such as collision-coalescence, riming, capture nucleation, or aggregation, can be determined. The near-infrared sensor, that is used to trigger the cameras and the lights quantifies the fall-speed of the hydrometeors, by measuring the time the particle needs to pass the distance between the upper and lower trigger.

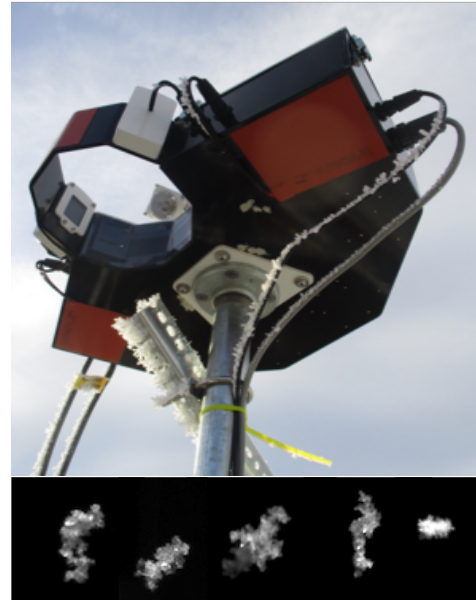


Figure 2.3.5: MASC and images taken by instrument during the Christmas storm 2016.

2.4 OPTIMAL ESTIMATION RETRIEVAL ALGORITHM

Since 2006, with the launch of CloudSats Cloud Profiling Radar (CPR) a global estimation of snowfall can be done. Several studies, such as [Kulie and Bennartz \[2009\]](#) have shown that estimated snowfall values depend heavily upon assumed snowflake microphysical properties. [Wood et al. \[2015\]](#) showed that a refinement of the CloudSat snowfall retrieval algorithm can be performed by using snowflake models. This study was based on data from the Canadian CloudSat-CALIPSO Validation Project [C3VP, [Hudak et al., 2006](#)], where

they concentrated on cold season clouds and precipitation.

In an attempt to reduce the non-uniqueness of the problem, Wood et al. [2015] used the a priori knowledge of snowfall microphysics and temperature (from ground-based observations) to refine the forward-model assumptions for the CloudSat snowfall retrieval scheme. Results from this scheme showed a good agreement with reported values observed at meteorological measurement sites.

Model estimates have proven, how useful the estimation retrieval can be to verify ground-based radar snowfall measurements [Norin et al., 2015]. Although the retrieval has obviously been improved the estimation algorithm, a priori guess can still lead to uncertainties in the retrievals of up to 140 % to 200 % [Wood, 2011].

Cooper et al. [2017] developed a technique to combine MRR, MASC, and PiP information into a common retrieval framework. Specifically, estimates of snowflake microphysical properties from the MRR are used as the a priori term in the optimal-estimation retrieval scheme. The usage of either MASC/PiP or MRR fall-speed can show which a priori guess in the retrieval gives the more accurate retrieved snowfall rate at the ground.

The difference between the retrieval and the snow gauge observations was –18 % when applied to data from Barrow, Alaska.

Cooper et al. [2017] also showed that the retrieval is sensitive to habit and fall speed. The installation of a MRR, MASC, and PIP should help to adjust the particle models for graupels and rimed particles which are often observed at Haukeliseter.

2.4.1 FORWARD MODEL

Forward model defines a relationship between the radar observations and the retrieved state vector \mathbf{x} . It is difficult to find the properties of the atmosphere by using observations due to unknown parameters influencing the measurement.

Stephens [1994] described the forward problem in the manner that e.g. a reindeer represents the known source, observations Figure 2.4.1. The amount of received radiation lost during the transmittance to the sensor is unknown, the Tracks in Figure 2.4.1a. The forward model will help to find simulated observations before the attenuation took place and give information about the tracks of the reindeer. In the scope of this work the inverse problem is solved. The tracks in Figure 2.4.1b present the vertical reflectivity observations from the MRR. Using the forward model will solve the inverse problem by finding the question mark in Figure 2.4.1b, which are simulated profiles of SWC.

The knowledge about the a priori parameters and related covariances, as well as \mathbf{x} , are used to minimize the cost function in Equation (2.4.7). The values of \mathbf{x} are found by Newtonian iteration Wood et al. [2014, Eq. 5].

The snow water content in each layer is estimated from the knowledge of the snow particle mass-dimension relationship in Appendix B.1, and a PSD related to slope parameter and number concentration (Equations (2.4.12–14)).

$$\text{SWC} = \int_{r_{min}}^{r_{max}} m(r)n(r)dr \quad [\text{gm}^{-3}] \quad (2.4.1)$$

To achieve a relationship between the reflectivity and the snowfall amount one needs to account for attenuation in the atmosphere. Using the previously calculated PSD (Equation (2.4.12)) the backscattering cross-section σ_{bk} , one can estimate the reflectivity for

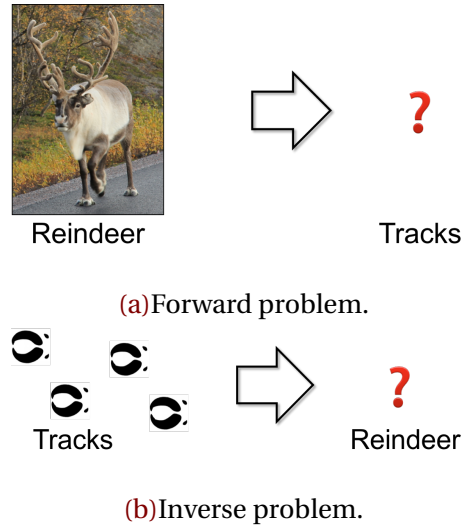


Figure 2.4.1: a: Relationship between parameter of interest (reindeer) and the unknown parameter of measurements (tracks). b: Inverse problem when the parameter of measurements is known but the parameter of interest is not [Stephens, 1994].

Rayleigh approximated, singly-scattered non-attenuated ice particles [Kulie and Bentartz, 2009, L'Ecuyer and Stephens, 2002, Wood et al., 2015]. The Rayleigh approximation assumes, that $2\pi r/\lambda \ll 1$, where λ the wavelength of incident radiation.

$$\begin{aligned}\eta_{bk} &= \int_{r_{min}}^{r_{max}} n(r) \sigma_{bk} dr \quad [\text{m}^{-1}] \\ Ze^{ss,na} &= \frac{\Lambda^4}{\|K_w\|^2 \pi^5} \eta_{bk} \quad [\text{mm}^6 \text{m}^{-3}]\end{aligned}\quad (2.4.2)$$

where, Λ is the wavelength of the radar; $\|K_w\|^2$ is the complex refractive index of water and varies between 0.91 and 0.93 for wavelength between 0.01 m and 0.10 m and is independent of temperature. It also exists a complex refractive index for ice $\|K_i\|^2$, which is 0.18. This is valid for a density of 0.917 g cm^{-3} and is independent of temperature and of wavelength in the microwave region [Doviak and Zrnic, 1993]. In this work $\|K_w\|^2 = 0.93$ is chosen, BECAUSE???

The singly-scattered reflectivity has to be corrected for attenuation in the layers above the actual layer. According to Beer's law is in a homogeneous medium one-way transmission assumed.

$$\frac{I_\lambda}{I_{\lambda_0}} = \exp \left[- \int_0^s \beta_{ext} ds' \right] \quad (2.4.3)$$

where s is the path length through the medium. The transmissivity I_λ/I_{λ_0} is the relation of survived radiation through extinction in the atmosphere with the snow extinction coefficient β_{ext}

$$\beta_{ext} = \int_{r_{min}}^{r_{max}} n(r) \sigma_{ext} dr \quad [\text{m}^{-1}] \quad (2.4.4)$$

The extinction coefficient is the sum of absorption and scattering in the atmosphere followed from the extinction cross-section $\sigma_{ext} = \sigma_{abs} + \sigma_{scat}$, [Lamb and Verlinde, 2011, Lohmann et al., 2016]. Lohmann et al. [Eq. 12.1 and more 2016]

Following Equations (2.4.2–4) the singly-scattered attenuated reflectivity $Ze^{ss,a}$ is

$$Ze^{ss,a} = Ze^{ss,na} \cdot \frac{I_\lambda}{I_{\lambda_0}} \quad [\text{mm}^6 \text{m}^{-3}] \quad (2.4.5)$$

That follows with the use of radiative transfer equations for the simulated reflectivity from the forward model, $F(\mathbf{x})$ in Equation (2.4.7), after the transformation with Equation (2.3.1)

$$F(\mathbf{x}) = \begin{bmatrix} Ze_1^{ss,a} \\ \vdots \\ Ze_{nlayer}^{ss,a} \end{bmatrix} \quad [\text{dBZ}]. \quad (2.4.6)$$

2.4.2 SNOWFALL RETRIEVAL SCHEME

The optimal estimation method is based on Gaussian statistics. Minimizing the scalar cost function, Φ for the snowfall properties, \mathbf{x} . The cost function weights the difference between the observed reflectivity and the simulated measurements as well as the difference between the estimated and a priori guess.

Scalar cost function:

$$\begin{aligned} \Phi(\mathbf{x}, y, a) = & (y - F(\mathbf{x}))^T \mathbf{S}_y^{-1} (y - F(\mathbf{x})) \\ & + (\mathbf{x} - a)^T \mathbf{S}_a^{-1} (\mathbf{x} - a) \end{aligned} \quad (2.4.7)$$

where, \mathbf{x} , vector of retrieved snowfall properties (Equation (2.4.15)); y , vector of observation (MRR reflectivity); a , vector of the a priori guess (temperature dependent); \mathbf{S}_a , a priori error covariance matrix; \mathbf{S}_y , measurement error covariance matrix. The forward model $F(\mathbf{x})$, presented in Section 2.4.1 relates unknown snowfall parameters \mathbf{x} to radar observations y and approximates the true physical state between them [Cooper et al., 2017, Wood et al., 2014].

\mathbf{S}_a links the uncertainties of the PSD information and the surface temperature differences. The diagonal matrix elements in \mathbf{S}_a are equal to 0.133 and 0.95 for the particle slope parameter and the number concentration, respectively as from Eq. 7.35 and 7.36 in Wood [2011].

\mathbf{S}_y characterises the uncertainties associated with the measurements and the error in the forward model. This study uses for the diagonal matrix elements 2.5^2 UNIT! based on the study from CITATION. BECAUSE.

I don't understand the next steps and if it is still the same \mathbf{x} ?

At convergence is the error covariance of the retrieved state vector \mathbf{S}_x

$$\mathbf{S}_x = \left(\mathbf{S}_a^{-1} + \mathbf{K}^T \mathbf{S}_y^{-1} \mathbf{K} \right)^{-1} \quad (2.4.8)$$

which follows for \mathbf{x}

$$\mathbf{x} = \underbrace{\left(\mathbf{S}_a^{-1} + \mathbf{K}^T \mathbf{S}_y^{-1} \mathbf{K} \right)^{-1}}_{\mathbf{S}_x} \left(\mathbf{S}_a^{-1} \mathbf{a} + \mathbf{K}^T \mathbf{S}_y^{-1} (y - F(\mathbf{x}) + \mathbf{K}\mathbf{x}) \right) \quad (2.4.9)$$

The Jacobian matrix, \mathbf{K} , represents the sensitivity matrix of the perturbed result of the forward model. The true state \mathbf{x} is perturbed by $\pm 0.2\%$ and thus \mathbf{K} represents the relation between simulated values to the true state and how sensitive the simulated values are to small changes when starting a new retrieval cycle. The closer \mathbf{K} is diagonal, the more is \mathbf{x} determined by the real observed and a priori values. If the limit of the partial derivative is close to unity, the retrieved value \mathbf{x} is its true state [Wood, 2011].

mmmh? What exactly are we doing here? Test the if convergent:

$$\hat{x} = (\mathbf{x} - F(\mathbf{x}))^T \mathbf{S}_x^{-1} (\mathbf{x} - F(\mathbf{x})) \quad (2.4.10)$$

only if \hat{x} is smaller than 2 it is a 'good' retrieval.

To test the result of \mathbf{x} a χ^2 test is performed at the convergence of \mathbf{S}_x .

$$\begin{aligned} \chi^2 = & (F(\mathbf{x}) - y)^T \mathbf{S}_y^{-1} (F(\mathbf{x}) - y) \\ & + (\mathbf{x} - \mathbf{a})^T \mathbf{S}_a^{-1} (\mathbf{x} - \mathbf{a}). \end{aligned} \quad (2.4.11)$$

The first term in Equation (2.4.11) measures the part of χ^2 related to the noise of the forward model, and the second part the relation to the state vector. Thus, the second term describes the accuracy of the quantities within the reflectivity and temperature measurements [Rodgers, 2000]. Furthermore, are the error contribution from the reflectivity measurement uncertainty, \mathbf{S}_{y_e} , and the uncertainty of the a priori values, \mathbf{S}_{a_e} estimated.

2.4.3 PRESENCE OF SNOW

To achieve vertical profiles of snowfall from MRR different steps and assumptions are done in the here presented snowfall retrieval. From one of the lower levels, the snowfall rate at the surface can be estimated. The retrieval is only performed for profiles, which are likely to have observed snow, where most retrievals use rain. In previous studies relationships between reflectivity and snowfall have been developed. Even if the PSD of ice particles is known, different crystal shapes led to different results. Snow densities vary significantly

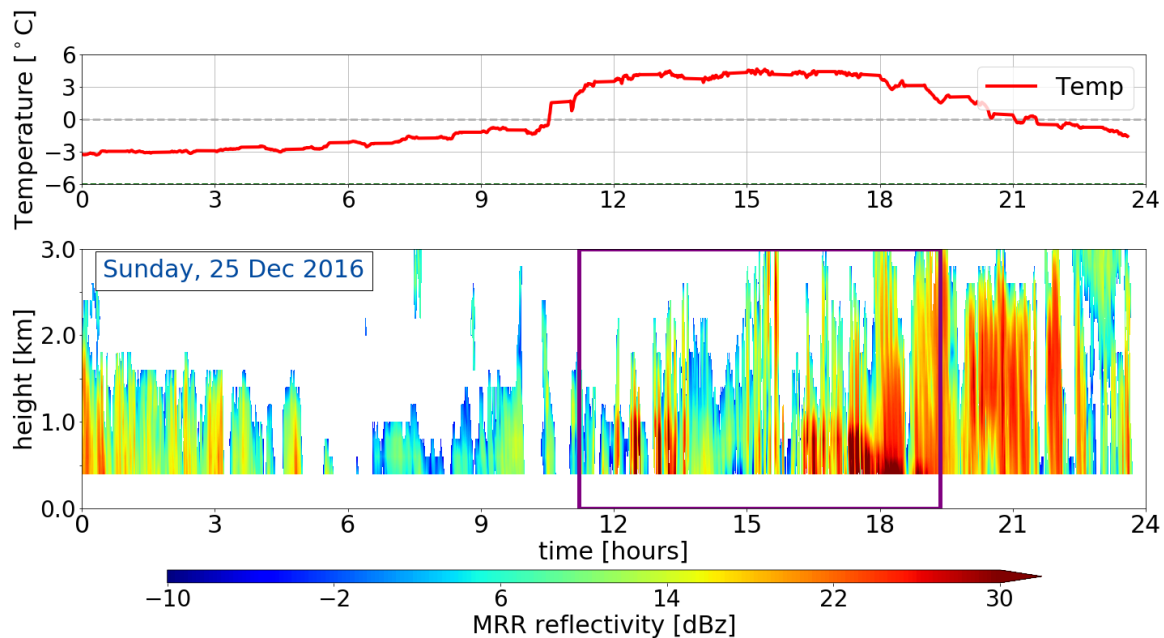


Figure 2.4.2: Shows the a priori temperature dependence within the optimal estimation retrieval for an all day precipitation event on 25 December 2016. The upper panel shows T_{ap} measured at the Haukeliseter site. The lower panel presents the reflectivity from the MRR in addition indicates the purple frame the time, where the MRR reflectivity was larger than -10 dBZ and surface temperatures less than 2°C

from storm to storm, where small particles are still Rayleigh scattered, and larger particles non-Rayleigh scattered [Gunn and East, 1954].

To obtain the likelihood of present snow a reflectivity threshold of -15 dBZ is used. This threshold is similar to the one used in Wood et al. [2013], where it states that light liquid precipitation is related to -10 dBZ [Stephens and Wood, 2007]. Wood [2011] compared the reflectivity in the lowest bin and adjacent bin and found, that the reflectivity above -15 dBZ are not influenced by ground clutter.

The Haukeliseter measurement site is equipped with a weather mast, measuring the air temperature every minute at two meter height (compare Figure 2.4.2, upper panel). Since the MRR measures above 300 m and only temperature measurements at the surface exists, a priori temperature (T_a) is assumed to be similar to the observed near-surface air temperature. Using a moist adiabatic lapse rate of $dT/dz = 5 \text{ K km}^{-1}$ gives T_a in each layer. Assuming snow exists at temperature measurements up to a threshold of 2°C , validated by

Liu G. [2008] who analysed present weather reports to find the distinction between liquid and solid precipitation.

The purple line in the lower panel of Figure 2.4.2 represents the time frame during 25 December 2016, where the MRR reflectivity is less than -15 dBZ, and a priori temperature passes the 2 °C limit at the surface.

2.4.4 SIZE DISTRIBUTION

To determine the snowfall rate at the surface an exponential particle size distribution (PSD) is needed.

$$n(r) = N_0 \exp(-\lambda r) \quad [\text{m}^{-3} \text{ mm}^{-1}] \quad (2.4.12)$$

where λ represents the PSD slope parameter and N_0 the number concentration. r is the particle maximum dimension evaluated from the 2D-scattering model for branched 6-arm spatial particles with porosities for reflectivity measurements at 24 GHz (see Appendix B.1). Since T_a varies with a moist adiabatic lapse rate in each layer bin the slope parameter and the number concentration in Equation (2.4.12) are changing too. Wood [2011] showed a linear fit between $\log(\lambda)$ and the a priori temperature, respectively $\log(N_0)$ and the a priori temperature. Using T_a in °C for each layer bin the following logarithmic assumption is used, to define the slope parameter and the number concentration.

$$\log(\lambda) = -0.03053 \cdot T_{ap} - 0.08258 \quad [\log(\text{mm}^{-1})] \quad (2.4.13)$$

$$\log(N_0) = -0.07193 \cdot T_{ap} + 2.665 \quad [\log(\text{m}^{-3} \text{ mm}^{-1})] \quad (2.4.14)$$

To achieve the state vector \mathbf{x} of unknown microphysical properties, the log-transformed values are taken.

$$\mathbf{x} = \begin{bmatrix} \log(\lambda)_0 \\ \vdots \\ \log(\lambda)_{\text{nlayer}} \\ \log(N_0)_0 \\ \vdots \\ \log(N_0)_{\text{nlayer}} \end{bmatrix} \quad \text{nlayer} = 14 \quad (2.4.15)$$

The log-transformed equation is useful, since the results from C3VP were similar to other observations. The study showed, that N_0 ranges over several order of magnitude as well as λ was non-Gaussian for the snow events [Wood \[2011\]](#).

2.4.5 SNOWFALL RATE AT THE SURFACE

To achieve snowfall rates at the surface, the snow water content (Equation (2.4.1)) has to be transformed. The use of an assumed particle fall speed of $V = 0.85 \text{ ms}^{-1}$ and the retrieved SWC (Equation (2.4.1)) gives the snow mass flux $J_{\text{snow}} = \text{SWC} \cdot V$ in $[\text{kg m}^{-2} \text{ s}^{-1}]$. [Why did we use this fall speed? Where does this assumption come from? Similar as Cooper et al. \[2017\] Eq. 4?](#) To compare retrieved snow, fall rates to double fence measurements and the forecast model output, the precipitation amount at the surface is calculated.

$$P = J_{\text{snow}} \times 10^{-3} \cdot (3600 \text{ s} \cdot 24) \quad [\text{mm d}^{-1}] \quad (2.4.16)$$

The precipitation amount at the surface, presented in Chapter 4, are taken to be equal to the values at the snow layer in 400 m, the lowest level of the obtained averaged MRR reflectivity.

2.5 METCOOP ENSEMBLE PREDICTION SYSTEM

MEPS (MetCoOp Ensemble Prediction System) was newly operational at Met-Norway when the extreme weather occurred in Norway. Comparing model data with actual observations helps to verify the agreement between model prediction and ground-based measurements.

AROME-MetCoOp was operational from March 2014 until November 2016, when it was replaced with an ensemble prediction system (EPS) based on AROME-MetCoOp. MEPS is used as weather forecast at the Norwegian Meteorological Institute, the Swedish Meteorological and Hydrological Institute (SMHI) and the Finnish Meteorological Institute (FMI), [\[Køltzow, 2017, Müller et al., 2017\]](#).

2.5.1 AROME - METCOOP

In principle, MEPS is a short-term weather forecast consisting of a ten ensemble member forecast system with 66 h prediction time and a horizontal resolution of 2.5 km and 65 ver-

tical levels. One of the members is the deterministic forecast where the other nine present the perturbed state of the deterministic forecast. The initialisation of each member is performed at 0 UTC, 6 UTC, 12 UTC and 18 UTC [MetCoOp Wiki, 2017].

Forecast data saved for the deterministic and first ensemble member have a time resolution of one hour for 66 h. The other eight members have values every three hours for up to 48 h forecast time.

Figure 2.1.1a shows the MEPS model domain and its elevation as it was operational for December 2016. It covers the Nordic Countries including open water such as the Atlantic Ocean, the North and the Baltic Sea. A representation of the horizontal resolution zoomed on the Haukeliseter site is shown in Figure 2.5.1. Haukeliseter is surrounded by a complex terrain with mountains up to 1500 m no the west and the north and the more open terrain to the south-east.

The centre of the model is approximately at 63.5° N, 15° E. The horizontal grid points are projected on a Lambert projection to receive the same area size of each grid cell. The outer, parent grid is the ECMWF-IFS model (European Centre for Medium-Range Weather Forecasts Integrated Forecasting System) with a horizontal resolution of 9 km [Homleid and Tveten, 2016]. The ECMWF-IFS forecasts are used 6 h prior to the actual cycle in MEPS.

Vertical hybrid coordinates are terrain-following and are mass-based, [Müller et al., 2017]. How the vertical hybrid coordinates are transformed into layer thickness or height is described in Section 2.6.1. Furthermore, MEPS underlies non-hydrostatic dynamics, MetCoOp Wiki [2017].

The representation of snow is covered by a modification of the three-class ice parametrization (ICE3) scheme. Where liquid-phase processes are separated from slow ice-phase processes and described in Section 2.5.2. To model the snow cover an one-layer atmo-

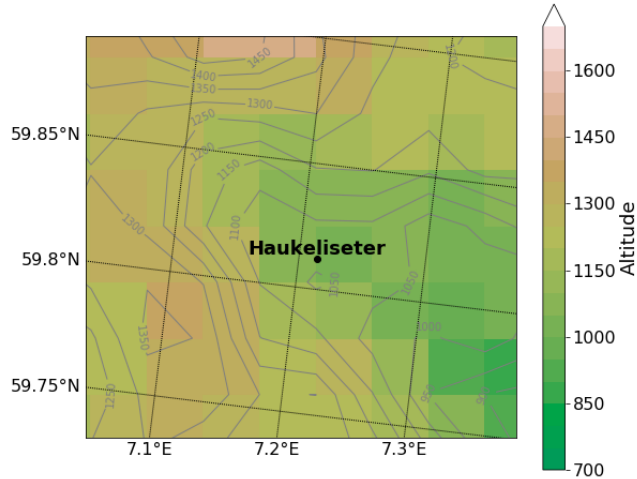


Figure 2.5.1: Representation of the topography around measurement site Haukeliseter in MEPS. Contours and shading present the elevation of the grid cells.

sphere model scheme is implemented. This includes three variables such as: snow water equivalent (SWE), snow density, and snow albedo [Müller et al., 2017].

As synoptic observations are included in the model the snow-depth predictions underlay a special performance. Observations of snow-depth are only available at 6 UTC and 18 UTC, therefore is the snow analysis only performed twice daily [Homleid and Tveter, 2016, Müller et al., 2017].

2.5.2 MESO-NH AND THE ICE3 SCHEME

The physical parametrization within AROME is based on the French research communities' mesoscale non-hydrostatic atmosphere model (Meso-NH). The microphysical scheme in the Meso-NH atmospheric simulation system is based on the ICE3 scheme. The purpose of the scheme is to model as correctly as possible the ice phase in the atmosphere [Pinty and Jabouille, 1998]. McCumber et al. [1991] concluded from their case study, that at least three different ice categories are necessary to cover most precipitation but that applications might be case specific. According to the Meteo France [2009] documentation, the ice phase microphysical scheme must include:

\mathbf{r}_i : pristine ice phase

\mathbf{r}_s : snowflake type from lightly rimed large ice crystals or dry clusters, and

\mathbf{r}_g : heavily rimed crystals, such as graupel, frozen drops or hail

Within the ICE3 scheme no distinction between hail and graupel exists and therefore is the physical discrimination in the growth mode of graupel and hail is neglected.

To achieve snow water content within MEPS the total number concentration, slope parameter, mass diameter and the particle size distribution have to be determined. According to Caniaux et al. [1994] follows the particle size distribution the Marshall-Palmer distribution similar to Equation (2.4.12). The goal is to use a varying number concentration N_0 dependent on the ice category. The study has shown that N_0 can be assumed with

$$N_0 = C \lambda^x \quad (2.5.1)$$

$$\log_{10} C = -3.55x + 3.89$$

where C and x depend on the ice category and represent the relation between each other in Equation (2.5.1).

The ice water content for primary ice, snowflakes and rimed crystals is then assumed to be similar to Equation (2.4.1), but the integration limits range from zero to infinity and mass, and particle size distribution are dependent on the diameter of the particle. The mass diameter and particle size distribution (Equations (2.5.2) and (2.5.3)) are represented depending on the ice category shown in Table 2.5.1

$$m(D) = aD^b \quad (2.5.2)$$

$$n(D) = N_0 g(D) \quad (2.5.3)$$

and $g(D)$ to be the generalised Gamma function

$$g(D) = \frac{\alpha}{\Gamma(\nu)} \lambda^{\alpha\nu} D^{\alpha\nu-1} \exp(-(\lambda D)^\alpha) \quad (2.5.4)$$

with α , ν the shape and tail dispersion parameters and $\Gamma(\nu)$ the gamma function.

After following the above equations including Equation (2.4.1) the slope parameter λ can be generated with $G(B)$ the gamma function.

$$\lambda = \left(\frac{\text{SWC}}{aCG(b)} \right)^{\frac{1}{x-b}} \quad (2.5.5)$$

Meteo France [2009] documentation suggests starting the microphysics in the ICE3 scheme with 'slow' processes such as homogeneous and heterogeneous nucleation (HON, HEN), vapour deposition of snow and graupel particles (DEP), aggregation (AGG) and auto conversion (AUT), for ice processes right side in Figure 2.5.2. The second step is to initiate the warm processes left side in Figure 2.5.2. Then include the aggregation and conversion-melting (CVM) for snowflakes and contact freezing of raindrops (CFR). Add AGG and melting for graupel (MLT), and then the melting from pristine ice and the Wegener-Bergeron-Findeisen (BER) effect and lastly the sedimentation terms.

Figure 2.5.2 shows the summary of the microphysical processes for mixed phase clouds. The study focuses mostly on solid precipitation particles and therefore only the initiation and growth of pristine ice crystals r_i , snowflakes r_s , and rimed crystals r_g is presented.

Following Pinty and Jabouille [1998] and Figure 2.5.2 it can be seen how AROME performs the ice production. Orange lines in Figure 2.5.2 show the initiation of pristine ice

Table 2.5.1: Characterization parameters from primary ice (r_i), snowflakes (r_s) and rimed crystals (r_g). Values are based on the references in [Meteo France \[2009\]](#) and in [Pinty and Jabouille \[1998\]](#).

	r_i	r_s	r_g
α, ν	3.3	1.1	1.1
a	0.82	0.02	196
b	2.5	1.9	2.8
c	800	5.1	124
d	1.0	0.27	0.66
C		5	5×10^5
x		1	-0.5

crystals and snowflakes. In purple the growth mechanisms of r_i (BER,DEP). Green lines demonstrate the expansion of the snowflakes (RIM, AGG, ACC). Graupel (r_g) forms as an effect of heavy riming (RIM), by collision of larger raindrops with snowflakes (ACC), by WET/DRY growth or by contact freezing of raindrops (CFR). All graupel growth processes are indicated by blue lines in Figure 2.5.2, were hail formation is included.

2.5.3 ADJUSTMENT OF ICE3 INSIDE MEPS

Since the ICE3 scheme showed some weaknesses for the winter month, [Müller et al. \[2017\]](#) introduced some modifications. During cold conditions the ICE3-scheme showed too low temperature at two meter, too much ice fog and all year long was the occurrence of cirrus overestimated. After implementing the modifications described in [Müller et al. \[2017\]](#) the two meter temperature bias was reduced as well as an improvement of low-level clouds was shown. A negative aspect of these adjustments was that the occurrence of fog increased.

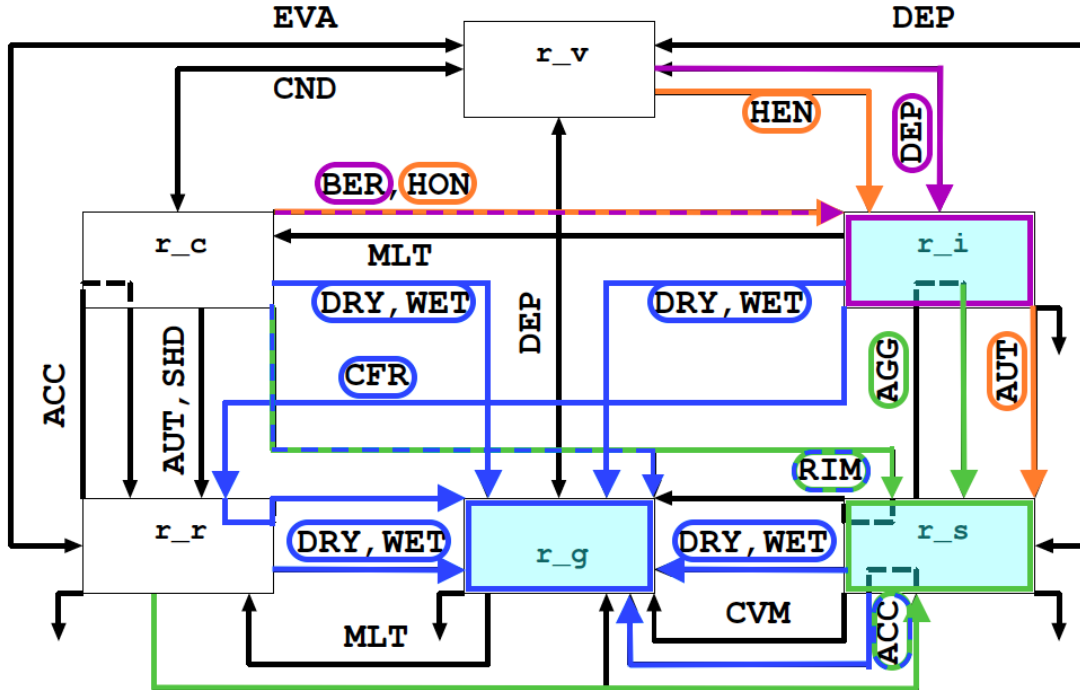


Figure 2.5.2: Microphysical processes for mixed phase clouds in the ICE3 scheme adapted from [Meteo France \[2009\]](#). In orange the initiation processes for primary ice r_i and snowflakes r_s . The growing processes of r_i is shown in purple and for r_s in green. Graupel particles, r_g , grow from existent particles and the processes are shown in blue.

2.6 NUMERICAL DATA TRANSFORMATION

The following section will describe how the different variables were processed to achieve a comparison between the retrieved values and the forecast model output.

2.6.1 LAYER THICKNESS IN MEPS

To compare the measurements from the surface with the MEPS data, the closest grid point to Haukeliseter, is used.

MEPS has a vertical resolution in hybrid sigma pressure coordinates, where one is at the surface and decreases with height. To calculate the actual vertical pressure in Pa, a formula is provided in the OPeNDAP Dataset of `meps_full_2_5km_*.nc` by the [Norwegian](#)

Meteorological Institute [2016].

$$p(n, k, j, i) = a_p(k) + b(k) \cdot p_s(n, j, i) \quad [\text{Pa}]. \quad (2.6.1)$$

p_s is the surface air pressure in Pa, and information about the variables a_p , b are not given from the access form. **Find reference for sigma-hybrid coordinate transformation equation.**

The next step was to convert pressure-levels into actual heights by the use of the hypsometric equation. Here, the air temperature in model levels is used to calculate the mean temperature of each layer.

$$\bar{T} = \frac{\int_{p_2}^{p_1} T \partial \ln p}{\int_{p_2}^{p_1} \partial \ln p} \quad [\text{K}] \quad (2.6.2)$$

For the numerical integration, the Simpson rule was used, which is a build-in function in Python.

Martin [2006] presents steps of differentiating the hypsometric equation by using the virtual air temperature. But when the atmospheric mixing ratio is large, will the virtual temperature only be 1 % larger than the actual air temperature. Since the error is little calculations are done with the provided air temperature in model levels.

The thickness, Δz , of each layer is then be found by using the hypsometric equation from Martin [2006] and the previously calculated mean temperature (Equation (2.6.2)):

$$\Delta z = z_2 - z_1 = \frac{R_d \bar{T}}{g} \ln \left(\frac{p_1}{p_2} \right) \quad [\text{m}] \quad (2.6.3)$$

where R_d is gas constant for dry air with a value of $287 \text{ J kg}^{-1} \text{ K}^{-1}$, standard gravity $g = 9.81 \text{ m s}^{-2}$. p_1 and p_2 are the pressure levels at lower and higher levels, respectively ($p_2 < p_1$). To gain the respective height of each pressure layer, Δz is summed.

2.6.2 SNOW WATER CONTENT

To get a valid comparison between the SWC from the optimal estimation retrieval and the results from MEPS, the SWC is averaged over each hour. Taking the model initialisation

of MEPS at 0 UTC the model produces forecast values at 0, 1, 2, ..., 22, 23, ..., 66 UTC. To approach hourly mean values from the retrieval SWC an average over 30 min prior and 29 min after each full hour is performed. This leads to a match of the average value at the same time as from MEPS.

Since MEPS has a higher vertical resolution than the optimal estimation snowfall retrieval each vertical profile of SWC is averaged every 200 m. To accomplish the same vertical resolution only values above 100 m are used to start at the same range height as given from the MRR (Section 2.3.2).

Within the output from MEPS snow water content does not exist for each model layer. Hence the calculation of the SWC is performed by using the three solid precipitation categories given in MEPS. Namely the instantaneous mixing ratio of snowfall (r_s), graupel fall (r_g) and the atmosphere cloud ice content (r_i). The mixing ratios are represented in kg kg^{-1} and a transformation to gm^{-3} is performed. Densities in each model level (ρ_{ml}) are calculated and then multiplied with the sum of the solid precipitation mixing ratio.

$$\rho_{ml} = \frac{p_{ml}}{R_d T} \quad [\text{kg m}^{-3}] \quad (2.6.4)$$

$$SWC_{ml} = \rho_{ml} \cdot (r_s + r_g + r_i)_{ml} \cdot 10^6 \quad [\text{gm}^{-3}]. \quad (2.6.5)$$

2.6.3 SNOW WATER PATH

The snow water path (SWP) is the vertically integrated value of the averaged SWC (Equations (2.4.1) and (2.6.5)), where the numerical Simpson's integration is applied.

$$\int_{h_0}^{h_1=3000\text{m}} \text{SWC}(h) dh \approx \frac{h_1 - h_0}{6} \left[\text{SWC}(h_0) + \text{SWC}(h_1) + 4\text{SWC}\left(\frac{h_0 + h_1}{2}\right) \right] \quad [\text{gm}^{-2}] \quad (2.6.6)$$

The snow water path is a measure of the weight of ice particles per unit area. It indicates the total amount of ice in the atmosphere.

2.6.4 ENSEMBLE MEAN AND COEFFICIENT OF VARIATION

Check literature of meaning

The ensemble mean is the average of all ten ensemble members of MEPS.

$$\bar{x} = \frac{\sum_{i=1}^n x_i}{N} \quad (2.6.7)$$

The ensemble spread is known as the standard deviation with respect to their mean of the model output. That means it shows the variation around the center or control run.

$$\sigma = \sqrt{\frac{\sum_{i=1}^n (x_i - \bar{x})^2}{N-1}} \quad (2.6.8)$$

for either variable is the dimension of the standard deviation the same.

To verify how well MEPS performed during the Christmas storm a variation of the SWC is calculated. For this, the standard deviation (Equation (2.6.8)) is divided by the ensemble mean (Equation (2.6.7)).

2.6.5 DEW POINT TEMPERATURE FOR SKEW-T LOG-P DIAGRAM

The Python module pyMeteo is used to calculate the dew point temperature of each ensemble member to study the stability of the atmosphere (<https://pythonhosted.org/pymeteo/>, last visited: 25.01.2018). The additional package thermo.py is able to calculate the dew point temperature if the pressure and the specific humidity in each level are known.

$$e_l = \ln \left(\frac{\frac{q_v}{\epsilon} \cdot \frac{p}{100}}{1 + \frac{q_v}{\epsilon}} \right) \quad (2.6.9)$$

$$T_d = 273.15 + \frac{243.5 \cdot e_l - 440.8}{19.48 - e_l} \quad [\text{K}] \quad (2.6.10)$$

where, q_v is the specific humidity, p pressure in [Pa], $\epsilon = R_d/R_v = 0.622$ with R_v gas constant for water vapour.

CHAPTER 3: ANALYSIS OF THE CHRISTMAS STORM 2016

This extreme weather event is chosen since MEPS just became operational and in addition surface snow instruments where installed to profile the vertical at Haukeliseter. Preliminary test showed the overestimation of snow accumulation by MEPS compared to the measurements at the ground. Furthermore, changed the phase of precipitation from solid to liquid to solid.

The next sections will give a definition of an extreme weather event, a description of the different weather maps, and a synoptic interpretation of the storm and why mixed phase precipitation was observed at Haukeliseter.

Before the analysis each weather maps' purpose will be presented to understand the connections between them. For this, the ECMWF operational model Cycle 43r1 are used. The analysis consists of 137 model levels and to reduce computational costs is it reduced to the *octahedral reduced Gaussian grid* and then interpolated to a N640 Gaussian grid. Between the pole and the equator are 640 lines of latitude equally symmetric spaced. This follows 1280 latitude lines for each hemisphere. The resolution along the longitude is $90^\circ/640$ lines with points getting closer with increasing latitude. This follows a total number of grid points of $8 \cdot 640^2$ [Dando, 2016].

3.1 EXTREME WEATHER

'Extreme weather' is a meteorological term, associated with the extent of a weather type. The Norwegian Meteorological Institute declares an extreme event, if strong winds, large amounts of precipitation and large temperature changes are expected before the event

occurs. As well as a large avalanche risk is present and coastal areas are influenced by extremely high-water levels. All this occurred during the Christmas storm [Olsen and Granerød, 2017]. The average wind along the coast of Western Norway had hurricane strength (observed: 40 ms^{-1} to 55 ms^{-1}). In South and Eastern Norway west to north-west winds between 25 ms^{-1} to 40 ms^{-1} were measured. At the Haukeliseter measurement site, 136.4 mm of precipitation were monitored during 21 December 2016 to 27 December 2016. This event was just above the limit of been called an extreme weather. Generally, an event is divided into four phases that it can be called extreme [Pedersen and Rommetveit, 2013].

Phase A: *Increased monitoring before the possible extreme weather.* The meteorologists give special attention to the weather situation. At this point it is not certain, that there will be an extreme weather event.

Phase B: *Short-term forecasts.* It is decided, that there will be an extreme event. The forecasts are more detailed, and updates will be published at least every six hours. The event will get a name.

Phase C: *The extreme weather is in progress.* The meteorologists send out weather announcements at least every six hours.

Phase D: *The extreme weather event is over. Clean-up and repairs are in progress.* When the extreme weather is over the public is notified and information about the upcoming weather and clearing work is given.

3.2 DYNAMIC TROPOPAUSE MAP

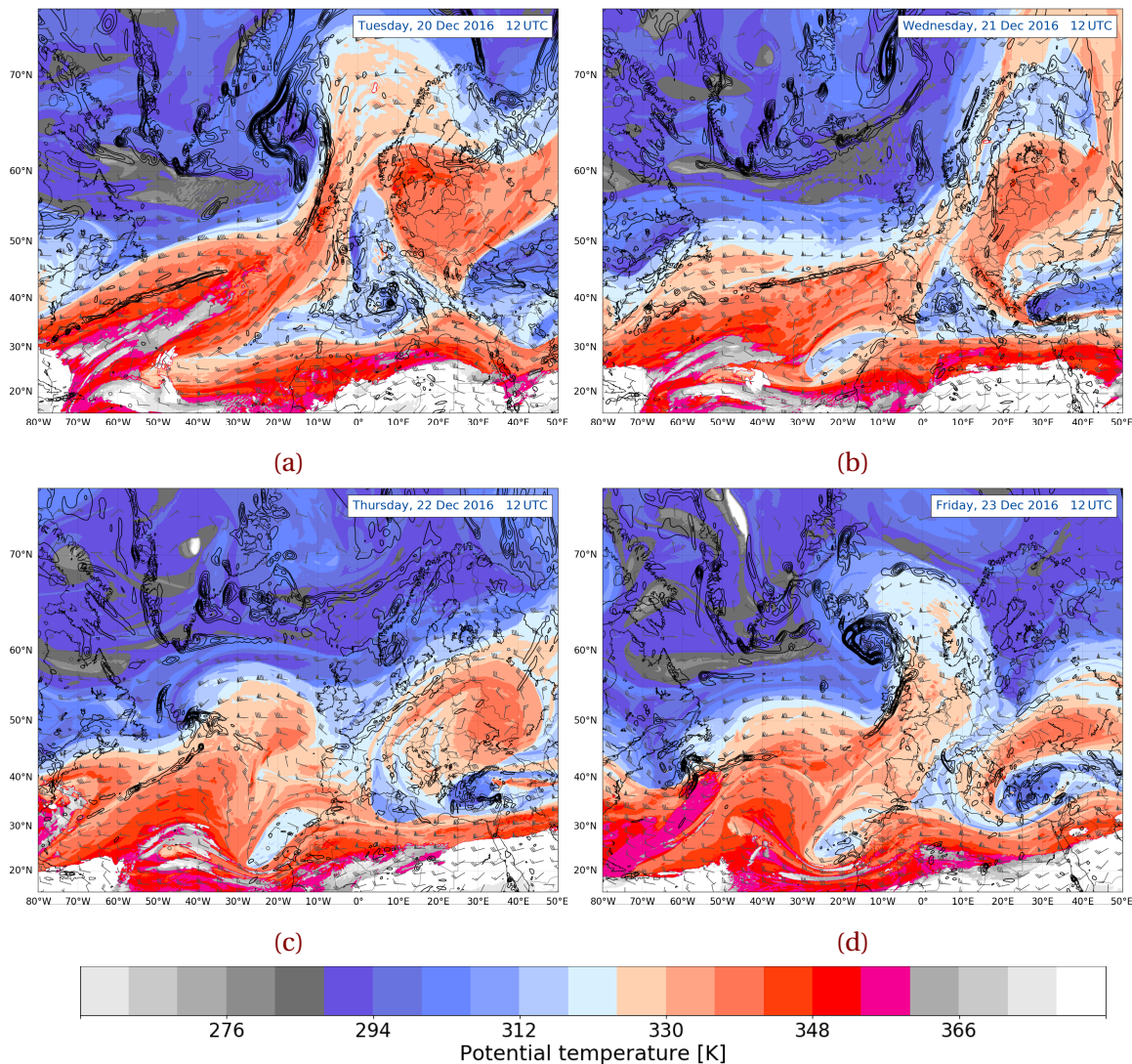
The dynamic tropopause map (DT), shown in Figure 3.2.1 presents the potential temperature distribution at the tropopause. Colder tropopause is associated with colder colours and vice versa warmer tropopause with warmer colours (shading according to the colorbar). Therefore, a warmer tropopause indicates an elevation of the atmospheric column.

The gradient at the 2 PVU (1 PV unit = $10^{-6} \text{ m}^2 \text{ s}^{-1} \text{ K kg}^{-1}$; Hoskins et al. [1985]) surface, between the cold and warm area indicates the thermal wind. There is a slope between the cold and warm surfaces increasing towards the warmer column averaged temperature. An increased slope means also an increased pressure gradient force with increasing height and therefore an increase in geostrophic wind. This means, that there exists a vertical

wind shear. From this, the mid-latitude jet stream can be pointed out. **do I need to present the equation of thermal wind?** Wind barbs in m s^{-1} indicate the direction of the wind flow, which is generally from west to east in the mid-latitudes.

The 925 – 850 hPa layer-averaged surface relative vorticity is shown in black contours, every $0.5 \times 10^{-4} \text{ s}^{-1}$. It represents the rotation of a fluid. **Does the relative vorticity need more explanation?**

Along the Rossby-Wave-Guide, troughs and ridges are seen which can be combined with the surface relative vorticity to understand the vertical dynamic interaction in the atmosphere. In case of a westward tilt between the surface cyclone and an upper level through an intensification of the surface cyclone is more likely to occur.



3.3 THICKNESS, SEA LEVEL PRESSURE, MOISTURE, AND WIND AT 250 hPa

A good overview gives the sea level pressure, 1000–500 hPa thickness map and winds at 250 hPa. Figure 3.3.1 shows, that it combines several important features of the vertical distribution within the atmosphere, for example.

Black contour lines indicate sea level pressure in hPa and makes it possible to observe cyclones and anticyclones at the sea surface.

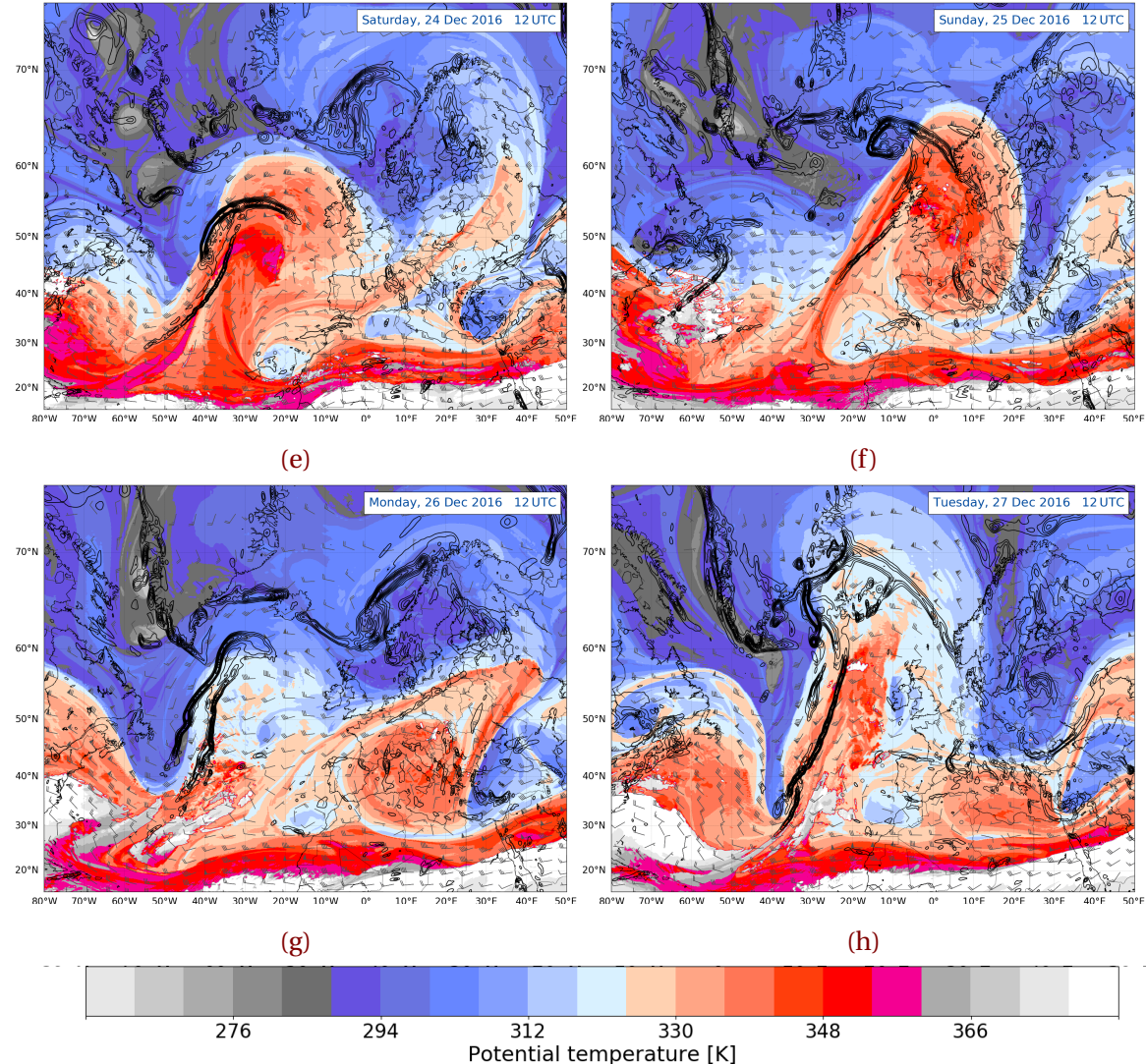
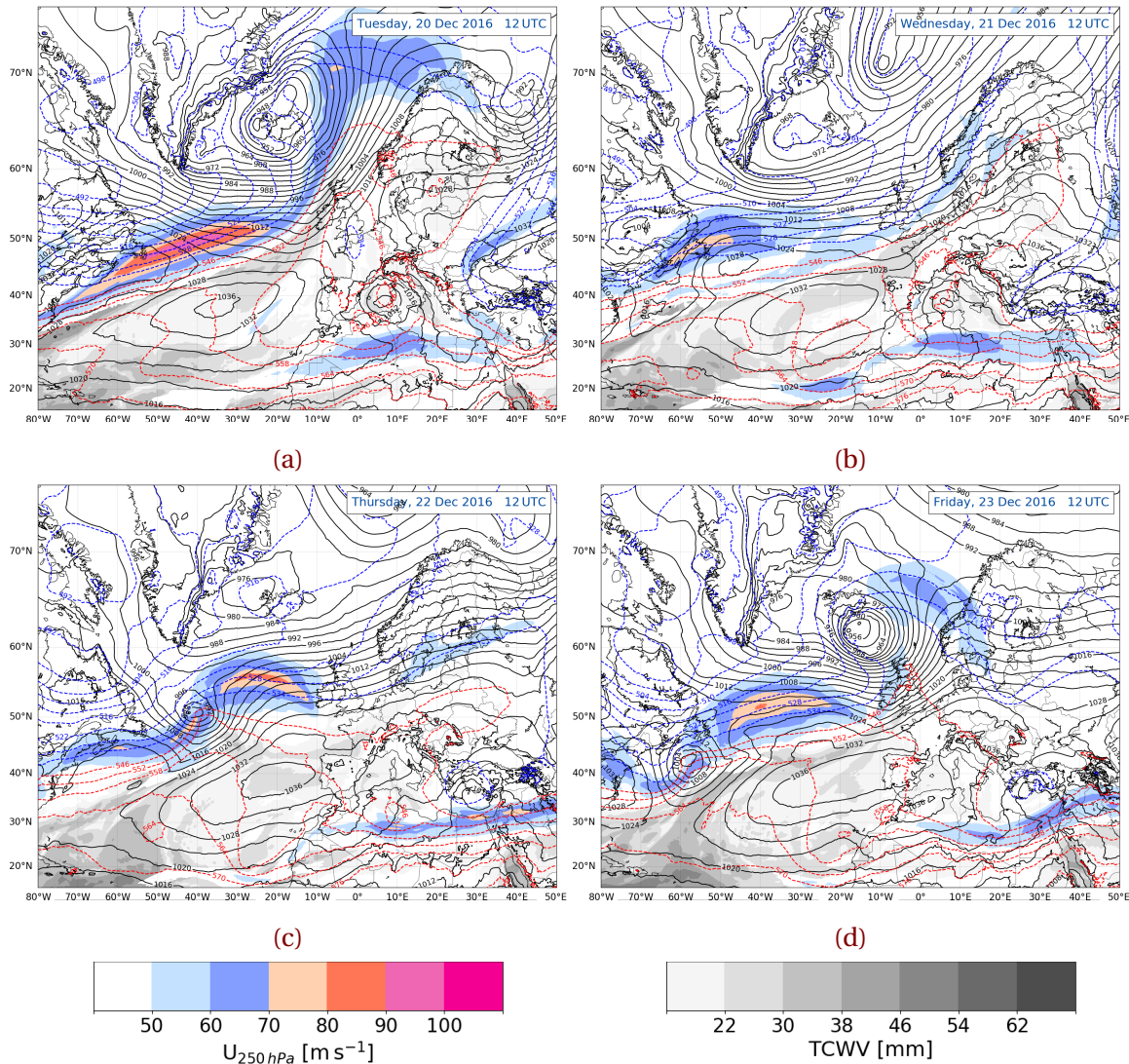


Figure 3.2.1: Dynamic tropopause analysis map, data from ECMWF at 2 PVU. During 20 December 2016 to 27 December 2016. Potential temperature [K] at the 2 PVU surface, shaded according to the colour bar. Total wind, barbs [m s^{-1}], and 925–850 hPa layer-averaged surface relative vorticity (black contours, every $0.5 \times 10^{-4} \text{ s}^{-1}$).



The dashed, coloured contours show the vertical thickness between the 1000 hPa and 500 hPa surface, every 6 dam. The thickness between two pressure levels can be related to the hypsometric equation (Equation (2.6.3)). This is a relation of the mean temperature of the air between two pressure levels. Thus, high values of thickness mean relative warm, moist air (red, dashed). This can then be associated to rain or snow in mid-latitudes, depending on cold or warm air advection.

Grey shaded areas describe total precipitable water in the atmosphere in mm. It is an indicator for the amount of moisture to supply rainfall and will be used to identify where moisture was present.

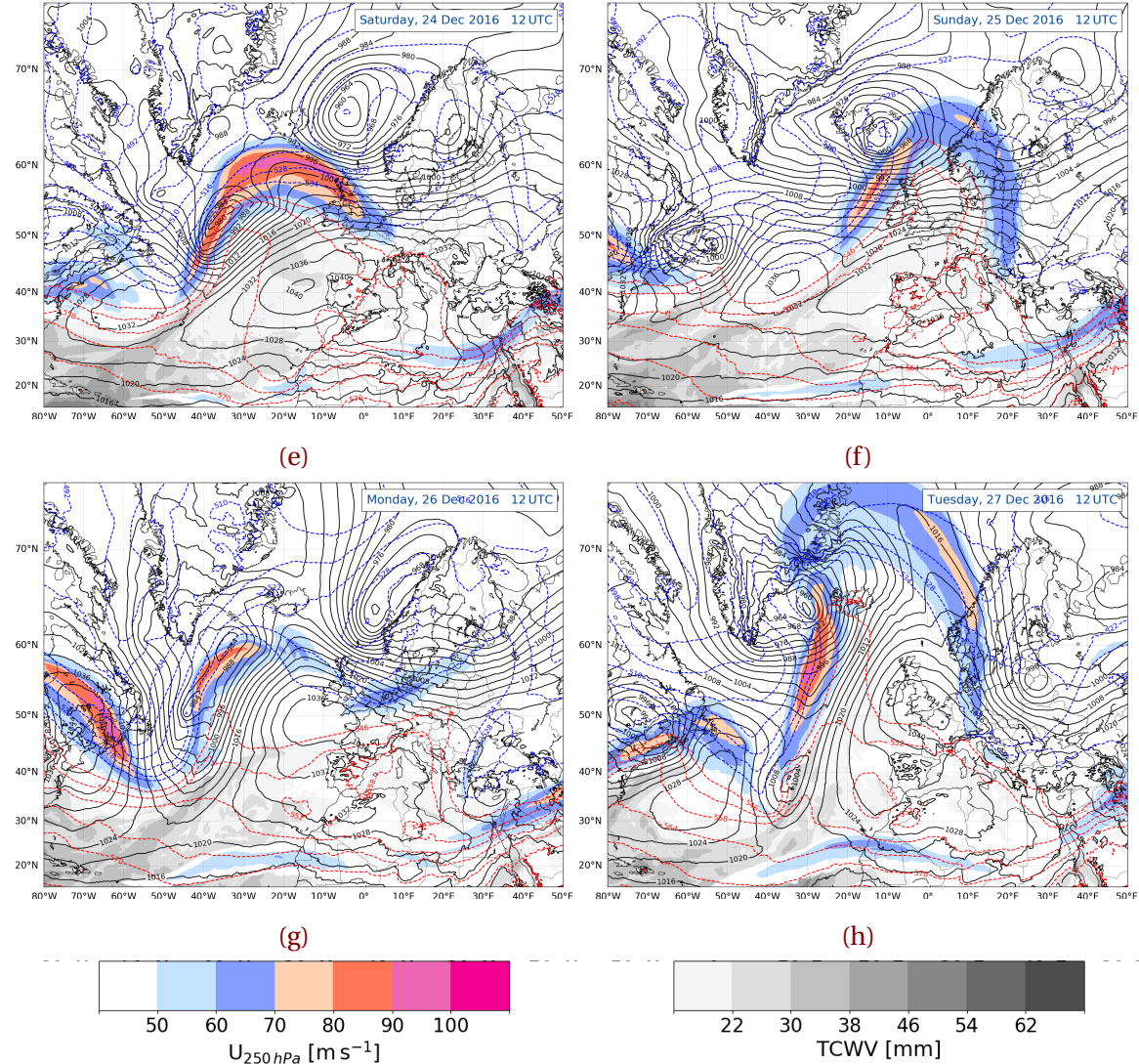
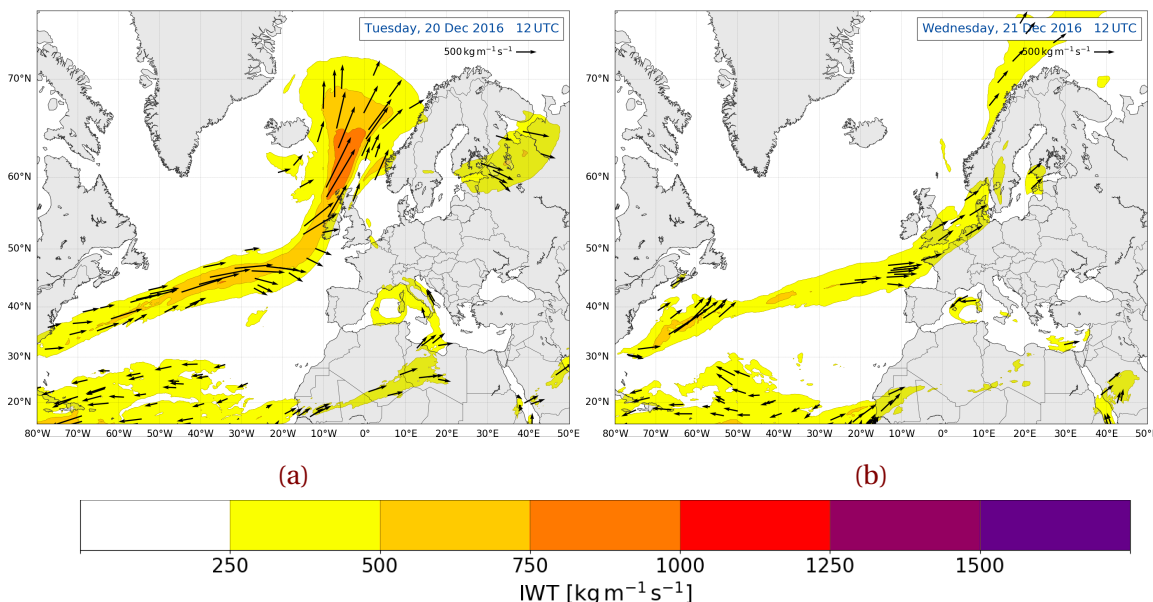


Figure 3.3.1: Jet, thickness, mean sea level pressure, and moisture synoptic analysis, data from ECMWF. During 20 December 2016 to 27 December 2016. 250 hPa wind speed, shaded according to the colour bar, $[\text{ms}^{-1}]$. 1000 – 500 hPa thickness, dashed contours every 6 dam, MSLP, black contours every 4 hPa, total column water vapour [mm], shaded according the grey scale.

Colour shaded contours in Figure 3.3.1 indicate the mid-latitude jet streaks at 250 hPa. Warmer colour is associated with higher wind speeds at this level.

3.4 ATMOSPHERIC RIVER MAP



An atmospheric river (AR) is a filament structure of intense moisture transport from the tropics to higher latitudes. Heavy precipitation can be associated with it, because the air is warm and moist. This can often be observed at mountain ranges at west coasts such as in Norway [include reference here](#). Due to orographic lifting will the moisture be released and follow high amounts of precipitation.

An atmospheric river is characterised if the integrated vapour transport shows values higher than $250 \text{ kg m}^{-1} \text{s}^{-1}$ and is a continuous region larger than 2000 km [Rutz et al., 2014]. The integrated vapour transport (IVT) was calculated from the ECMWF data as followed:

$$IVT = \frac{1}{g} \int_{p_{sfc}}^{100 \text{ hPa}} q \mathbf{V} dp \quad [\text{kg m}^{-1} \text{s}^{-1}] \quad (3.4.1)$$

where g is the standard gravity, q the specific humidity, and \mathbf{V} the total wind vector at each pressure level p . The numerical, trapezoidal integration is performed by using data

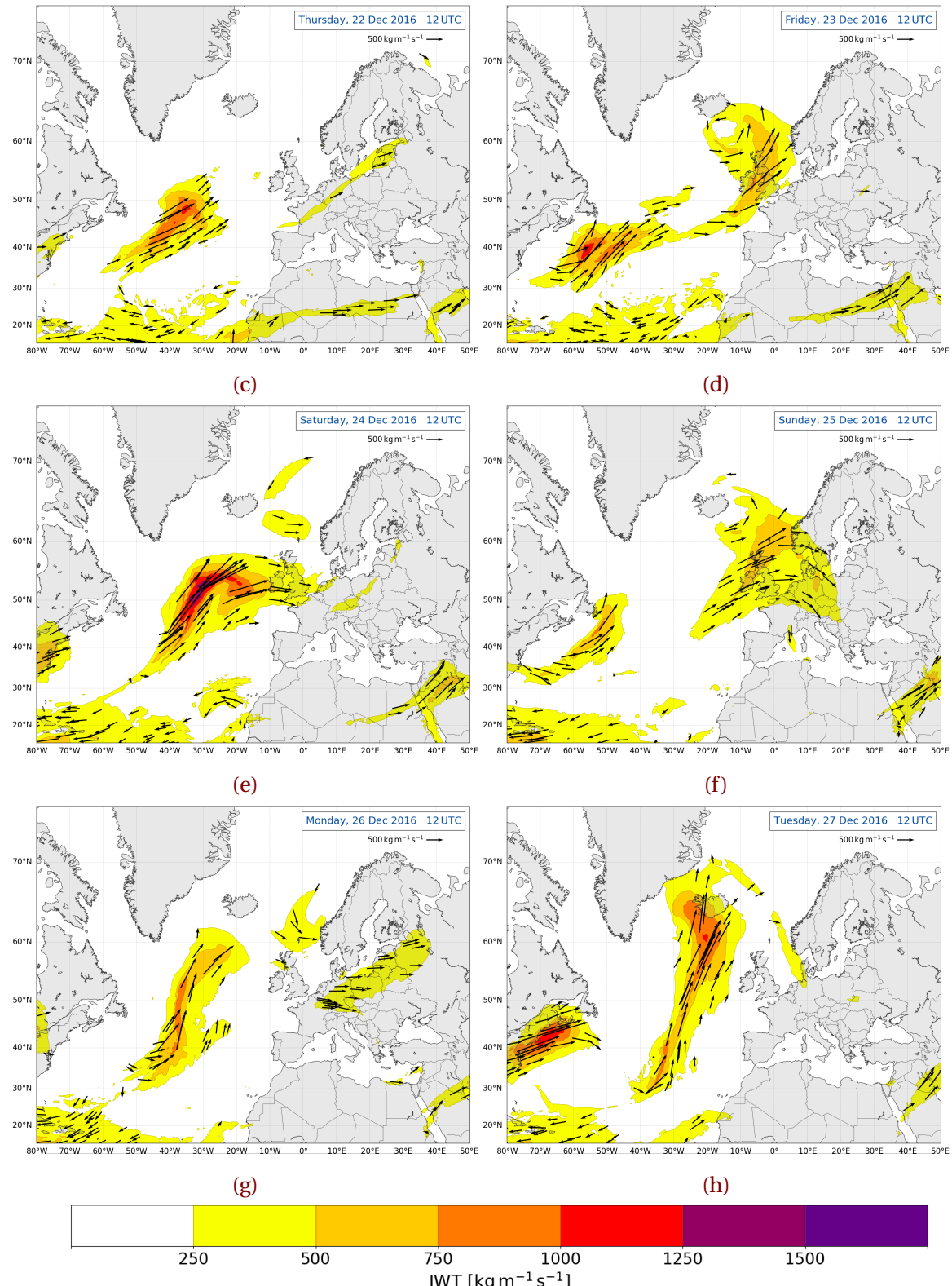


Figure 3.4.1: Atmospheric river analysis map, data from ECMWF. During 20 December 2016 to 27 December 2016. IVT, shaded according to the colour bar [$\text{kg m}^{-1} \text{s}^{-1}$]. Vectors, indicating the direction and magnitude of the IVT.

Table 3.5.1: Damage related to wind speed, from Færaas et al. [2016].

slight storm	$20.8 \text{ ms}^{-1} - 24.4 \text{ ms}^{-1}$	Large trees sway and hiver. Roofs can blow down.
full storm	$24.5 \text{ ms}^{-1} - 28.4 \text{ ms}^{-1}$	Trees are pulled up with clutter. Big damages to houses.
strong storm	$28.5 \text{ ms}^{-1} - 32.6 \text{ ms}^{-1}$	Extensive damage.
hurricane	$>32.6 \text{ ms}^{-1}$	Unusually large destruction.

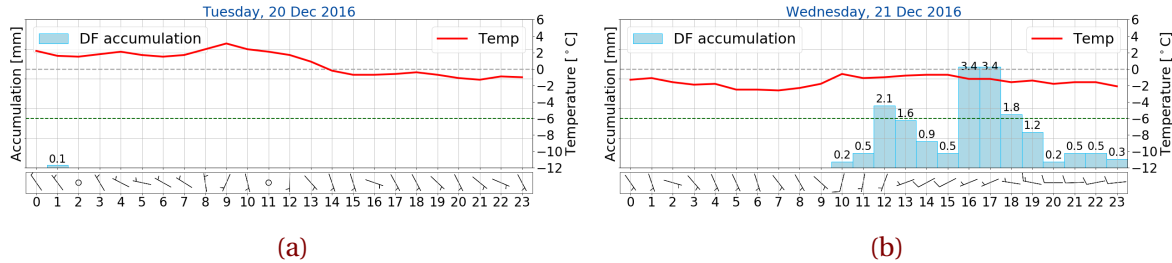
from the surface pressure p_{sfc} to 850 hPa in 50 hPa intervals and from 700 hPa to 100 hPa in 100 hPa intervals.

Figure 3.4.1 shows coloured contours of the integrated vapour transport (IVT) in $\text{kg m}^{-1} \text{s}^{-1}$, where warmer colours indicate higher IVT. Stream vectors indicate the direction and intensity of the IVT flow.

3.5 OBSERVATIONS AT THE WEATHER MAST

The large scale synoptic analysis will be related to the local weather observations at Haukeliseter.

60 min accumulation is presented as bars in Figure 3.5.1 and will show the continuous precipitation at Haukeliseter during the extreme event. The possible change of precipitation will be investigated with the temperature. Snow fall is likely for temperatures up to 2 °C. The intensity of the storm can be classified by the hourly averaged wind speed and direction as wind barbs in ms^{-1} . To understand which damage a storm can have, Færaas et al. [2016] released a table to associate wind strength with damage (see Table 3.5.1).



3.6 RADIOSONDE FROM STAVANGER

The Appendix A.1 includes images of vertical temperature profiles of Radiosondes from Stavanger, represented in a Skew-T log-P diagram. The vertical profiles extend from surface up to 300 hPa. (Note, that the representation of the vertical scale (in m) differs with each sounding from day to day.)

The vertical temperature distribution will identify the stability of the atmosphere and give information on convection and thickness of clouds. Furthermore, warm air and cold air advection can be identified by observing the change of wind with height.

Black and green line represent the atmospheric and dew-point temperature, respectively.

3.7 LARGE SCALE CIRCULATION

Everything has to get into relation with the Radiosondes, Figure A.1.1. How to do that? Any suggestions? They took me some time to make, so I want to include them!

21 December 2016

The dynamic tropopause map in Figure 3.2.1b shows that Norway is influenced by a change of elevated tropopause to a suppressed tropopause during 20 December 2016 to 21 December 2016. Hence the potential vorticity changed from positive to negative at the tropopause and cold air stretches right over Norway. A good amount of moisture is transported from the low latitudes to high latitudes, influencing Norway's' west coast. This can be seen in the surface maps (Figure 3.3.1b) as well as in the atmospheric river maps (Figure 3.4.1b). The westerly flow in Figure 3.3.1b is conducive to orographic lifting. The precipitation was probably snow when having a look at the moisture content and the

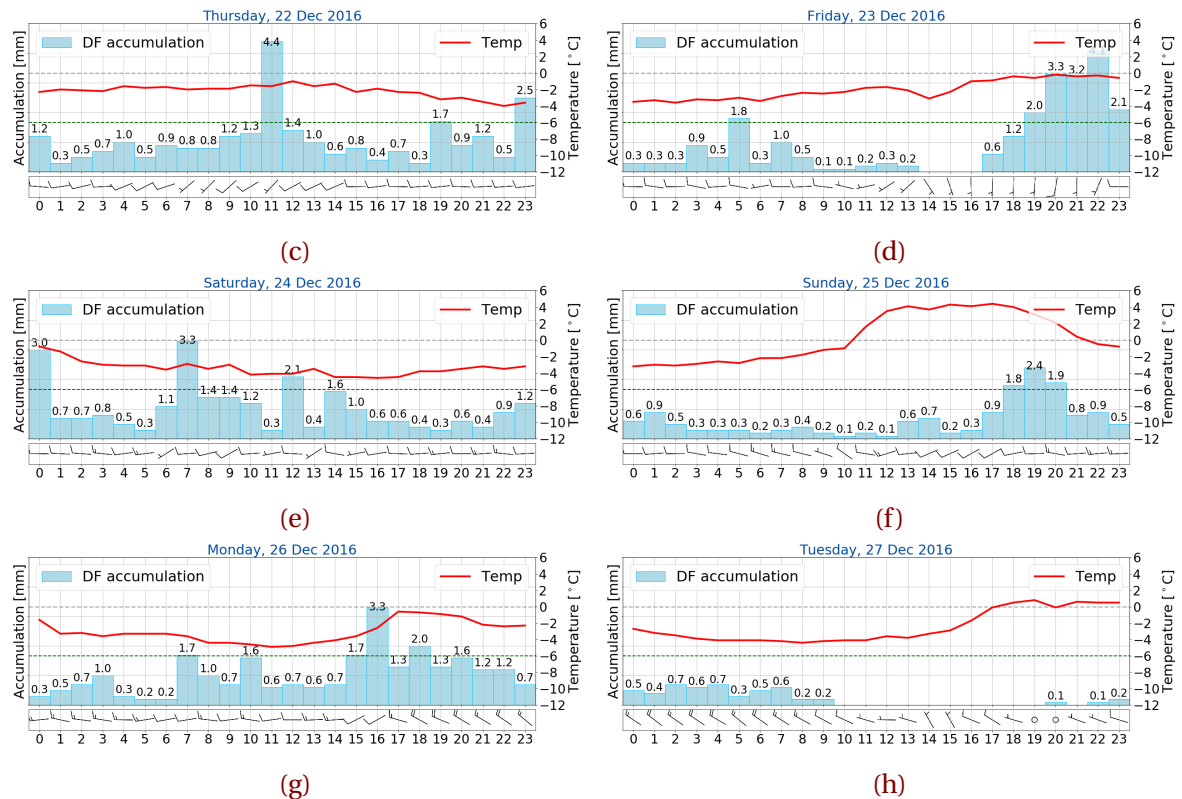


Figure 3.5.1: Observation from the weather mast at Haukeliseterd during 20 December 2016 to 27 December 2016. 60 min total accumulation [mm] in light blue as bar, temperature (red, $^{\circ}\text{C}$), and wind as barbs $[\text{m s}^{-1}]$. Gray dashed line indicates the freezing temperature and the green dashed line the 30-year climate mean temperature at -6°C . Hourly processed data taken from [eklima \[2016\]](#).

cold air. The change from warm air to cold air can also be observed in the time series of temperature in Figure 3.5.1b. And the westerly flow, combined with a good amount of vapour transport from the tropics led to orographic lifting and precipitation at the Haukeliseter site. At around 60° W a formation of a cyclone at the baroclinic zone can be implied.

22 December 2016

Twenty-four hours later the analysis shows from 22 December 2016 phasing between the surface relative vorticity and the baroclinic zone at 50° N in the DT. The centre of the surface low is directly located below the temperature gradient at the 2 PVU surface, hence this is good for synoptic lifting. Furthermore, the strongest baroclinicity is observed on the south west side of the surface low. The synoptic map of the geopotential thickness and the surface pressure show the beginning of the frontal boundaries in Figure 3.3.1c. At the same time shows the AR map, Figure 3.4.1c, large values just at the baroclinic zone, where the low pressure is beginning to form. **Help?! Does that lead to even more lifting in this area? Or does it just mean that the cyclone gets a good amount of moisture?!**. Norway is located in a cold area. The continues precipitation observed at Haukeliseter (Figure 3.5.1c) is associated with the westerly flow which is conducive to orographic lifting, and therefore moisture release.

23 December 2016

The begin of the ridging on the 22 December 2016 is more pronounced 24 h later. The warmer air pushes away the cold air, which covered Norway. The low-pressure system moved north-east and lies south of Iceland. The occluded front of this system passes through Haukeliseter, which is why a temperature 'jump' observed at 14 UTC. After this, Southern Norway is influenced by the warm sector, monitored as a temperature increase. The AR, as well as the total column water vapour amount in Figure 3.4.1d and Figure 3.3.1d, respectively show the amount of moisture, transported from low latitudes.

At the same time forms a second cyclone at the baroclinic zone at 40° N. The atmospheric river map (Figure 3.4.1d) indicates a large amount of moisture at this latitude. Again, moist, warm air is conducive to intensify the surface cyclone. In addition, shows the DT map a

phasing between the low-level vorticity and the upper level baroclinic zone.

24 December 2016

After the passage of the cold front over Norway, Scandinavia is within colder air (compare Figure 3.2.1e and Figure 3.3.1e for 24 December 2016). Over the Atlantic warmer air starts to push the colder air northward. **something something with the low-level vorticity and lifting; lifting at the right entrance region of the jet streak, and very high IVT.**

At Haukeliseter negative temperature up to -4°C is observed, compare Figure 3.5.1e. The westerly flow is again conducive for orographic lifting and associated precipitation.

25 December 2016

Twenty-four hours later the ridge is more pronounced and covers large parts of Norway. The surface low south-east of Iceland has built its frontal boundaries, which can be seen in the low-level vorticity of Figure 3.2.1f. The warm front lies west of Haukeliseter and starts to be observed at the measurement site (compare Figure 3.5.1f for 25 December 2016). Figure 3.4.1f indicating the integrated vapour transport shows that a lot of moisture is transported from the Atlantic, towards Great Britain and south-western Norway. Together with the lifting at the surface boundary a sufficient amount of precipitation is observed. Since the ridging brings moister (Figure 3.4.1f), warm air (Figure 3.2.1f) and Norway lies in a warm sector (Figure 3.3.1f) the assumption will be made, that the precipitation changed from solid to liquid.

26 December 2016

Within the next twenty-four hours the cold front passed through (temperature change in Figure 3.5.1g for 25 December 2016 to 26 December 2016). Norway is covered in cold air (Figure 3.2.1g). The surface low-level indicates the occlusion of the cyclone and therefore a weakening. The wind is still from the west which is helpful for orographic lifting. The moisture content is still present but much weaker and smaller in extend. Since Norway is covered in cold air, the temperature is below zero and the precipitation had to be solid.

27 December 2016

The images of 27 December 2016 show that the storm passed and disappeared. Southern Norway lies in cold air (Figure 3.2.1h), but on the right exit region of the jet (\rightarrow sinking motion of cold air), compare 3.3.1h. A small amount of moisture is present (Figure 3.4.1h). Because of the wind change from west to north-west follows that orographic lifting is not present and the precipitation amount decreases at the end of the storm.

CHAPTER 4: RESULTS AND DISCUSSION

In this chapter the results of the surface observation, the optimal estimation retrieval and the regional mesoscale forecast model are presented. On the basis of the methodology described in Chapter 2 it should be evaluated if a regional mesoscale forecast model predicts the same synoptic patterns as observed at the measurement site. Also, vertical SWC forecasted by MEPS is being verified with the retrieved SWC at Haukeliseter. It should be paid attention to the fact, that this study is very unique of its kind. As far as the author has knowledge was no approach done to verify a vertical regional forecast model with the help of vertical observation measurements.

4.1 AGREEMENT BETWEEN SURFACE OBSERVATIONS

To be able to compare the vertical predicted snow water content with the retrieved snow water content is a verification of the surface accumulation made. If the retrieved surface accumulation is confident in comparison to the double fence measurement, then the vertical can be trusted.

The correlation in Figure 4.1.1a demonstrates a good agreement between the 48 h accumulation measured by the double fence and the retrieved surface accumulation. The black line in Figure 4.1.1a presents a linear correlation with a regression coefficient of $R = 0.97$. In general, is the retrieved surface snowfall accumulation underestimated when compared to the double fence measurements, but not with a large degree.

Figure 4.1.1b shows the difference between retrieved accumulation and observed accumulation by the double fence. For the time period 20 December 2016 to 24 December 2016 indicates Figure 4.1.1b an underestimation of retrieved snow accumulation of less than -5 mm for the first 24 h. Snow accumulation calculated on 23 December 2016 at 0 UTC

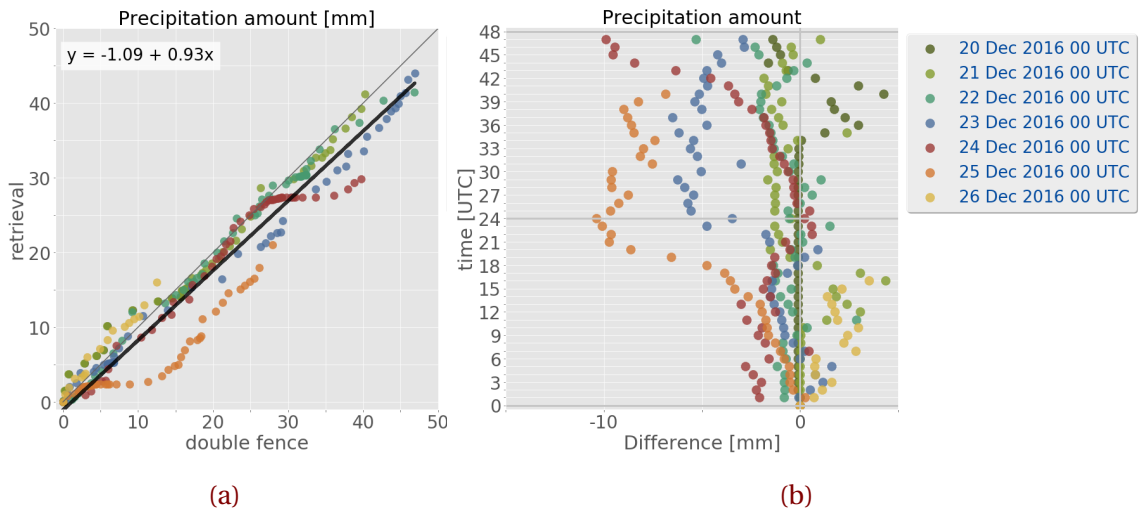


Figure 4.1.1: Scatter plot comparing the observed and retrieved 48 h surface accumulation (a). In black the linear regression between the two systems. b: Difference between the retrieved surface accumulation and the observed accumulation by the double fence. The colours represent the days of the storm with the start of calculated 48 h accumulation at 0 UTC. Accumulations starting on the 25 December 2016 are not a fair comparison because of observed liquid precipitation.

show after 24 h an underestimation by the retrieval of up to -6.5 mm. larger underestimation is related to the observation of liquid precipitation on 25 December 2016 between 12 UTC to 21 UTC for accumulations on 24 December 2016 after 43 h. On 25 December 2016 no fair comparison to the double fence measurement can be performed after 12 UTC because of the neglection of precipitation when temperatures exceed 2°C .

The mean absolute error of all days is 2.06 mm (excluding values on 25 December 2016 after 12 UTC and on 26 December 2016 after 17 UTC because of attenuation at the MRR). For a 48 h accumulation follows for the Christmas storm (20 to 26 December 2016) an average error of -23.4% . For shorter, 24 h accumulation decreases the average error to -9.6% .

Similar to this study used Cooper et al. [2017] a CloudSat snow particle model, PSD and fall speed from MASC observations for five snow events at Barrow, Alaska. The comparison to the weather station followed an error of -16% for all five snow events. The usage of a particle model for hex columns, slope parameters estimated from the MASC and fall

speed assumptions from the doppler velocity followed an average difference error of the individual events of 21 %.

Table 4.1.1: Observed (obs.) and retrieved (ret.) snowfall amounts for the Christmas storm 2016. Difference refers to the difference of the retrieved and observed snow accumulation after 24 h and 48 h. The average is the value over all seven days, including the ignored values after 12 UTC on 25 December 2016 and after 17 UTC on 26 December 2016.

Day	24 h				48 h			
	Snowfall		Difference	Average	Snowfall		Difference	Average
	[mm]		[%]	[%]	[mm]		[%]	[%]
	obs.	ret.			ob.	ret.		
20 Dec	0.1	0.002	-97.8	-23.4	16.9	15.5	-8.2	-9.6
21 Dec	17.1	16.6	-2.7		40.2	41.2	+2.6	
22 Dec	25.6	25.1	-2.1		46.8	41.5	-11.3	
23 Dec	23.3	19.8	-14.9		46.9	44.0	-6.2	
24 Dec	24.8	25.0	+0.8		39.7	29.8	-24.9	
25 Dec	15.4	-	-		39.8	-	-	
26 Dec	25.1	-	-		30.0	-	-	

Table 4.1.1 shows the difference error for each individual day and the average difference error over seven days. The choice of the correct PSD model, slope parameters and fall speed shows a good agreement with the observations at Haukeliseter for the Christmas storm (Table 4.1.1). It indicates also that the non-uniqueness of snow accumulation is reduced, when using a combination of ground-based observations. Of course, more storms should be investigated to find the exact correlation between the surface observations and the estimated accumulation to see if the error keeps as small for different snow patterns at Haukeliseter. During the Christmas storm is the average error for 24 h accumulation almost similar to Barrow, Alaska. It turns out that there is no relation between high precipitation and low precipitation since the difference error varies. Cooper et al. [2017] also showed different combinations of PSD assumptions and fall speed. For Barrow, best agreements between observations and retrieved snowfall were found by using the here presented approach.

On 20 December 2016 is the difference error large (-97.8%) this is probably related to the observation of precipitation at the double fence, but the MRR did not receive the occurrence of precipitation. That the double fence observed precipitation might be related to some particles stirred up by wind. Neglecting the values from 20 December 2016 reduces the average error to -4.7% for 24 h accumulation. This follows a much lower average value than at Barrow and a very good agreement between observed and retrieved snow accumulation. In Section 4.4 will the vertical SWC be compared to the forecasted MEPS values for the Christmas storm. The small average error for 21 December 2016 to 26 December 2016 will be useful to trust the vertical observations when comparing to the forecast, but it should be kept in mind that retrieved snow accumulation is underestimated and therefore may the vertical SWC be too low.

4.2 OBSERVATION OF LARGE SCALE WEATHER PHENOMENA AT THE SURFACE

One of the main factors, that made this particular case so interesting is the fact, that several times in the six-day period frontal boundaries passed over Norway. One aim of this work is to determine if large scale features were observed at the measurement site.

A comparison between the surface observations at Haukeliseter and the ECMWF analysis of the dynamic tropopause maps show that frontal passages occurred on three days during the Christmas storm (Figure 3.3.1 and 3.2.1). These frontal boundaries show in the surface observations and ensemble forecasts on 23 December 2016, 25 December 2016 and 26 December 2016. A typical cyclone has a prevailing warm front and a faster moving cold front. As the storm gets more intense and the cold front rotates around the low-pressure centre and catches the warm front the cyclone will begin to occlude. Changes in pressures, temperature, wind direction and wind speed can occur. In some cases, an intensification of the precipitation can be observed as well.

Figure 4.2.1 shows the different parameters forecasts initialised at 0 UTC for 23 December 2016, 25 December 2016 and 26 December 2016, as well as the observations at the Haukeliseter measurement site in dash-red. Typical pressure decreases and increases, as well as temperature increases, and wind changes are present on 23 December 2016 and 26 December 2016. The 25 December 2016 shows only an increase of temperature leading to the assumption

of a warm air passage.

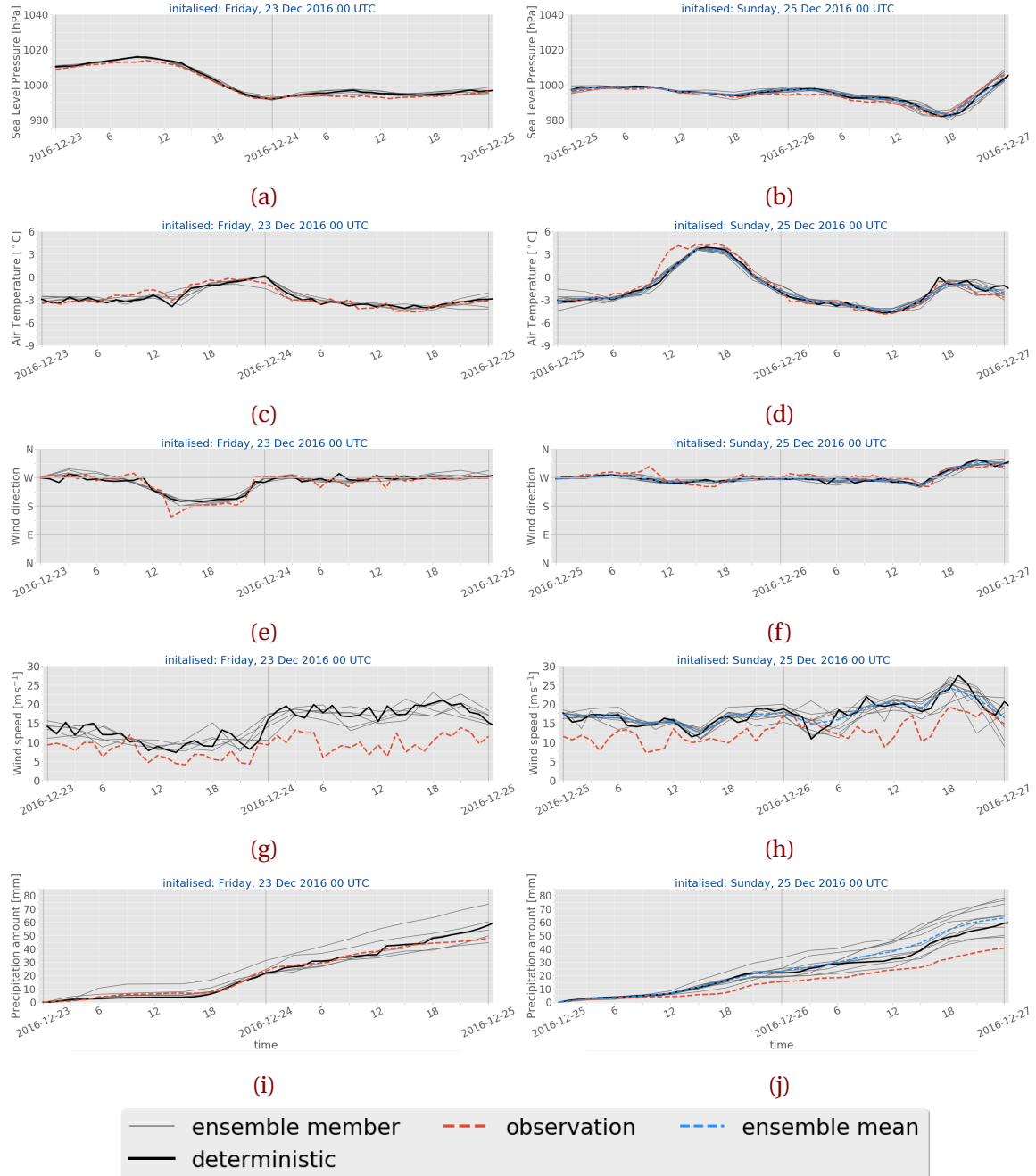


Figure 4.2.1: 48 h surface observations and ensemble forecasts initialised on the 23 December 2016 at 0 UTC (left column, a, c, e, g, i), and on 25 December 2016 at 0 UTC (right column, b, d, f, h, j) as well as 26 December 2016 (k, l, m, n, o). Line representation according to the label. Upper panel sea level pressure, second 2 m air temperature, third and fourth 10 m wind direction and speed, respectively, and lowest panel precipitation amount.

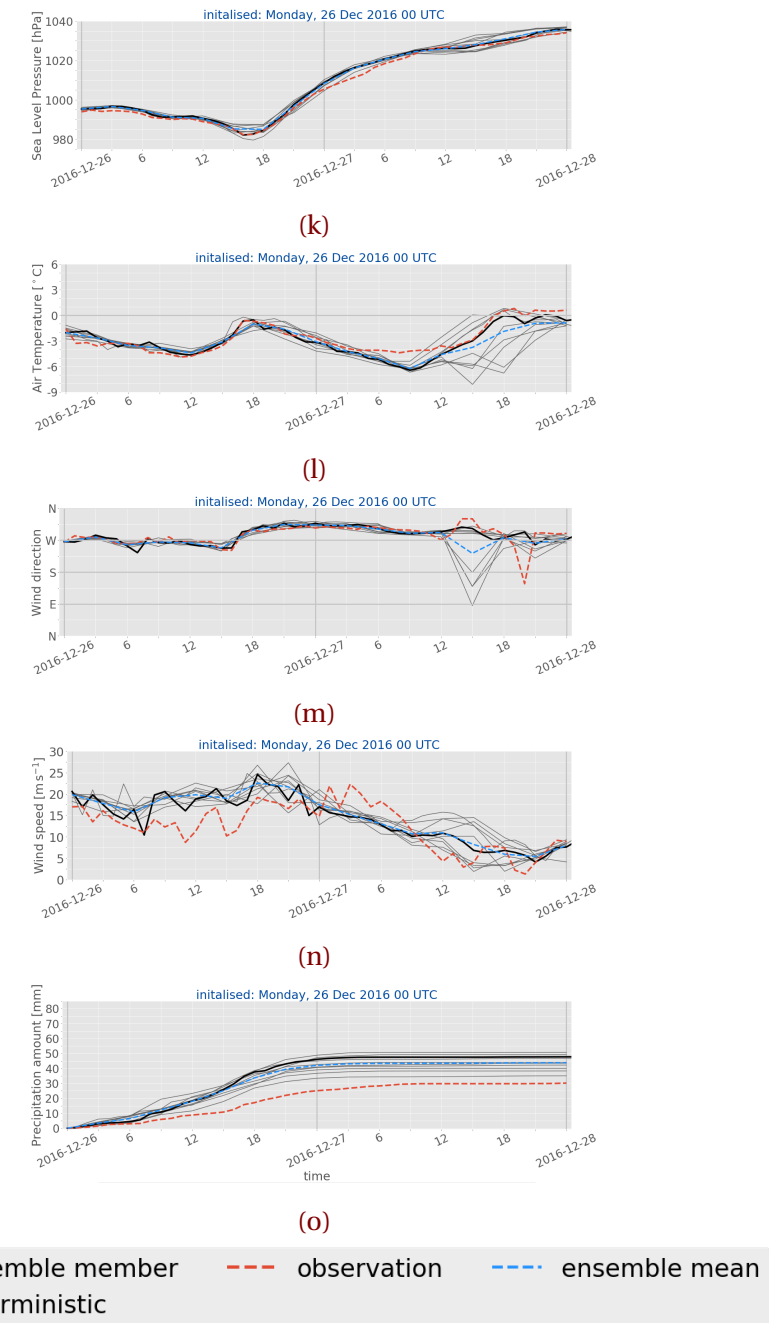


Figure 4.2.1: (Continued from previous page.) Initialisation 26 December 2016 at 0 UTC.

As described in Section 3.7 shows the ECMWF dynamic tropopause analysis map (Figure 3.2.1d) more ridging and therefore warmer air over Southern Norway on 23 December 2016. The low-pressure system approaches in the course of the day south-east of Iceland and hence stronger west to south west wind are associated with the cyclone (Figure 3.3.1d). The MEPS forecast, initialised on 23 December 2016 0 UTC in Figure 4.2.1a follows the observations and shows the decrease in pressure after 12 UTC due to the passage of the occluded front with a constant pressure after the transition. Since warmer air is more advected to the North and the DT in Figure 3.2.1d shows a warm low-pressure core, an increase in temperature was observed and predicted at the measurement site (Figure 4.2.1c). As the cyclone is advected to the north-east, closer into the Norwegian Sea, a wind change can be seen in the analysis map from ECMWF (Figure 3.3.1d). First west wind and later south-west wind was associated with the low-pressure system. The MEPS forecast and observations in Figure 4.2.1e and g indicate a wind change from west to south with a slight decrease in wind speed.

On 23 December 2016 was the passage of the occlusion also observed by an increase in precipitation. Before 18 UTC shows the surface accumulation light precipitation. During the passage of the occluded front increases the observed surface accumulation and is associated to continuous, heavy precipitation.

Similar patterns were seen for the passage of the occluded front on 26 December 2016 in the ECMWF analysis Figure 3.2.1g and 3.3.1g. In this case the low-pressure system was located north of Morø og Romsdal in the Norwegian Sea. In the morning was the cyclone located east of Iceland and in the course of the day it got closer to the coast of Norway. Before landfall at 16 UTC indicates Figure 4.2.1k a pressure decrease. During the passage the sea level pressure reaches its lowest point of 985 hPa and increased afterwards during the dissipation of the Christmas storm. Pressure, temperature, and wind changes were already forecasted for initialisations on 25 December 2016, only wind speed and precipitation seem not to agree with the observations at Haukeliseter.

Since the cyclone was surrounded by colder air (south of the low-pressure system) first a drop and then an increase of temperature were observed and forecasted by MEPS. An indication of the passage is also seen in the 10 m wind observations and forecasts. As the cyclone is east of Iceland with a westward large-scale surface wind (?? and ??), shows Figure 4.2.1m west wind with observed strength up to 17.5 m s^{-1} (Figure 4.2.1n). During



Figure 4.2.2: MASC images of falling water drops observed on 25 December 2016 at 17 UTC from three different angles. Not all parts of the liquid sphere are equally illuminated.

the passage changes the wind direction to north-west with higher wind speed which can be associated to the location of the low-pressure system and the closer surface isobars (Figure 3.2.1g).

The precipitation was continuing throughout the day, with light to moderate precipitation before the passage and heavy precipitation around 16 UTC followed by moderate to light.

While on 23 December 2016 and 25 December 2016 the precipitation was associated with a passage/landfall of an occluded front, was the 25 December 2016 marked by the transition of a warm sector. The ECMWF analysis showed a ridging at the DT surface. The surface cyclone core is south east of Iceland in Figure 3.2.1f with two associated frontal boundaries. While the warm front is approaching the west coast, is the cold front north west of Great Britain. The cold fronts tail moved into lower latitudes, following the slow-down of the cold front, leading to a stationary frontal boundary. Furthermore, the mid-latitude jet is aligned along the surface frontal boundaries (??), while the Haukeliseter site is located below the left jet exit region. This leads to rising motion at the surface.

Neither pressure nor wind observations and forecasts indicate the passage of any frontal boundary. The only indication of the transition is seen in the increase of temperature at 11 UTC until 21 UTC (Figure 4.2.1d). In Figure 4.2.1f a small wind change was observed by the wind mast at 10 UTC. This development from west to north-west was not forecasted by MEPS, it rather estimated strong west winds.

In Figure 4.2.2 are the surface observations from the MASC during the passage of the warm

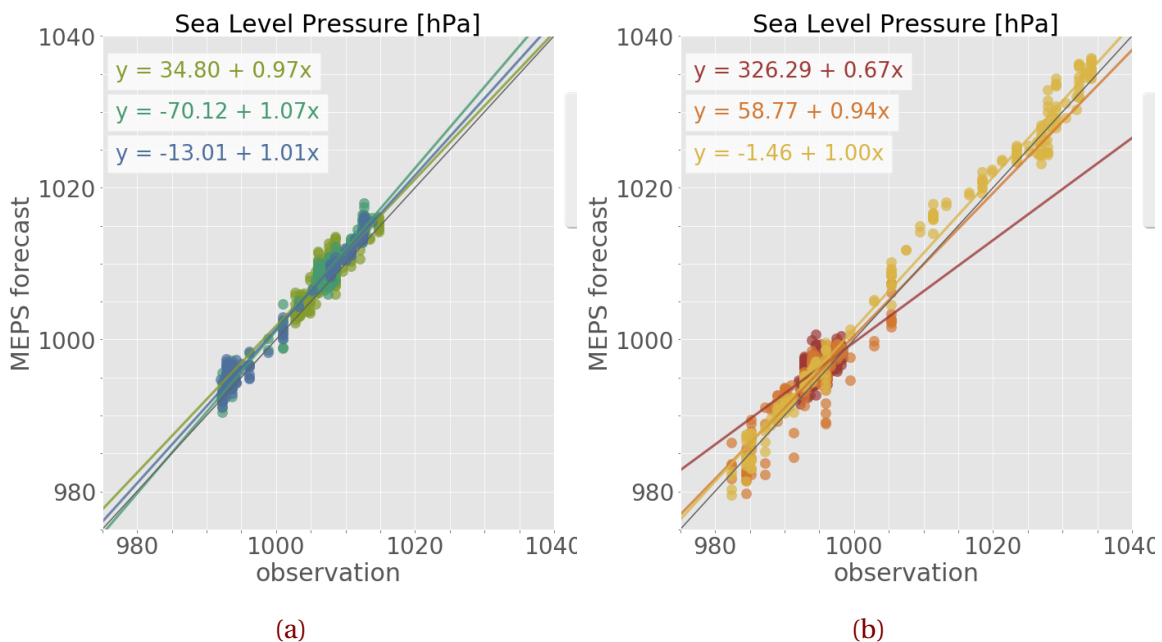


Figure 4.2.3: 48 h scatter plots for surface observations and ensemble forecasts initialised for 21 December 2016 to 23 December 2016 (left column, **a, c, e, g, i**) and for 24 December 2016 to 26 December 2016 (right column, **b, d, f, h, j**). Sea level pressure.

sector. Without the images taken around 17 UTC it would not be possible to verify that liquid precipitation occurred at the Haukeliseter site. Together with the increase in surface temperature in Figure 4.2.1d it is qualified that at least the warm sector of the low-pressure system appeared at the measurement site.

The comparison between the ECMWF analysis displays, that the ensemble member forecast system MEPS covers the prediction of large scale phenomena like frontal boundaries and liquid precipitation at the surface. Figure 4.2.3 presents the correlation between the observations and the 48 h ensemble forecast. The relation between Haukeliseter observations and the forecast members is indicated by the regression line for each day.

Sea level pressure has the best correlation under all variables. The best agreement shows on 26 December 2016 when the Christmas storm made landfall and dissipates after the passage of the occluded front at 16 UTC. Dahlgren [2013] showed that by mixing in large scale information from the boundary condition (ECMWF) into the regional model, the

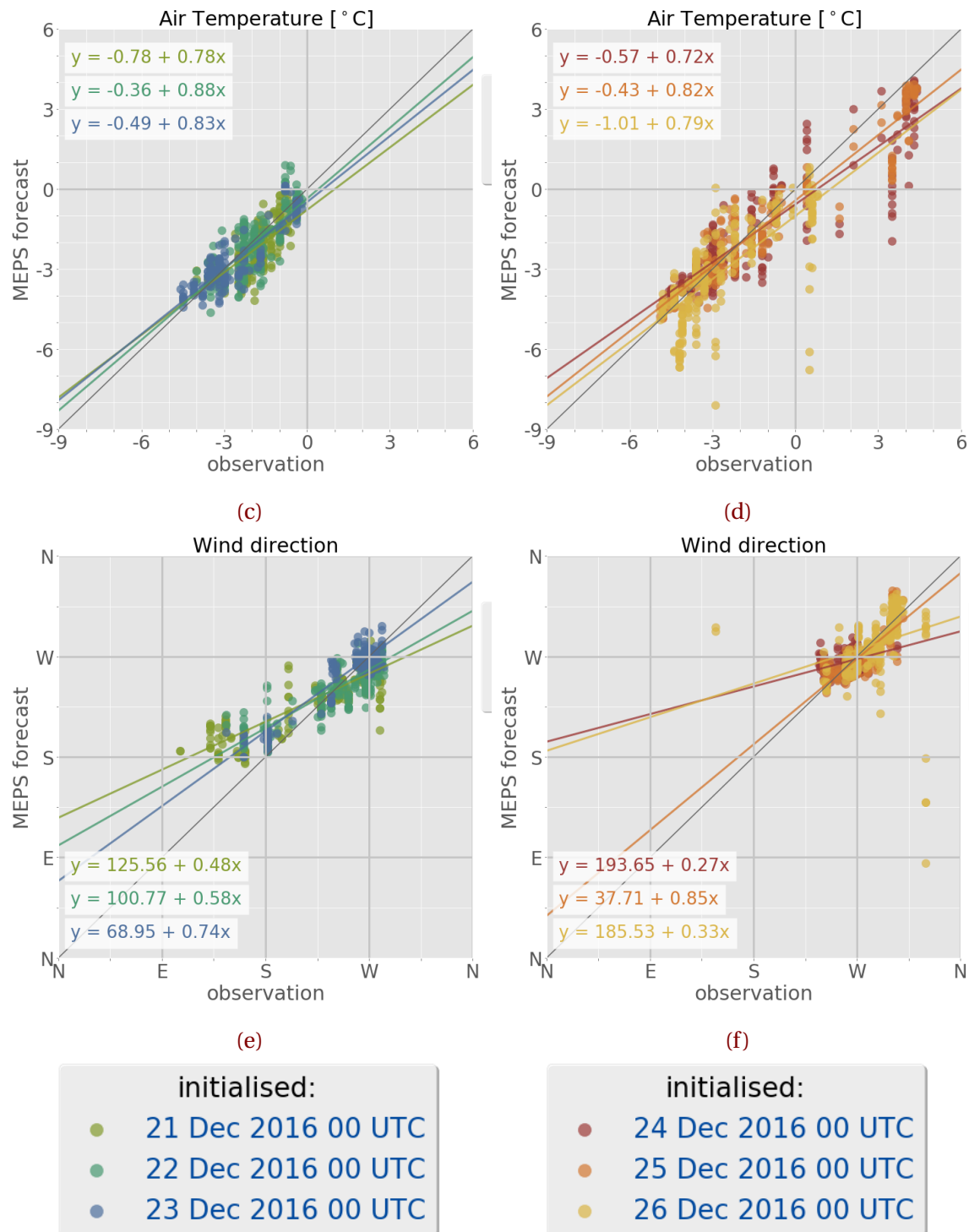


Figure 4.2.3: (Continued from previous page.) Upper panel 2 m air temperature, second panel 10 m wind direction.

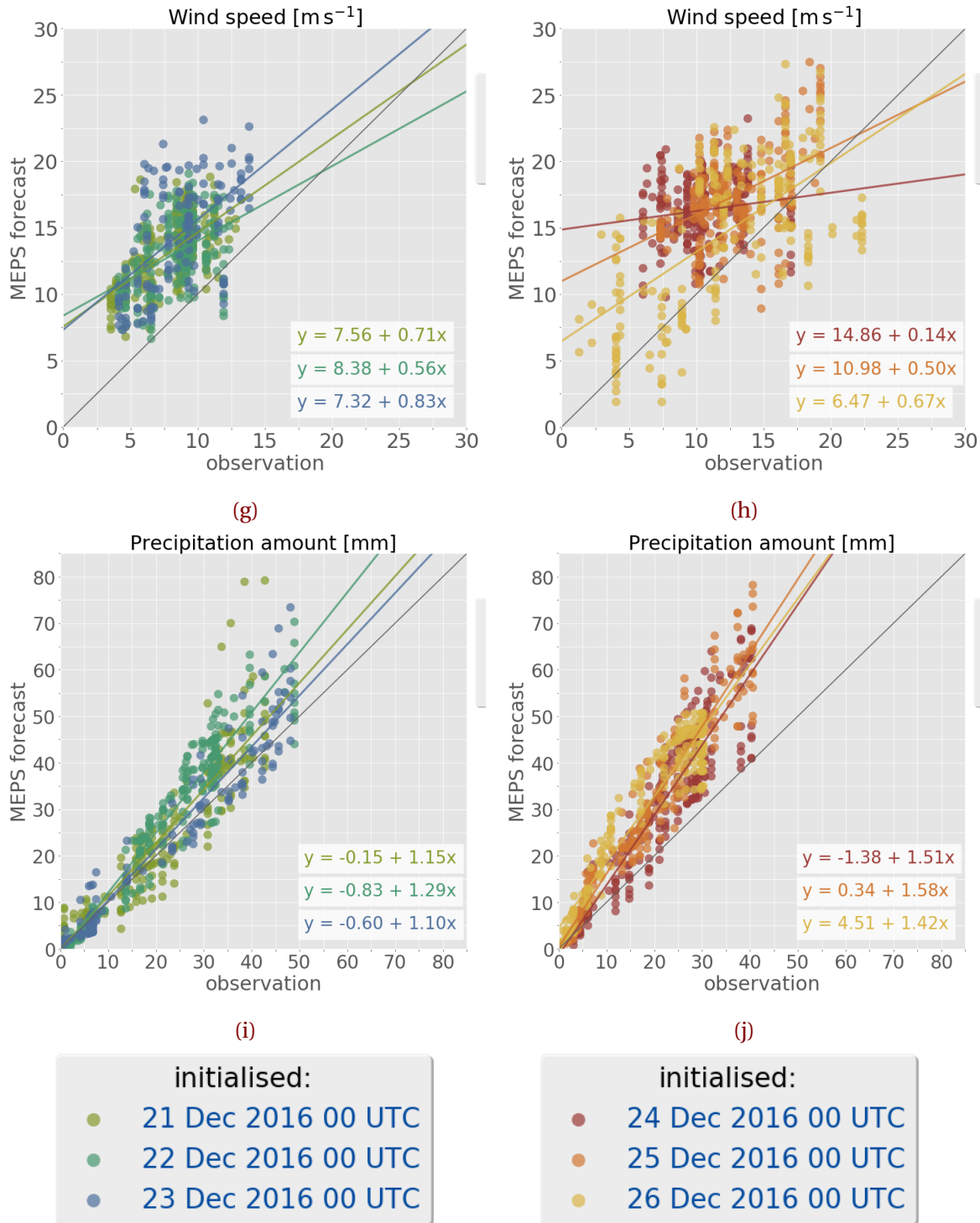


Figure 4.2.3: (Continued from previous page.) Upper panel 10 m wind speed, lower panel surface precipitation amount.

forecast for sea level pressure will be improved. The model-observation comparison by Dahlgren [2013] showed a declination of forecasts after 24 h Since the pressure values are in good agreement with the observations is it assumed that the warm front did not pass through at Haukeliseter on 25 December 2016 and only the warm sector is observed. This shows a quite detailed forecast ability of MEPS, as from the ECMWF analysis it is not quite clear where the warm front passed through.

Figure 4.2.3d indicates a moderate correlation between observation and the 48 h ensemble member forecast system. In general, underestimated MEPS the observed temperature, but it estimated it at the correct timing on 25 December 2016. The previous operational model AROME-MetCoOp showed a negative winter bias after winter 2012 [Müller et al., 2017]. Figure C.2.1c shows for 23 December 2016 and 26 December 2016 positive as well as negative biases for the individual members. The 25 December 2016, where the warm sector was observed shows a negative bias, underestimating the temperature when compared to the observation. The mean error for the Norwegian model domain of AROME-MetCoOP estimated by Müller et al. [2017] is smaller than 1.8 K for the surface temperature in December 2014. The forecasts for 23 December 2016, 25 December 2016 and 26 December 2016 show mean absolute error values of up to 0.61 K, 0.77 K and 1.44 K. It shows by using an ensemble forecast system a reduction of mean errors and an increase in forecast accuracy. During the Christmas storm 2016 high wind speeds were observed at the Haukeliseter site (Figure 4.2.3g and h). According to Müller et al. [2017] are large wind speeds significantly better simulated for AROME-MetCoOp compared to ECMWF's forecast. The wind speeds are still overestimated, which is an already known difficulty in the deterministic version of MEPS. In AROME-MetCoOp wind speed prediction agreed better with observations for wind speeds between 3 m s^{-1} to 13 m s^{-1} than ECMWF forecasts did, showing the advantage of a high-resolution weather model. With increasing wind speed the forecast accuracy decreases with a mean absolute error below 2 m s^{-1} for December 2014 in AROME-MetCoOp. The mean absolute error for wind speed during the Christmas storm is higher at all days ranging from 3 m s^{-1} to 7 m s^{-1} . During the three days with frontal passages shows the 23 December 2016 the highest mean absolute error of 6.5 m s^{-1} , more than three times as high as the monthly averaged value from Müller et al. [2017]. Their study case in February 2015 showed a slight overestimation of ECMWF 10 m wind compared to the Norwegian AROME-MetCoOp domain.

Haukeliseter is a measurement site exposed to high wind speeds [Wolff et al., 2013, 2015]

the ensemble prediction system MEPS seems to still have issues forecasting the wind speed correctly in mountainous terrain. Figure 4.2.1 indicates that MEPS is able to estimate larger scale features which is probably related to the outer boundary conditions of ECMWF described by Dahlgren [2013]. In general, were surface parameters well predicted, only wind speed and precipitation accumulation showed overestimation in MEPS. Wind speeds forecasted higher than observations, is probably related to the weakness of wind speed prediction already known from the previous operational model AROME-MetCoOp. On the 25 December 2016 and 26 December 2016 MEPS also overestimated the precipitation amount at the surface. This will be further discussed in Section 4.3.

4.3 SURFACE SNOWFALL ACCUMULATION

One approach of this study is to see if observed surface accumulation was correctly predicted by the regional weather model MEPS. Precipitation amount at the surface are shown in Figure 4.3.1. The figures are representing the observed surface precipitation accumulation in mm over 48 h. Accumulation, measured by the double fence are presented as red hexagons. Minutely retrieved surface snowfall amount in dash-dotted green. The ten 48 h forecast ensemble members are lines in black and grey, the deterministic and its perturbed ensemble members, respectively. The blue dashed line shows the ensemble mean of all ten members. Since the deterministic and the first ensemble member are having values every hour and the other perturbed members only every three hours, shows the ensemble mean the precipitation amount at 0 h, 3 h, ..., 21 h, 24 h, ..., 48 h forecast time. When too few ensemble members were present, like on 23 December 2016, no ensemble mean is calculated (Figure 4.3.1c). Underneath is the associated 10 min average wind of the last hour from the 10 m weather mast at Haukeliseter, to see if surface accumulation observations may be influenced by wind.

Figures 4.3.1a to 4.3.1c show in general a better agreement between observations and forecast for 48 h forecasts initialised on 21 December 2016 to 23 December 2016 at 0 UTC. The spread of the ensemble member around the control runt fit better to the observations as well than initialisations on 24 December 2016 to 26 December 2016. During these days gets the low-pressure system more intense and closer advected to the Norwegian coast and influencing the local weather in Norway (??). Figures 4.3.1d to 4.3.1f indicates a larger

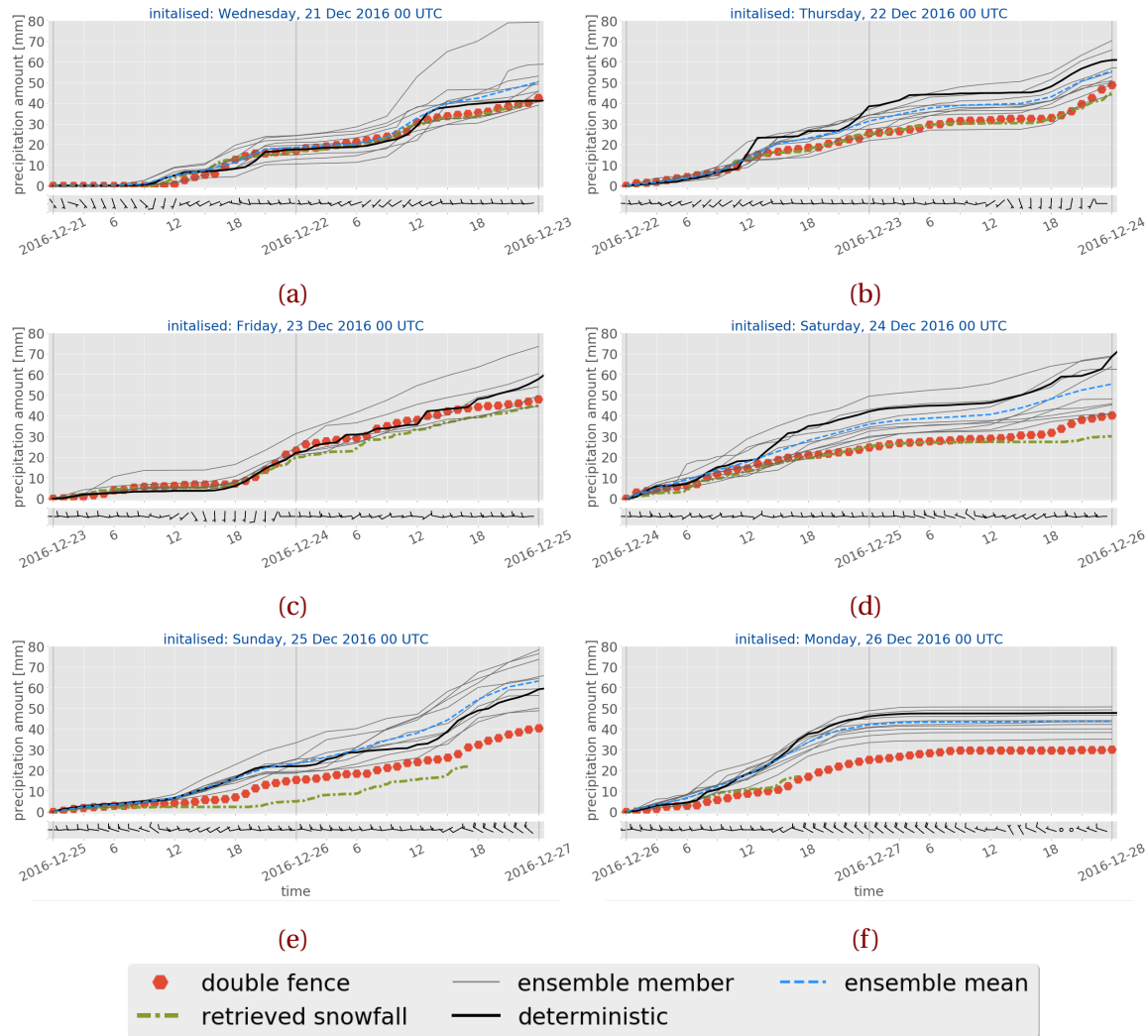


Figure 4.3.1: 48 h surface snowfall accumulation for 21 December 2016 to 26 December 2016 (a-f). Representing the values from the double fence in red, hexagons; optimal estimation retrieval output at snow layer height 400 m in dash-dotted green; and ensemble member deterministic forecast, initialised at 0 UTC in black and its nine perturbed ensemble members in grey. The ensemble mean of all ten members is shown in dashed blue. Underneath are the associated last 10 min average wind from the weather mast at 10 m height.

estimated surface precipitation amount for all ten ensemble members than observed at the measurement site between 24 December 2016 to 26 December 2016.

The correlation between double fence observation and ensemble forecast is presented in Figure 4.2.3a and b. Showing a better agreement between 21 December 2016 to 23 December 2016 than initialisation on 24 December 2016 to 26 December 2016. On 21 December 2016 to 23 December 2016 is the slope of the regression relatively close to unity, indicating a good agreement between the ensemble forecast and the observations by the double fence. The largest disagreement between surface observations and forecasts is seen on 25 December 2016 with a positive bias up to 17 mm (Figure C.2.1i). The mean absolute error is not larger than 13 mm for the first three days and increases with intensification of the storm up to 19 mm on 24 December 2016.

Initialisations on 24 December 2016 indicate an overestimation of the deterministic surface snowfall prediction already after 13 h forecast time. The deterministic forecast in solid black is much higher and increases faster than the observations. In Figure 4.3.1d at 16 UTC a higher value of approximately 15 mm can be seen when compared to the surface measurements. This difference remains almost constantly over the forecast time. Furthermore, all ensemble members seem to overestimate the surface accumulation after 24 h prediction time.

Since the MEPS performance was better on the previous days one might assume that the double fence measurement is influenced by surface winds. It shows in Figure 4.3.1d that the 10 min average wind at 13 UTC increases from 5 m s^{-1} to 10 m s^{-1} (see also ??). Wolff [2018] states that the double fence gauge is influenced by wind, but accumulation measurement errors occur rather at higher wind speeds larger than 20 m s^{-1} . It is therefore assumed that the measurements from the double fence are correct and MEPS had rather a forecasting issue.

While the cyclone gets more advected to Norway increases the forecast inaccuracy of the surface precipitation. On 25 December 2016 the miscalculation of the precipitation amount is associated with the warm sector passage at Haukeliseter (Section 4.2). Afterwards follows the model the same path as the double fence observations, but higher. The 25 December 2016 indicates a good spread between the ensemble members and the deterministic forecast, while on 24 December 2016 the ensemble members were not spread symmetrically around the deterministic forecast.

An overestimation of the surface accumulation is also observed on 26 December 2016. While the large-scale analysis indicates the passage of an occlusion after 15 UTC (Fig-

ure 3.2.1g, g) seems the overestimation to occur after 12 h forecast time in Figure 4.3.1f. Again, all ensemble members seem to follow the course of the double fence accumulation, but larger.

Whereas the spread between the ensemble members is large in the beginning of 24 December 2016 is the variability between the members narrow for 25 December 2016 and 26 December 2016.

The variability between the ensemble member can be compared with a box-whisker plot. A box-whisker-plot shows the time evolution of the distribution of the precipitation amount made of ten ensemble members up to 48 h. Since some ensemble member do not have forecast values every hour provides the box-whisker-plot in Figure 4.3.2 information every 3 h. The red line shows the ensemble mean of all ten members. The short light green horizontal line is showing the median, wide vertical box represents the 25th and 75th percentiles, and minimum and maximum values are indicated by the vertical lines.

The box-whisker-plot in Figure 4.3.2 shows the distribution of the ten ensemble members for the respective days. All three days with overestimation seem to be different in their variability. As expected increases the forecast uncertainty with longer forecast time for precipitation amount.

Figure 4.3.2b shows for 25 December 2016 the least variability between the ten ensemble members of up to almost 24 h. The 25 December 2016 is also the forecast with the smallest positive bias of these three days. As Figure 4.2.3j suggests is the overestimation not as high as for 24 December 2016 and 25 December 2016. On 24 December 2016 and 26 December 2016 is the mean error for the surface accumulation largest with values up to 19 mm.

Larger variability is already present after 3 h prediction time in Figure 4.3.2a on 24 December 2016. The spread between the ensemble members (shown by the minimum and maximum whiskers) seems to be wide indicating a larger uncertainty about the amount of surface accumulation. The ensemble mean (red line) is always higher than the median and already after 12 h forecast time is the median closer to the lower 25th percentile. Also, all upper whiskers in Figure 4.3.2a are taller than the lower ones, which would follow that the ensemble members vary amongst the most positive quartile and that it is very similar for the least positive quartile group. Since the deterministic forecast, black line in Figure 4.3.1d, is in the upper percentile compared to its perturbed members it follows that for this forecast the deterministic forecast was not the best guess for the surface accumulation and by

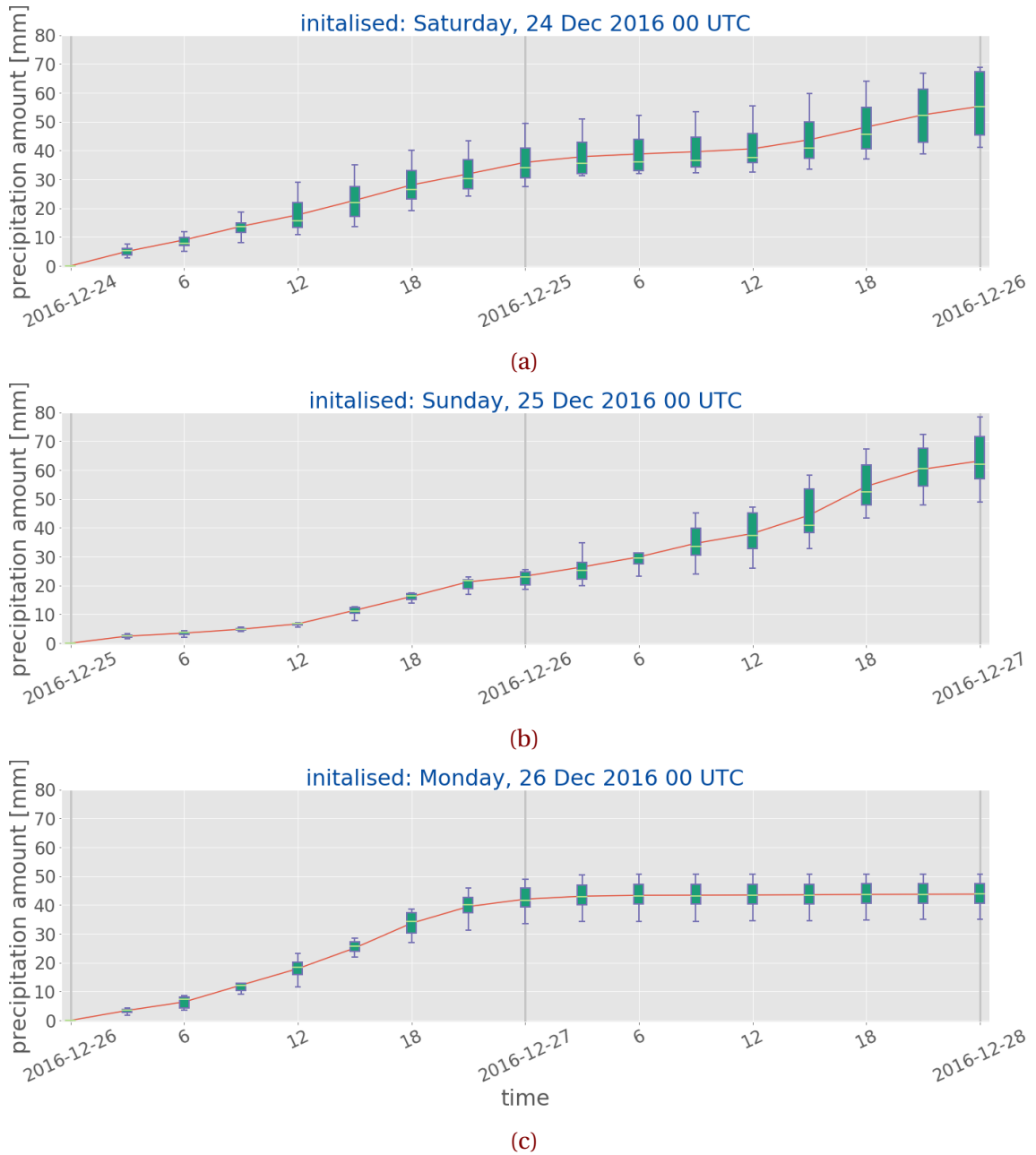


Figure 4.3.2: Box-whisker-plot of the ten ensemble members of MEPS. Red line indicating the ensemble mean, lower and upper whisker the 25th and 75th percentile, respectively. Light green shows the median of all members and the box represents the middle 50 % of scores of the precipitation.

using the 'wrong' initial state it can have led to larger miscalculations. I believe that the uncertainty appearing already after 3 h could be associated with a too long spin-up time of MEPS. MEPS usually has a spin-up time of about three hours, on 24 December 2016 this might have been longer as a result of poorer initial conditions [Need a reference here, not stated in Müller et al. \[2017\]](#). The regional model MEPS receives initial and boundary conditions from ECMWF before it can produce forecasts [Müller et al. \[2017\]](#). Since initial conditions such as observations have uncertainties as well as the model has mistrust, and needs to approach its own climatology, a model has to stabilize before the simulations can be trusted. The spin-up time varies depending on the quality of the initial and boundary conditions. Apparently, it seems, that the initial and boundary conditions for MEPS were not perfect for initialisations on 24 December 2016 at 0 UTC. The deterministic and perturbed members seem not to have stabilised yet and show larger variability in ?? from early on.

The uncertainty might have also been related to the fact, that the large-scale situation got more complex. The precipitation amount associated with the passage of an occluded front on 23 December 2016 was higher than on the previous days (Figure 4.2.1i and Figure 3.5.1). On previous days was the hourly precipitation around 0 UTC less intense than on 23 December 2016. This led to a higher accumulation amount over shorter time and could have led to a larger variability in the forecast model. Another possibility is perhaps that MEPS might have accounted for additional precipitation around 12 UTC on 24 December 2016 and this showed a stronger increase in accretion in Figure 4.3.1d at 13 UTC. I believe it could be associated to a local resolution effect of MEPS. Figure 2.5.1 shows the MEPS resolution and its 2.5 km grid cells around the Haukeliseter site. The complex terrain in the model could have followed a local misplacement of a precipitation cell by a few kilometres and followed an estimation of more accumulation at the site after noon.

In Figure 4.3.2b and c shows a smaller ensemble member variability on 25 December 2016 and 26 December 2016 than on 24 December 2016. The box-whiskers are narrower for the first 30 h in Figure 4.3.2b, but slightly larger after 6 h forecast time for initialisations on 26 December 2016. Section 4.2 presented a good agreement between observations and forecast of large scale features. While the occlusion on 26 December 2016 was more intuitive (Figures 4.2.1k to 4.2.1n) than the warm front passage on 25 December 2016 (Figure 4.2.1b, d, f, h) shows the mean error for each variable to be best for 25 December 2016

(Figure C.2.1b,d,f, h, and j).

On 25 December 2016 the overestimation started to occur around 13 UTC in Figure 4.3.1e, related to the delayed forecasted temperature increase in Figure 4.2.1d. As ?? shows, increases the variability in the forecast after 15 h prediction time. In general, agree median and mean well for the entire period of a 48 h forecast. After 39 h prediction time is the mean much higher than the median and closer to the lower 25th percentile in ?? It seems, that all ten ensemble members agree well on the prediction and nevertheless overestimates MEPS the surface accumulation. I consider that MEPS misinterpreted the amount of precipitation related to the passage of the warm sector.

During 26 December 2016 the core of the low-pressure system goes through between 15 UTC and 18 UTC at Haukeliseter. The box-whiskers in Figure 4.3.2c indicates a larger variability after 6 h prediction while the precipitation amount forecast is miscalculated at 12 UTC and following the structure of the double fence observation. Variability of all ensemble members show to increase at 6 h forecast time, but then decreases again in Figure 4.3.2c.

Since the box-whisker-plot in Figure 4.3.2b and c show less variability in the beginning it is assumed that spin-up time issues are less likely. It could be related to an error in the initialisation state, even though it does not show in the variability in the beginning. An error associated with the spin-up time of MEPS is not totally excluded for these days. In Figure 4.3.1e and f agrees the ensemble mean well with the deterministic forecast, which is an indication of a symmetrical spread around the deterministic run.

The overestimation during 24 December 2016 and 26 December 2016 might be related to the high forecasted wind speeds, as well as to the complex development of the low-pressure system north-west of Norway on 24 December 2016.

According to Müller et al. [2017] are strong precipitation events better predicted with AROME-MetCoOp than with ECMWF (European Centre for Medium-Range Weather Forecasts). In Section 2.2 it was described, that during 21 December 2016 to 27 December 2016 56.9 % of the total December 2016 accumulation were observed. Müller et al. [2017] states also, that an overestimation appears, where the precipitation event (12 h accumulation) is less than 10 mm this seems not to be true for all days but could be possible for 25 December 2016 and 26 December 2016 (observed accumulation in Table 4.3.1). In December 2014 was the 12 h precipitation mean absolute error in AROME-MetCoOp

Table 4.3.1: Surface snowfall accumulation measured by the double fence gauge. Presenting 12 h accumulation before noon and after noon, as well as the total 24 h surface accretion.

Day	Accumulation		
	[mm]		
	12 h (0 to 12 UTC)	12 h (12 to 23 UTC)	24 h
21 December 2016	0.7	16.4	17.1
22 December 2016	13.6	12.0	25.6
23 December 2016	6.3	17.0	23.3
24 December 2016	14.7	10.1	24.8
25 December 2016	4.3	11.1	15.4
26 December 2016	8.8	16.3	25.1

1.5 mm. For the Christmas storm is the mean absolute error not larger than 5 mm for the first 12 h accumulation on 24 December 2016 and 26 December 2016 (Figure C.2.11). Therefore, the assumption follows that on 26 December 2016 the overestimation might be correlated to the <10 mm problem described by Müller et al. [2017]. On 25 December 2016 the mean absolute error was 1.1 mm for the first 12 h accumulation and shows that this could be an influence but does not necessarily mean to be the case, since the overestimation started occurring after 11 h prediction time.

It will be interesting to re-run the ensemble prediction system again with all available observations to see, if this has an influence on the overestimation indicated in Figures 4.3.1d to 4.3.1f. ECMWF as boundary condition might not have reached its stabilised state when MEPS was initiated and could also have led to a misinterpretation. A re-run with analysis data from ECMWF could possibly improve the original forecast [find reference for this](#). Another approach could be to perturb the initial state (deterministic forecast) in other way, to see if different perturbations might lead to a better correlation between observation and forecast at the ground. Also, the deterministic forecast (best guess) might have been chosen incorrectly and followed a miscalculation of surface accumulation. It is very important to have correct measurements such as the double fence or MRR observations,

to produce better initial condition for weather forecast models, so that initialisations can start at a realistic state.

Also, more study cases should be considered to get a better estimate about the performance of MEPS during extreme winter events. The mean absolute error for 12 h accumulation has shown a great variability, depending on the initialisation time and the intensification of the low-pressure system.

4.4 OBSERVATION OF LARGE SCALE WEATHER PHENOMENA IN THE VERTICAL

Frontal boundary passages were observed at the surface several times throughout the extreme storm in December 2016. MEPS is able to predict the large scale features for initialisation more than 24 h before (Section 4.2). In winter 2016 three additional instruments were installed to estimate the vertical snow water content at Haukeliseter. This unique approach gives the unique opportunity to compare the vertical forecasts of SWC to vertical solid precipitation observations. As far as the author knows is there no study on this particular topic about the verification of vertical ensemble member prediction models with observations.

Figure 4.4.1 shows the reflectivity from the MRR at Haukeliseter for 23 December 2016, 25 December 2016 and 26 December 2016. Passages of occluded fronts and a warm sector were observed on 23 December 2016, 26 December 2016 and 25 December 2016, respectively. Figure 4.4.1c presents only values until 17 UTC, because of the temperature change and hence a precipitation shift followed liquid drops freezing on the MRR dish and the signal got attenuated. The transit of the boundaries is shown in Figure 4.4.1 by the more consistent structure of a storm with higher reflectivity values. While on 23 December 2016 and 25 December 2016 the reflectivity did not pass values larger than 28 dBZ shows Figure 4.4.1b high reflectivity values larger than 30 dBZ (compare for approximation Table 2.3.1). These high values indicate the observation of possible liquid precipitation. Images from the MASC were able to verify observed liquid drops (Figure 4.2.2). On 23 December 2016 allow the surface observations to assume that the occluded front passed through between 12 UTC to 21 UTC (Figure 4.2.1a, c, e). The vertical observations at Haukeliseter show intense reflectivity and therefore more intense precipitation after

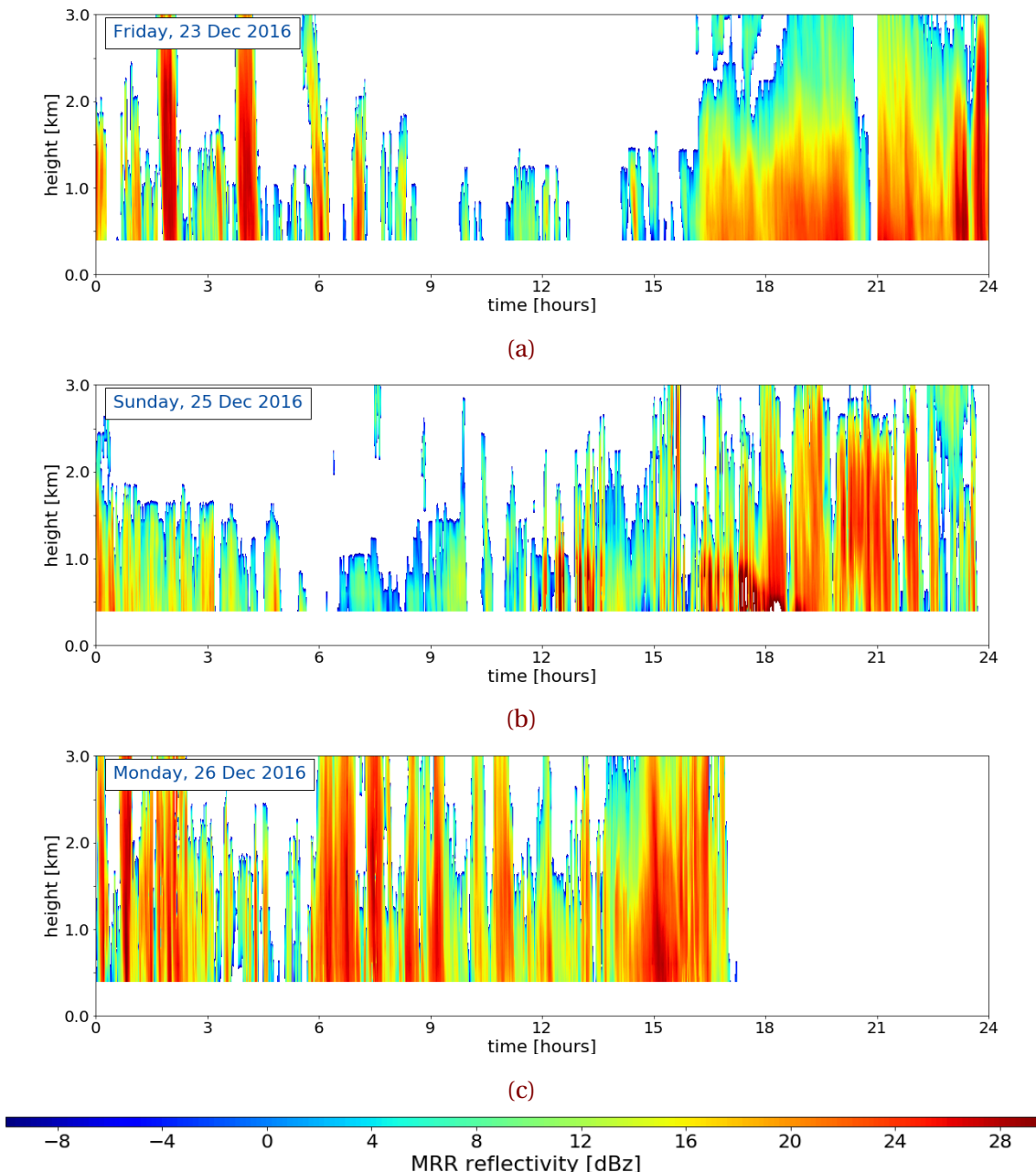


Figure 4.4.1: MRR reflectivity for the days when a front or an occlusion passed through at Haukeliseter. dBZ reflectivity according to the colour bar, with weaker precipitation in blue and more intense precipitation in red. **a:** Friday, 23 December 2016, **b:** Sunday, 25 December 2016, and **c:** Monday, 26 December 2016.

16 UTC. Another occlusion passed through on 26 December 2016 shortly before 15 UTC which lasted until 21 UTC. The high reflectivity on both days shows the passage of the fronts and the associated precipitation. The wind on 23 December 2016 was from the south, upslope (Figure 4.2.1e, Figure 2.1.1c) which led to a more consistent storm structure. On 25 December 2016 indicate Figure 4.2.1f and h strong wind observations from the west which led a consistent, but shorter storm structure in Figure 4.4.1b. The orographic influenced wind and therefore a relation to the precipitation will be further assessed in Section 4.5.

Figure 4.4.2b (lower panel) shows the one hourly averaged values over all ensemble members, neglecting not existing values. The forecast predicts the consistent storm pattern after 16 UTC, when initialised less than 24 h before. Even the three hourly averaged forecast values show a response on the occurrence of the storm (Figure 4.4.2c, lower panel). That the 3 h averages predicts the snow water content is related to the duration of the occlusion passage (between 16 UTC to 23 UTC). In general, is the forecasted instantaneous snow water content amount weaker than the retrieved values on 23 December 2016. Hourly averages, only using the deterministic forecast and the first ensemble member show no occurrence of the occlusion passage on either day (Figure C.3.1a, b, c). The variation of each ensemble member initialised on the respective day are given in Figure C.4.1. It shows that on 23 December 2016 the first perturbed ensemble member does not exist and hence little snow water content is predicted for the ensemble means. A comparison with 25 December 2016 and 26 December 2016 shows the same result. Not much more snow water content is predicted when using the instantaneous values from the deterministic and first perturbed forecast (Figure C.3.1b, c).

On 26 December 2016 when the passage of the occlusion is predicted, the three-hourly instantaneous SWC (Figure 4.4.2i) as well as the average of all ensemble members (Figure 4.4.2h) predict the frontal passage. Already initialisations 39 h prior let assume that intense precipitation over a short time will occur. The variation of all members in Figure C.4.1b and c indicate that almost all perturbed members would have predicted the precipitation around 16 UTC. The deterministic forecast shows in both cases the highest SWC values when comparing to the perturbed members. But in Figure C.3.1b and c is the amount of snow water content very weak. It shows better estimations for predicted snowfall amount when using either hourly or three hourly time resolution and all ten ensemble members to create the mean than forecasts for hourly averages with only the

deterministic and first perturbed member. Still the instantaneous average values of all ensemble members are much weaker than the retrieved SWC.

Higher predicted values appear for deterministic forecasts than for any other ensemble member for initialisations on 25 December 2016 and 26 December 2016. This bias might have led to an overestimation at the surface on 26 December 2016, where the deterministic forecast indicates higher values than the perturbed members (Figure 4.3.1f).

The 25 December 2016 showed patterns of liquid precipitation (Figure 4.2.2) with warm temperatures (Figure 4.2.1d) and high reflectivity (Figure 4.4.1b) between 12 UTC to 21 UTC. To see if liquid precipitation was forecasted, the atmospheric cloud condensed water content and rainfall amount in model levels is summed. Figure 4.4.3a and b show liquid water content for initialisations at either 24 December 2016 or 25 December 2016. Positive surface temperatures were forecasted between 12 UTC to 21 UTC (Figure 4.2.1d). Since MEPS forecasts the liquid layer correctly in depth and length it seems to be a good interaction between the surface model setting the vertical prediction. High reflectivity values in Figure 4.4.1b are present around 18 UTC with layer thickness up to 1.2 km. Figure 4.4.3a or b show also a narrow thickness up to 800 m.

A validation of how well the forecast performed is difficult to do at this state, since the time resolution of MEPS is coarse compared to the observations. For the first glance operates the forecast well when compared to vertical observations. One possibility to assess the variability of all ensemble member. ?????? show the coefficient of variation for SWC, which is the standard deviation of the ten ensemble members divided by the mean of all ensemble members. This coefficient gives the possibility to compare the SWC results for different days with different values. It also shows if the ensemble spread (standard deviation of all ensemble members) is low the SWC is does not need to be less variable. One question to answer in this work is if the operational model MEPS gets large scale features correctly. As discussed here and in Section 4.2 it seems that the model is able to cover the development of large scale features and its associated precipitation. Even with the intensification of the storm seems MEPS to be able to predict extreme events such as the Christmas event. MEPS is also able to distinguish between liquid and solid precipitation in layer thickness and duration. This can be major approach since a change in temperature and associated precipitation transformation can lead to major risks in the Norwegian mountains, especially during winter. With the knowledge more than 24 h prior risk notice can be send out to the population and rescue teams can prepare better.

Furthermore, roads and train tracks can be closed to increase the safety of people.

I'm not sure if the above mentioned should be here?!

4.5 OROGRAPHIC INFLUENCE ON PRECIPITATION

It has shown, that wind plays an important role at the Haukeliseter measurement site, since it is suspended to high wind speeds during the winter. The mountain plateau is surrounded by higher mountains to the west and more open to the south east [[Wolff et al., 2013, 2015](#)]). The correlation between wind speed observations and forecast have shown an overestimation throughout the event (Figure [4.2.3g](#) and [h](#)). It seems, that wind direction plays an important role too, at the Haukeliseter site.

During 24 December 2016 to 26 December 2016 was the wind constantly from the west with higher wind speeds observed than during 21 December 2016 to 23 December 2016 (Figure [4.2.1e, f, m](#); Figure [C.1.1e, f, m](#); Figure [4.2.1g, h, n](#), and Figure [C.1.1g, h, n](#)). Figure [4.2.3e](#) and [f](#) indicate a better agreement between the forecasted and observed wind directions when precipitation overestimation occurred. During 24 December 2016 to 26 December 2016 were the observed wind speeds higher than on the previous days, and as Figure [4.2.3g](#) and [h](#) present is the correlation between observation and forecasts lower during high wind speeds.

While the wind direction of MEPS has a good agreement shows the wind speed larger values over all days. Although MEPS includes ten perturbed ensemble members the insufficiency of AROME-MetCoOp too high wind prediction in extreme situations is not resolved. The regional model wind prediction is still dependent on the intensity of the storm. As [Müller et al. \[2017\]](#) also mentioned are higher wind speeds in general better forecasted in AROME-MetCoOp than in ECMWF.

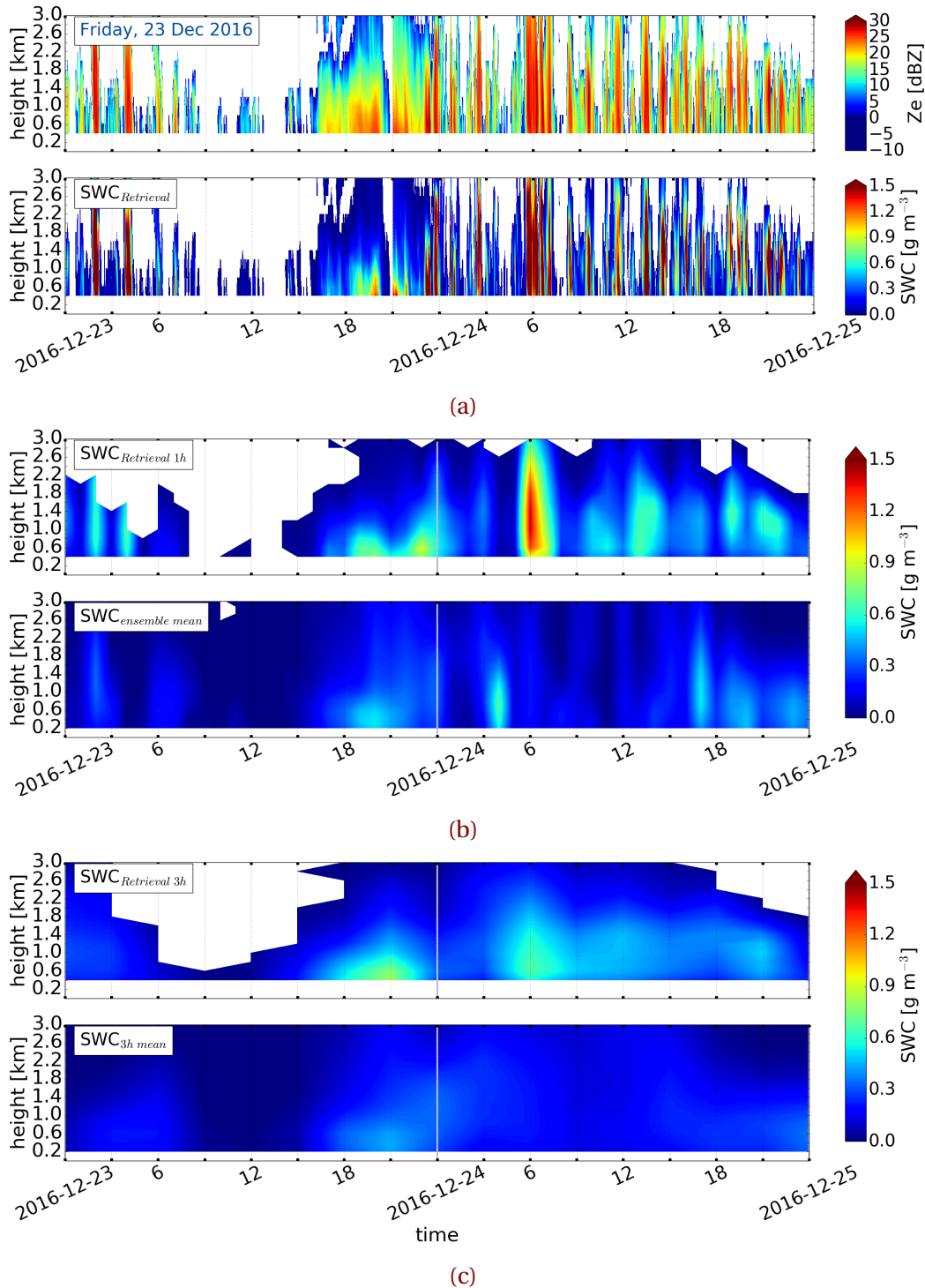


Figure 4.4.2: Initialisation 23 December 2016, 25 December 2016 and 26 December 2016 0 UTC. (a, d, g) Upper panel: MRR reflectivity for 48 h, lower panel minutely retrieved SWC. (b, e, h) Upper panel: hourly averaged retrieved SWC, lower panel instantaneous hourly averaged forecast of all ensemble member SWC, neglecting missing values. (c, f, i) Upper panel three hourly averaged retrieved SWC, lower panel instantaneous three hourly averaged forecast of all ensemble member SWC.

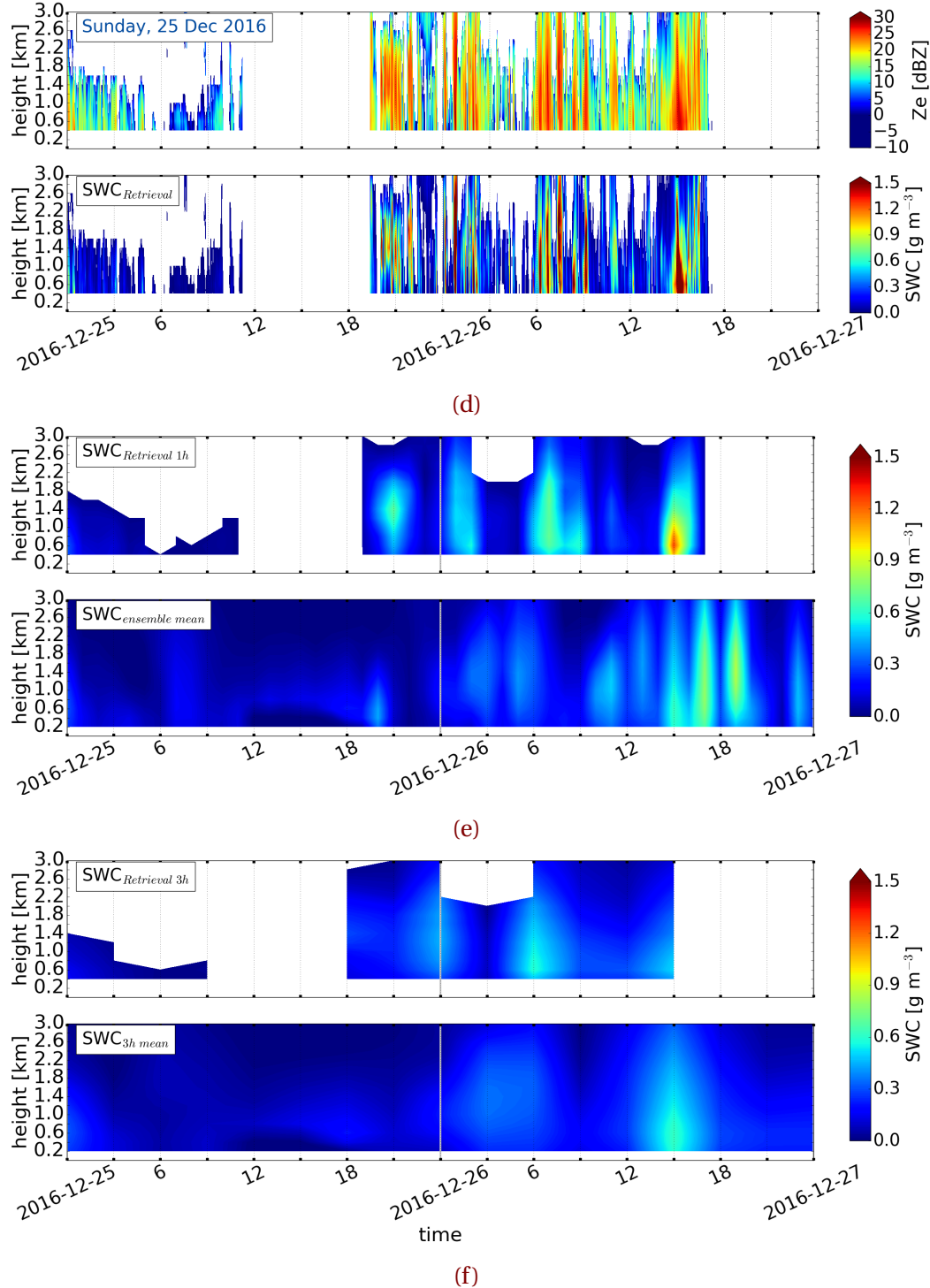


Figure 4.4.2: (Continued from previous page.) Initialisation 25 December 2016.

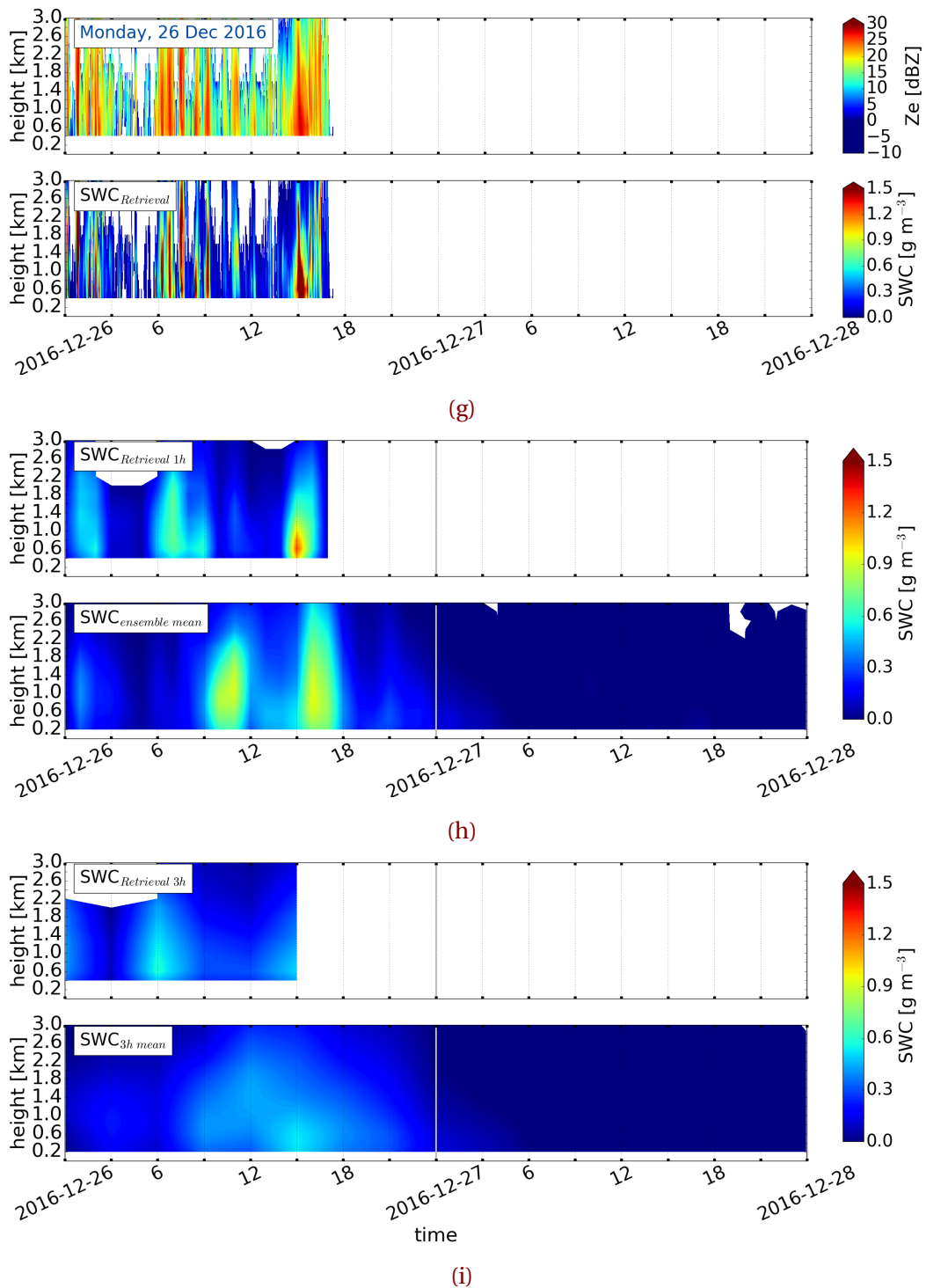


Figure 4.4.2: (Continued from previous page.) Initialisation 26 December 2016.

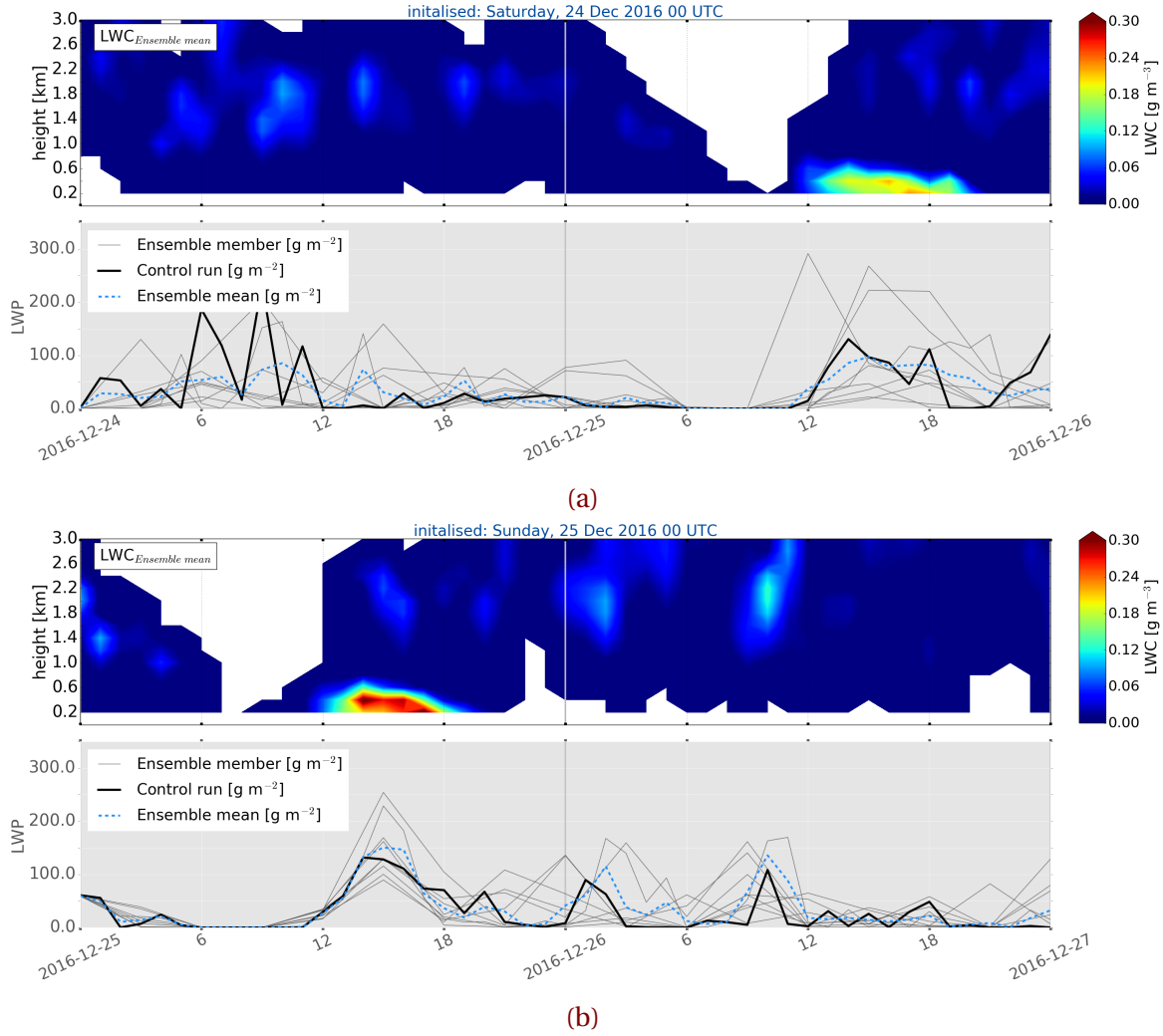


Figure 4.4.3: Upper panel: 200m hourly averaged LWC forecast from MEPS with all ensemble members, neglecting missing values. Lower panel: LWP from MEPS, initialised at 0 UTC. Black line represents the deterministic forecast, the dotted blue line the ensemble mean and the grey lines the nine perturbed members.

CHAPTER 5: SUMMARY AND CONCLUSION

SUMMARIZE! What did you do? Why did you do it? What did you use? What were your findings? What could be done in the future?

REFERENCES

- Caniaux, G., Redelsperger, J.-L., and Lafore, J.-P. A Numerical Study of the Stratiform Region of a Fast-Moving Squall Line. Part I: General Description and Water and Heat Budgets. *J. Atmos. Sci.*, 51(14):2046–2074, July 1994. ISSN 0022-4928. doi: [10.1175/1520-0469\(1994\)051<2046:ANSOTS>2.0.CO;2](https://doi.org/10.1175/1520-0469(1994)051<2046:ANSOTS>2.0.CO;2). URL [https://journals.ametsoc.org/doi/abs/10.1175/1520-0469\(1994\)051%3C2046:ANSOTS%3E2.0.CO;2](https://journals.ametsoc.org/doi/abs/10.1175/1520-0469(1994)051%3C2046:ANSOTS%3E2.0.CO;2).
- Cooper, S. J., Wood, N. B., and L'Ecuyer, T. S. A variational technique to estimate snowfall rate from coincident radar, snowflake, and fall-speed observations. *Atmos. Meas. Tech.*, 10(7):2557–2571, July 2017. ISSN 1867-8548. doi: [10.5194/amt-10-2557-2017](https://doi.org/10.5194/amt-10-2557-2017). URL <https://www.atmos-meas-tech.net/10/2557/2017/>.
- Dahlgren, P. A Comparison Of Two Large Scale Blending Methods. page 16, 2013. URL <http://metcoop.org/memo/2013/02-2013-METCOOP-MEMO.PDF>.
- Dando, P. Introducing the octahedral reduced Gaussian grid, June 2016. URL <https://software.ecmwf.int/wiki/display/FCST/Gaussian+grids>.
- Doviak, R. J. and Zrnic, D. S. *Doppler Radar and Weather Observations*. Courier Corporation, 1993. ISBN 978-0-486-45060-5. Google-Books-ID: [ispLkPX9n2UC](#).
- eklima. Norwegian Meteorological Institute, 2016. URL http://sharki.oslo.dnmi.no/portal/page?_pageid=73,39035,73_39049&_dad=portal&_schema=PORTAL.
- Farestveit, E. 80.000 mista radioen under ekstremvêret, December 2016. URL <https://www.nrk.no/hordaland/80.000-mista-radioen-under-ekstremveret-1.13294980>.

- Færaas, A., Rommetveit, A., Duesund, J., and Senel, E. «Urd» har nådd orkan styrke – flytter seg mot Østlandet, December 2016. URL http://www.yr.no/artikkelen/_urd_-har-nadd-orkan-styrke_-_flytter-seg-mot-ostlandet-1.13292245.
- Garrett, T. J., Fallgatter, C., Shkurko, K., and Howlett, D. Fall speed measurement and high-resolution multi-angle photography of hydrometeors in free fall. *Atmos. Meas. Tech.*, 5(11):2625–2633, November 2012. ISSN 1867-8548. doi: [10.5194/amt-5-2625-2012](https://doi.org/10.5194/amt-5-2625-2012). URL <https://www.atmos-meas-tech.net/5/2625/2012/>.
- Geonor Inc. T-200b All Weather Precipitation – Rain Gauge, 2015. URL <http://geonor.com/live/products/weather-instruments/t-200b-weather-precipitation-rain-gauge/>.
- Geonorge. DTM 10 Terrengmodell (UTM33) - Kartverket - Kartkatalogen, May 2018. URL <https://kartkatalog.geonorge.no/metadata/uuid/dddbb667-1303-4ac5-8640-7ec04c0e3918>.
- Gunn, K. L. S. and East, T. W. R. The microwave properties of precipitation particles. *Q. J. Royal Meteorol. Soc.*, 80(346):522–545, 1954.
- Homleid, M. and Tveter, F. T. Verification of operational weather prediction models september to november 2015. *METInfo Rep*, 16:2016, 2016. URL https://www.met.no/publikasjoner/met-info/met-info-2016/_attachment/download/b0463915-cba0-42ac-8539-4233ae2bf01c:3d71565a27f88085373199a33ab8569151c144e9/MET-info-22-2016.pdf.
- Hoskins, B. J., McIntyre, M. E., and Robertson, A. W. On the use and significance of isentropic potential vorticity maps. *Q. J. Royal Meteorol. Soc.*, 111(470):877–946, October 1985. ISSN 1477-870X. doi: [10.1002/qj.49711147002](https://doi.org/10.1002/qj.49711147002). URL <http://onlinelibrary.wiley.com/doi/10.1002/qj.49711147002/abstract>.
- Hudak, D., Barker, H., Rodriguez, P., and Donovan, D. The Canadian CloudSat Validation Project. *4th ERAD*, September 2006. URL <http://www.crahi.upc.edu/ERAD2006/proceedingsMask/00165.pdf>. Barcelona, Spain.
- Kulie, M. S. and Bennartz, R. Utilizing Spaceborne Radars to Retrieve Dry Snowfall. *J. Appl. Meteor. Climatol.*, 48(12):2564–2580, January 2009. ISSN 1558-8424. doi: [10.1175/2008JAMC2124.1](https://doi.org/10.1175/2008JAMC2124.1).

- 10.1175/2009JAMC2193.1. URL <http://journals.ametsoc.org/doi/abs/10.1175/2009JAMC2193.1>.
- Køltzow, M. A. MetCoOp EPS - A convection permitting ensemble prediction system, October 2017.
- Lamb, D. and Verlinde, J. *Physics and Chemistry of Clouds*. Cambridge University Press, April 2011. ISBN 978-1-139-50094-4. Google-Books-ID: H97QKhe16aUC.
- L'Ecuyer, T. S. AOS 441 - Satellite and Radar Meteorology. January 2017. URL <https://lecuyer.aos.wisc.edu/aos441>.
- L'Ecuyer, T. S. and Stephens, G. L. An Estimation-Based Precipitation Retrieval Algorithm for Attenuating Radars. *J. Appl. Meteor.*, 41(3):272–285, January 2002. ISSN 0894-8763. doi: 10.1175/1520-0450(2002)041<0272:AEBPRA>2.0.CO;2. URL [http://journals.ametsoc.org/doi/abs/10.1175/1520-0450\(2002\)041%3C0272:AEBPRA%3E2.0.CO%3B2](http://journals.ametsoc.org/doi/abs/10.1175/1520-0450(2002)041%3C0272:AEBPRA%3E2.0.CO%3B2).
- Liu G. Deriving snow cloud characteristics from CloudSat observations. *J. Geophys. Res. Atmos.*, 113(D8), September 2008. ISSN 0148-0227. doi: 10.1029/2007JD009766. URL <https://agupubs.onlinelibrary.wiley.com/doi/abs/10.1029/2007JD009766>.
- Lohmann, U., Lüönd, F., and Mahrt, F. *An Introduction to Clouds: From the Microscale to Climate*. Cambridge University Press, June 2016. ISBN 978-1-107-01822-8. Google-Books-ID: KR1CDAAAQBAJ.
- Markowski, P. and Richardson, Y. *Mesoscale Meteorology in Midlatitudes*. John Wiley & Sons, September 2011. ISBN 978-1-119-96667-8. Google-Books-ID: MDeYosfLLEYC.
- Martin, J. E. *Mid-Latitude Atmospheric Dynamics: A First Course*. Wiley, May 2006. ISBN 978-0-470-86466-1.
- McCumber, M., Tao, W.-K., Simpson, J., Penc, R., and Soong, S.-T. Comparison of Ice-Phase Microphysical Parameterization Schemes Using Numerical Simulations of Tropical Convection. *J. Appl. Meteor.*, 30(7):985–1004, July 1991. ISSN 0894-8763. doi: 10.1175/1520-0450-30.7.985. URL <https://journals.ametsoc.org/doi/abs/10.1175/1520-0450-30.7.985>.

- MetCoOp Wiki. Description of MEPS, December 2017. URL <https://metcoop.smhi.se/dokuwiki/nwp/metcoop/>.
- METEK, M. M. G. Micro Rain Radar MRR-2, October 2010. URL <http://metek.de/wp-content/uploads/2014/05/Metek-Micro-Rain-Radar-MRR-2-Datasheet.pdf>.
- Meteo France. The Meso-NH Atmospheric Simulation System: Scientific Documentation, Part III: Physics, January 2009.
- Meteorologene. "Her kommer #Urd! Selve Lavtrykksenteret treffer Møre og Romsdal, men den sterkeste vinden kommer sør for Stad. #SørNorge" 26 December 2016, 9:34am, 2016. URL <https://twitter.com/Meteorologene>.
- Müller, M., Homleid, M., Ivarsson, K.-I., Køltzow, M. A. Ø., Lindskog, M., Midtbø, K. H., Andrae, U., Aspelien, T., Berggren, L., Bjørge, D., Dahlgren, P., Kristiansen, J., Randriamampianina, R., Ridal, M., and Vignes, O. AROME-MetCoOp: A Nordic Convective-Scale Operational Weather Prediction Model. *Wea. Forecasting*, 32(2):609–627, January 2017. ISSN 0882-8156. doi: [10.1175/WAF-D-16-0099.1](https://doi.org/10.1175/WAF-D-16-0099.1). URL <http://journals.ametsoc.org/doi/abs/10.1175/WAF-D-16-0099.1>.
- Newman, A. J., Kucera, P. A., and Bliven, L. F. Presenting the Snowflake Video Imager (SVI). *J. Atmos. Oceanic Technol.*, 26(2):167–179, February 2009. ISSN 0739-0572. doi: [10.1175/2008JTECHA1148.1](https://doi.org/10.1175/2008JTECHA1148.1). URL <https://journals.ametsoc.org/doi/abs/10.1175/2008JTECHA1148.1>.
- Norin, L., Devasthale, A., L'Ecuyer, T. S., Wood, N. B., and Smalley, M. Intercomparison of snowfall estimates derived from the CloudSat Cloud Profiling Radar and the ground-based weather radar network over Sweden. *Atmos. Meas. Tech.*, 8(12):5009–5021, December 2015. ISSN 1867-8548. doi: [10.5194/amt-8-5009-2015](https://doi.org/10.5194/amt-8-5009-2015). URL <https://www.atmos-meas-tech.net/8/5009/2015/>.
- Norwegian Meteorological Institute. MET Norway Thredds Service, 2016. URL <http://thredds.met.no/thredds/catalog/meps25epsarchive/catalog.html>.
- Olsen, A.-M. and Granerød, M. Ekstremværrapport. Hendelse: Urd 26. desember met. info. no. 18/2017 ISSN X METEOROLOGI Bergen, - PDF, September

2017. URL <http://docplayer.me/48734203-Ekstremvaerrapport-hendelse-urd-26-desember-met-info-no-18-2017-issn-x-meteorologi-bergen.html>.
- Pedersen, K. and Rommetveit, A. Hva er et «ekstremvær»?, November 2013. URL http://www.yr.no/artikkeli/hva-er-et-_ekstremvaer___1.7890946.
- Peel, M. C., Finlayson, B. L., and McMahon, T. A. Updated world map of the Köppen-Geiger climate classification. *Hydrology and Earth System Sciences Discussions*, 4(2):439–473, March 2007. URL <https://hal.archives-ouvertes.fr/hal-00298818>.
- Pinty, J.-P. and Jabouille, P. A mixed-phased cloud parameterization for use in a mesoscale non-hydrostatic model: Simulations of a squall line and of orographic precipitation. pages 217–220. Amer. Meteor. Soc., 1998.
- Rinehart, R. E. *Radar for Meteorologists: Or You, Too, Can be a Radar Meteorologist*. Rinehart Publications, 2010. ISBN 978-0-9658002-3-5. Google-Books-ID: VqatcQAACAAJ.
- Rodgers, C. D. *Inverse Methods for Atmospheric Sounding: Theory and Practice*. World Scientific, 2000. ISBN 978-981-02-2740-1. Google-Books-ID: FjxqDQAAQBAJ.
- Rutz, J. J., Steenburgh, W. J., and Ralph, F. M. Climatological Characteristics of Atmospheric Rivers and Their Inland Penetration over the Western United States. *Mon. Wea. Rev.*, 142(2):905–921, January 2014. ISSN 0027-0644. doi: [10.1175/MWR-D-13-00168.1](https://doi.org/10.1175/MWR-D-13-00168.1). URL <http://journals.ametsoc.org/doi/abs/10.1175/MWR-D-13-00168.1>.
- Ruud, S., Carr Ekroll, H., Bakke Foss, A., Torgersen, H. O., and Annar Holm, P. To tonn tungt skilt blåste ned da ekstremværet traff Oslo og Østlandet i natt, December 2016. URL <https://www.aftenposten.no/article/ap-2z6wy.html>.
- Stephens, G. L. *Remote Sensing of the Lower Atmosphere: An Introduction*. Oxford University Press, 1994. ISBN 978-0-19-508188-6. Google-Books-ID: 2FcRAQAAIAAJ.
- Stephens, G. L. and Wood, N. B. Properties of Tropical Convection Observed by Millimeter-Wave Radar Systems. *Monthly Weather Review*, 135(3):821–842, March 2007. ISSN 0027-0644, 1520-0493. doi: [10.1175/MWR3321.1](https://doi.org/10.1175/MWR3321.1). URL <http://journals.ametsoc.org/doi/abs/10.1175/MWR3321.1>.

- University Wyoming. Atmospheric Soundings, January 2018. URL <http://weather.uwyo.edu/upperair/sounding.html>.
- Wolff, M. A. WMO Solid Precipitation Intercomparison Experiment (WMO-SPICE), Ch. 4.2.4 Precipitation measurements in areas with high winds and/or complex terrain. unpublished, 2018.
- Wolff, M. A., Brækkan, R., Isaksen, K., and Ruud, E. A new testsite for wind correction of precipitation measurements at a mountain plateau in southern Norway. In *Proceedings of WMO Technical Conference on Meteorological and Environmental Instruments and Methods of Observation (TECO–2010). Instruments and Observing Methods Report*, 2010.
- Wolff, M. A., Isaksen, K., Brækkan, R., Alfnes, E., Petersen-Øverleir, A., and Ruud, E. Measurements of wind-induced loss of solid precipitation: description of a Norwegian field study. *Hydrol. Res.*, 44(1):35–43, February 2013. ISSN 0029-1277, 2224-7955. doi: [10.2166/nh.2012.166](https://doi.org/10.2166/nh.2012.166). URL <http://hr.iwaponline.com/content/44/1/35>.
- Wolff, M. A., Isaksen, K., Petersen-Øverleir, A., Ødemark, K., Reitan, T., and Brækkan, R. Derivation of a new continuous adjustment function for correcting wind-induced loss of solid precipitation: results of a Norwegian field study. *Hydrol. Earth Syst. Sci.*, 19(2):951–967, February 2015. ISSN 1607-7938. doi: [10.5194/hess-19-951-2015](https://doi.org/10.5194/hess-19-951-2015). URL <https://www.hydrol-earth-syst-sci.net/19/951/2015/>.
- Wood, N. B. *Estimation of snow microphysical properties with application to millimeter-wavelength radar retrievals for snowfall rate*. Ph.D., Colorado State University, 2011. URL https://dspace.library.colostate.edu/bitstream/handle/10217/48170/Wood_colostate_0053A_10476.pdf?sequence=1&isAllowed=y.
- Wood, N. B., L’Ecuyer, T. S., Vane, D. G., Stephens, G. L., and Partain, P. Level 2c snow profile process description and interface control document. Technical Report, 2013. URL http://www.cloudsat.cira.colostate.edu/sites/default/files/products/files/2C-SNOW-PROFILE_PDICD.P_R04.20130210.pdf.
- Wood, N. B., L’Ecuyer, T. S., Heymsfield, A. J., Stephens, G. L., Hudak, D. R., and Rodriguez, P. Estimating snow microphysical properties using collocated multisensor observations. *J. Geophys. Res. Atmos.*, 119(14):8941–8961, July 2014. ISSN 2169-8996.

doi: 10.1002/2013JD021303. URL <http://onlinelibrary.wiley.com/doi/10.1002/2013JD021303/abstract>.

Wood, N. B., L'Ecuyer, T. S., Heymsfield, A. J., and Stephens, G. L. Microphysical Constraints on Millimeter-Wavelength Scattering Properties of Snow Particles. *J. Appl. Meteor. Climatol.*, 54(4):909–931, January 2015. ISSN 1558-8424. doi: 10.1175/JAMC-D-14-0137.1. URL <http://journals.ametsoc.org/doi/10.1175/JAMC-D-14-0137.1>.

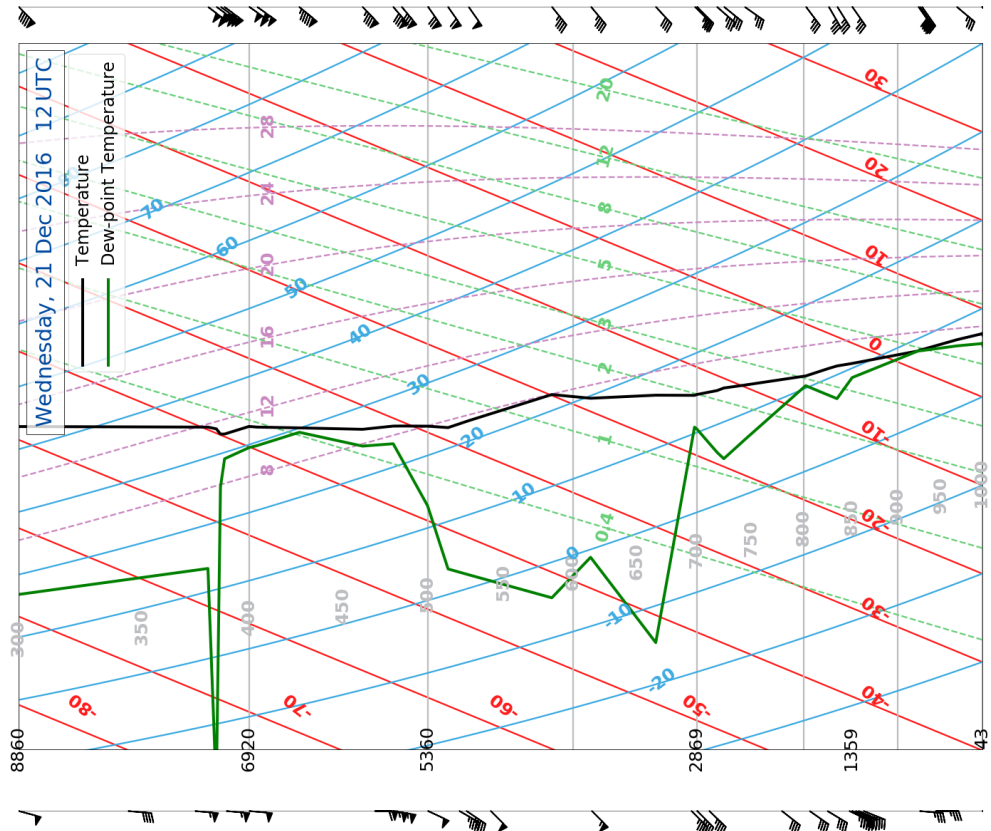
APPENDIX A: SYNOPTIC WEATHER SITUATION

A.1 SKEW-T LOG-P DIAGRAM FROM STAVANGER

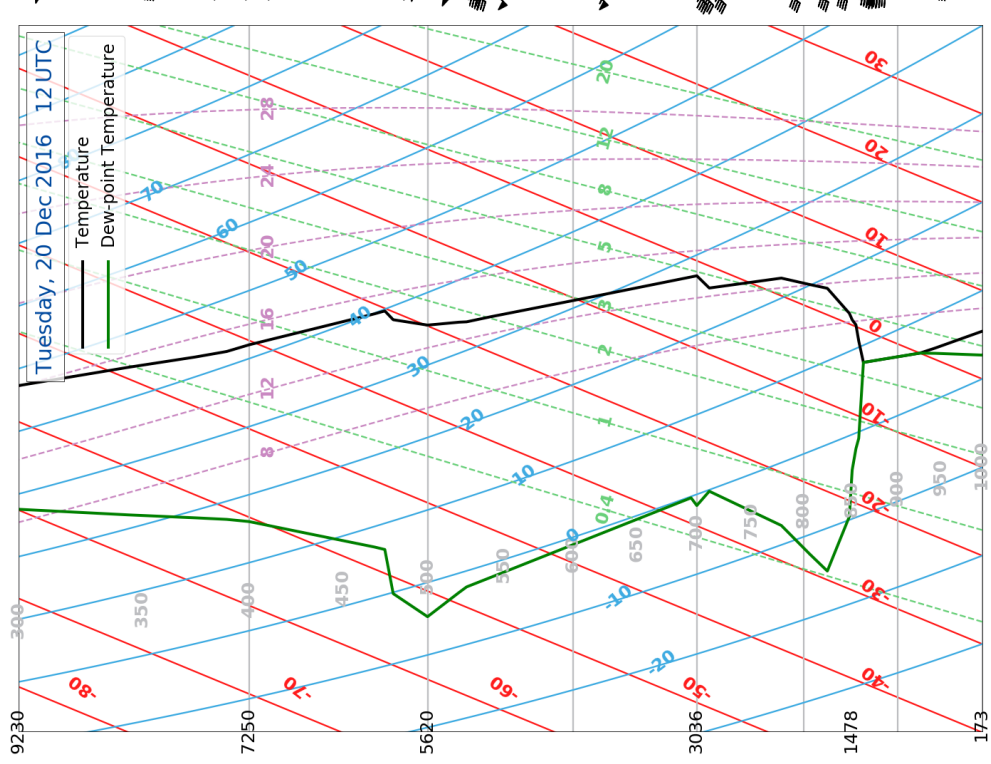
The Skew-T log-P diagram shows the observed vertical temperature and dew-point temperature at Stavanger. The data are taken from [University Wyoming \[2018\]](#) and processed in Python.

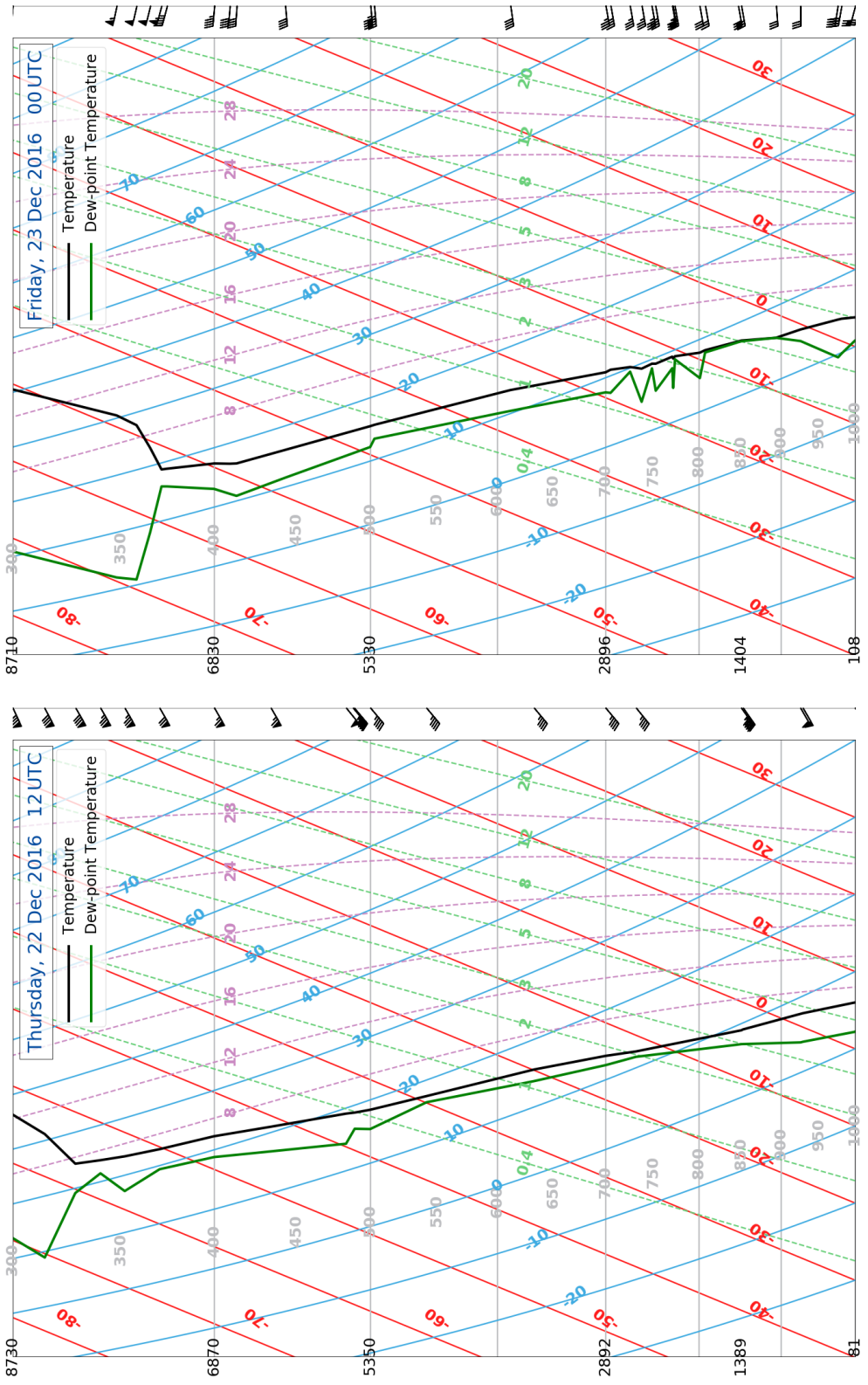
Isobars are grey lines, every 50 hPa, dry adiabats are blue (labelled in $^{\circ}\text{C}$), isotherms are red [$^{\circ}\text{C}$], water vapour mixing ratios are green, dashed in $[\text{g kg}^{-1}]$, and moist adiabats are dashed, purple lines (labelled in [$^{\circ}\text{C}$]).

(b)



(a)





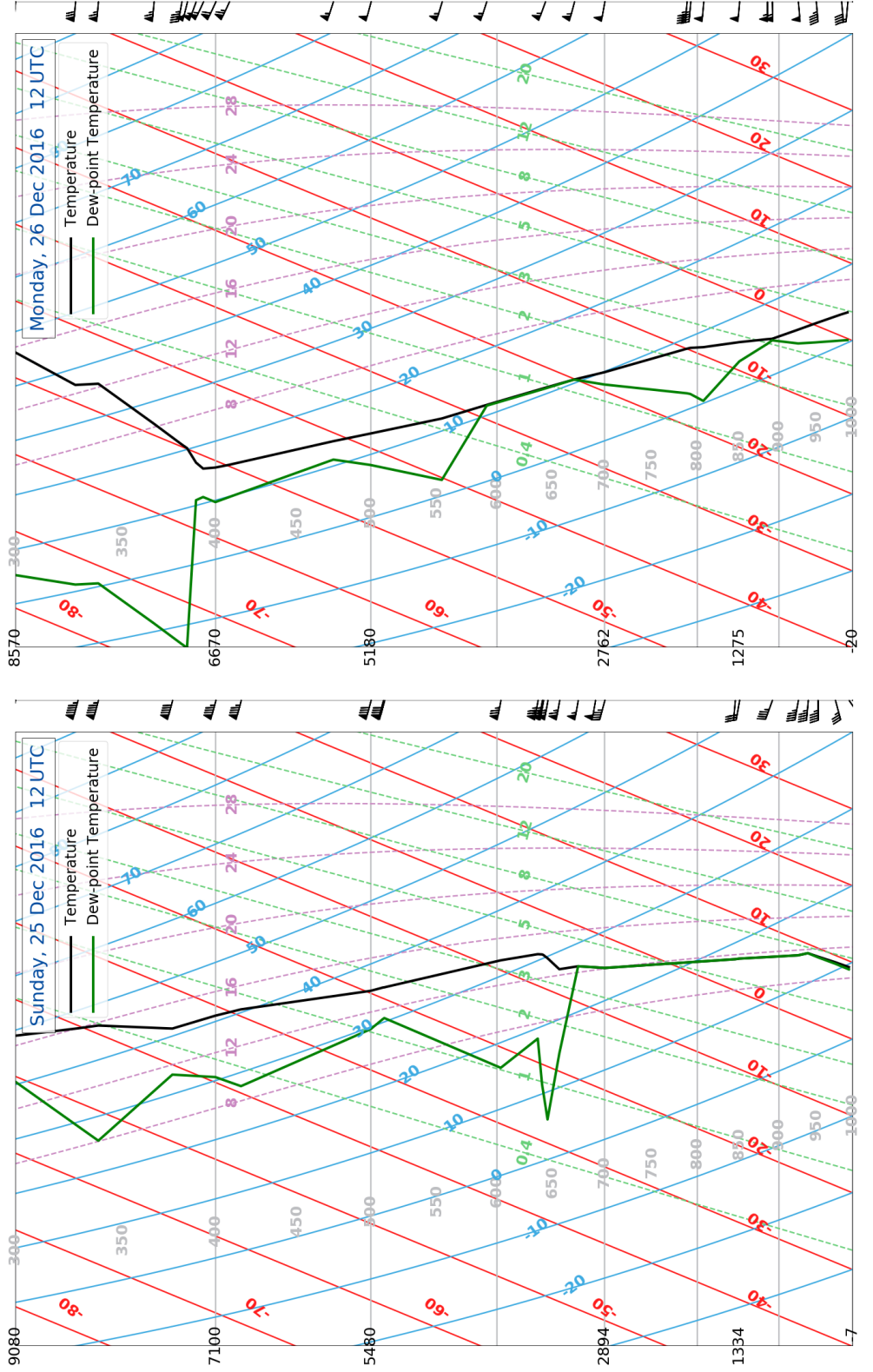


Figure A.1.1: Vertical profiles of atmospheric temperature (black) and dew-point temperature (green) during 20 December 2016 to 26 December 2016. Vertical Profiles from 24 December 2016 are missing at the webpage <http://weather.uwyo.edu/upperair/sounding.html>

APPENDIX B: FORWARD MODEL

B.1 SCATTERING MODEL

Table B.1.1: Branched 6-arm spatial particle with porosities, 2D, mass oriented scattering scheme at 24.0GHz. \mathbf{r} , particle size of the snow particle; $\mathbf{m}(\mathbf{r})$, particle mass; $\sigma_{\text{bk}}(\mathbf{r})$ and $\sigma_{\text{ext}}(\mathbf{r})$, backscattering and extinction cross-section, respectively.

\mathbf{r} [μm]	$\mathbf{m}(\mathbf{r})$ [kg]	$\sigma_{\text{bk}}(\mathbf{r})$ [m ⁻²]	$\sigma_{\text{ext}}(\mathbf{r})$ [m ⁻²]
35.27	1.68529×10^{-10}	8.85111×10^{-17}	4.85381×10^{-17}
41.73	2.79128×10^{-10}	2.00612×10^{-16}	1.28776×10^{-16}
47.87	4.21355×10^{-10}	4.792×10^{-16}	2.9959×10^{-16}
53.76	5.96809×10^{-10}	1.02733×10^{-15}	6.08871×10^{-16}
59.45	8.07074×10^{-10}	1.68272×10^{-15}	1.09633×10^{-15}
70.34	1.3368×10^{-9}	5.7444×10^{-15}	3.61096×10^{-15}
80.69	2.01798×10^{-9}	1.0899×10^{-14}	6.93961×10^{-15}
90.63	2.85939×10^{-9}	2.244×10^{-14}	1.42249×10^{-14}
100.20	3.86421×10^{-9}	3.7814×10^{-14}	2.73019×10^{-14}
109.50	5.04313×10^{-9}	7.05869×10^{-14}	5.36211×10^{-14}
118.60	6.40785×10^{-9}	1.16874×10^{-13}	9.74644×10^{-14}
127.40	7.94266×10^{-9}	1.67227×10^{-13}	1.56602×10^{-13}
144.50	1.15894×10^{-8}	3.41952×10^{-13}	4.19048×10^{-13}
160.90	1.60002×10^{-8}	7.30397×10^{-13}	1.05187×10^{-12}

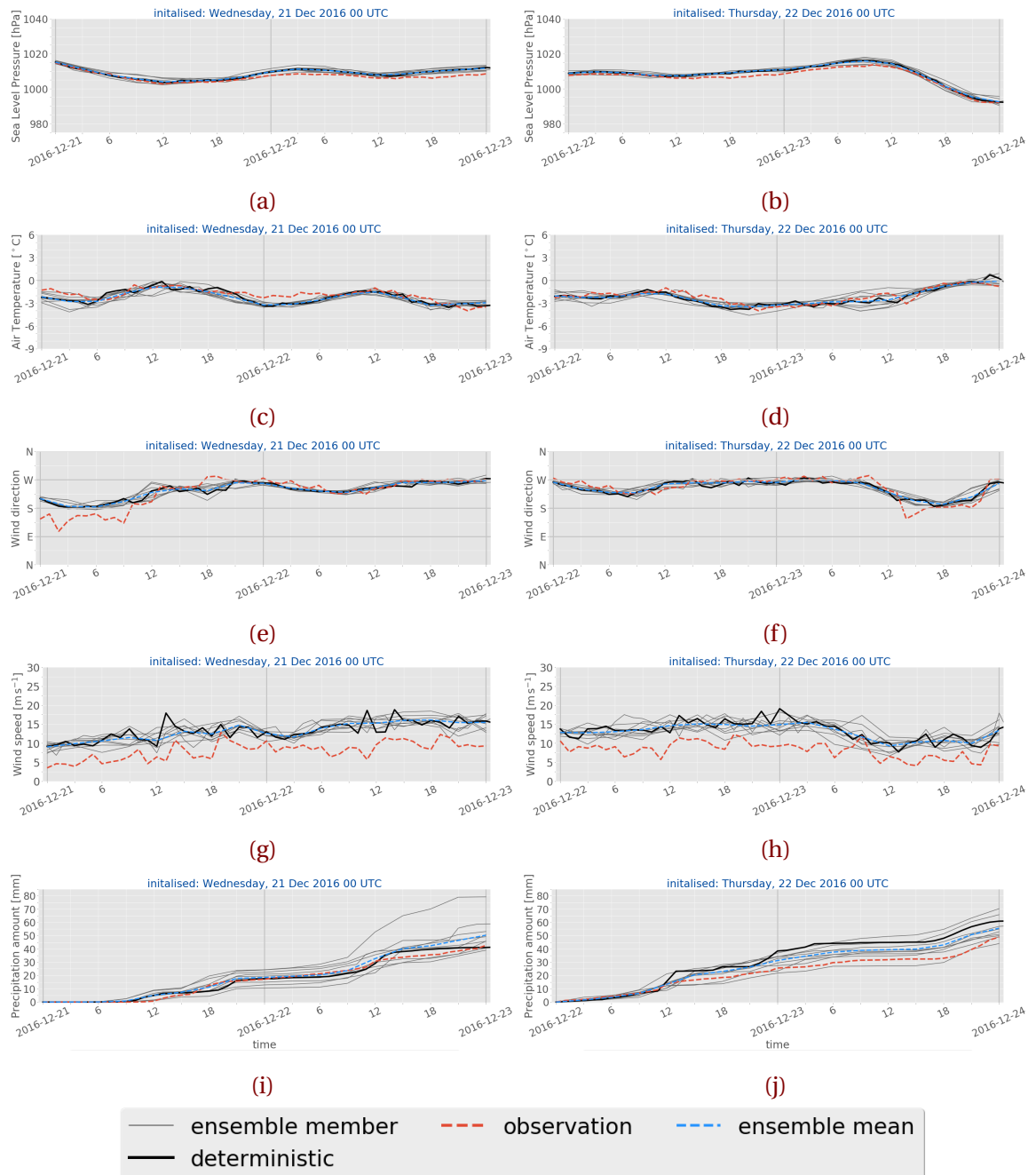
Continued on next page

Table B.1.1 Continued from previous page

r [μm]	m(r) [kg]	$\sigma_{\text{bk}}(\mathbf{r})$ [m ⁻²]	$\sigma_{\text{ext}}(\mathbf{r})$ [m ⁻²]
176.80	$2.122\,78 \times 10^{-8}$	$1.136\,38 \times 10^{-12}$	$2.003\,59 \times 10^{-12}$
192.30	$2.731\,47 \times 10^{-8}$	$2.053\,33 \times 10^{-12}$	$3.635\,31 \times 10^{-12}$
236.50	$5.081\,03 \times 10^{-8}$	$5.941\,38 \times 10^{-12}$	$1.525\,6 \times 10^{-11}$
278.10	$8.261\,54 \times 10^{-8}$	$1.577\,15 \times 10^{-11}$	$4.319\,27 \times 10^{-11}$
317.70	$1.231\,71 \times 10^{-7}$	$3.687\,19 \times 10^{-11}$	$9.719\,16 \times 10^{-11}$
355.80	$1.730\,12 \times 10^{-7}$	$6.460\,05 \times 10^{-11}$	$1.890\,57 \times 10^{-10}$
392.60	$2.324\,39 \times 10^{-7}$	$1.291\,91 \times 10^{-10}$	$3.524\,6 \times 10^{-10}$
428.20	$3.015\,77 \times 10^{-7}$	$1.752\,6 \times 10^{-10}$	$5.673\,93 \times 10^{-10}$
463.00	$3.812\,42 \times 10^{-7}$	$3.581\,77 \times 10^{-10}$	$8.763\,74 \times 10^{-10}$
496.90	$4.712\,65 \times 10^{-7}$	$5.862\,79 \times 10^{-10}$	$1.304\,17 \times 10^{-9}$
530.10	$5.721\,78 \times 10^{-7}$	$8.501\,41 \times 10^{-10}$	$1.886\,2 \times 10^{-9}$
562.60	$6.840\,02 \times 10^{-7}$	$1.045\,66 \times 10^{-9}$	$2.608\,54 \times 10^{-9}$
594.50	$8.070\,74 \times 10^{-7}$	$1.545\,14 \times 10^{-9}$	$3.681\,76 \times 10^{-9}$
625.80	$9.413\,79 \times 10^{-7}$	$1.617\,04 \times 10^{-9}$	$4.485\,78 \times 10^{-9}$
656.60	$1.087\,33 \times 10^{-6}$	$2.107\,09 \times 10^{-9}$	$5.711\,84 \times 10^{-9}$
687.00	$1.245\,46 \times 10^{-6}$	$3.315\,67 \times 10^{-9}$	$7.859\,38 \times 10^{-9}$
717.00	$1.415\,84 \times 10^{-6}$	$3.735\,98 \times 10^{-9}$	$9.508\,17 \times 10^{-9}$
746.50	$1.597\,89 \times 10^{-6}$	$4.405\,91 \times 10^{-9}$	$1.148\,24 \times 10^{-8}$
775.60	$1.792\,14 \times 10^{-6}$	$5.143\,2 \times 10^{-9}$	$1.373\,71 \times 10^{-8}$
804.40	$1.999\,28 \times 10^{-6}$	$4.212\,61 \times 10^{-9}$	$1.596\,03 \times 10^{-8}$
832.90	$2.219\,4 \times 10^{-6}$	$7.087\,5 \times 10^{-9}$	$1.904\,38 \times 10^{-8}$
861.10	$2.452\,55 \times 10^{-6}$	7.606×10^{-9}	$2.170\,23 \times 10^{-8}$
888.90	$2.697\,84 \times 10^{-6}$	$9.616\,05 \times 10^{-9}$	$2.524\,76 \times 10^{-8}$
916.50	$2.957\,03 \times 10^{-6}$	$1.201\,08 \times 10^{-8}$	$2.913\,29 \times 10^{-8}$
943.80	$3.229\,22 \times 10^{-6}$	$1.293\,26 \times 10^{-8}$	$3.309\,11 \times 10^{-8}$
970.80	$3.514\,37 \times 10^{-6}$	$1.532\,46 \times 10^{-8}$	$3.825\,95 \times 10^{-8}$
997.60	$3.813\,53 \times 10^{-6}$	$1.326\,87 \times 10^{-8}$	4.344×10^{-8}

APPENDIX C: RESULTS

C.1 48 h SURFACE OBSERVATIONS AND MEPS FORECASTS



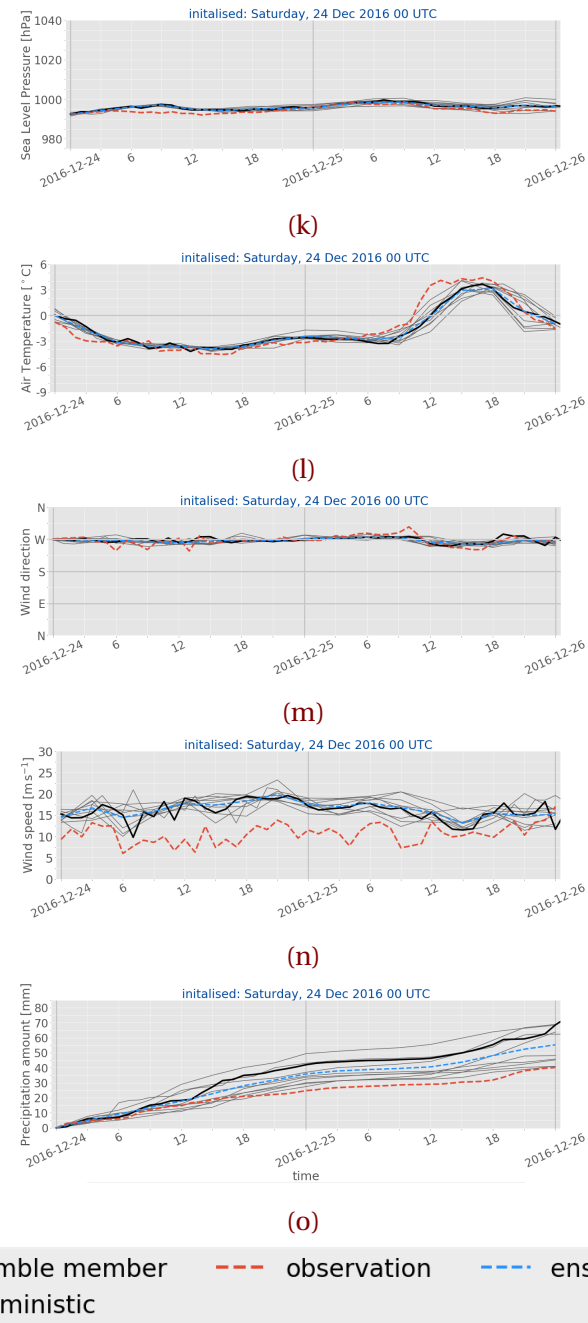


Figure C.1.1: (*Continued from previous page.*) Initialisations for 22 December 2016 (k, l, m, n, o)

C.2 MEAN ERROR AND MEAN ABSOLUTE ERROR

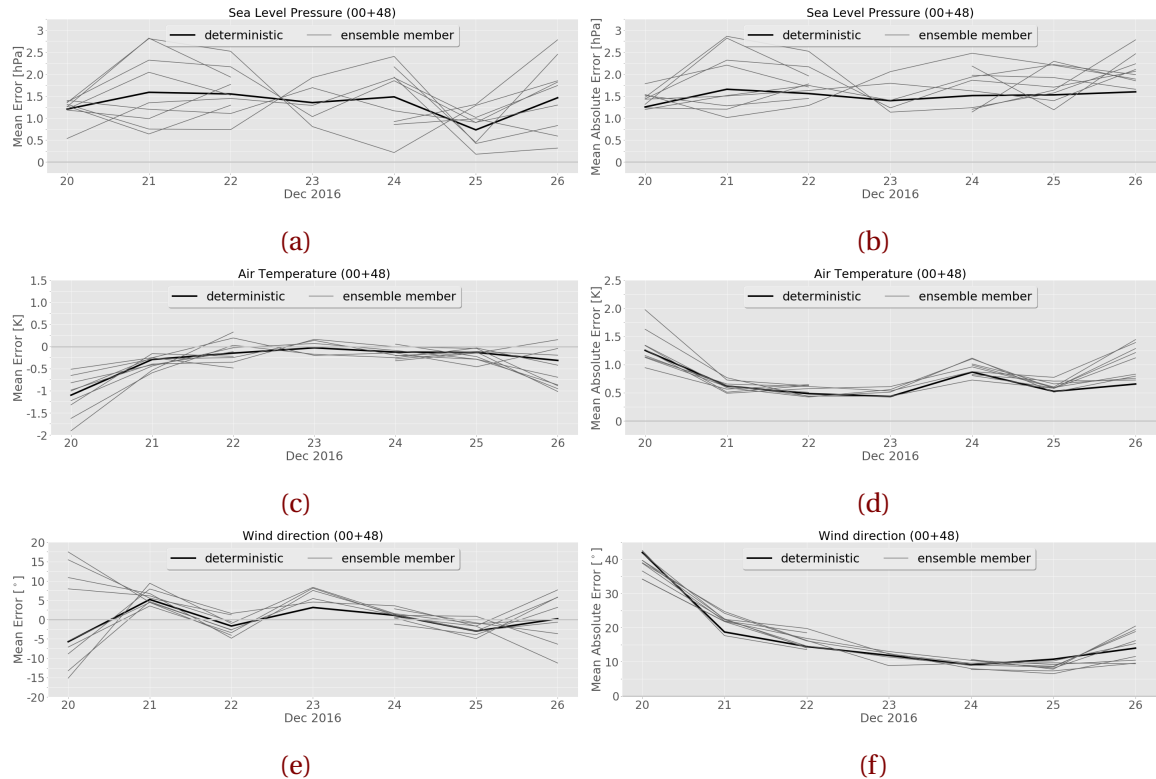


Figure C.2.1: Mean error (a, c, e, g, i) and mean absolute error (b, d, f, h, j) of surface variables for all ten ensemble members at Haukeliseter, initialisations at 0 UTC, valid for 48 h. From top to bottom, sea level pressure (a, b), 2 m air temperature (c, d), 10 m wind direction (e, f).

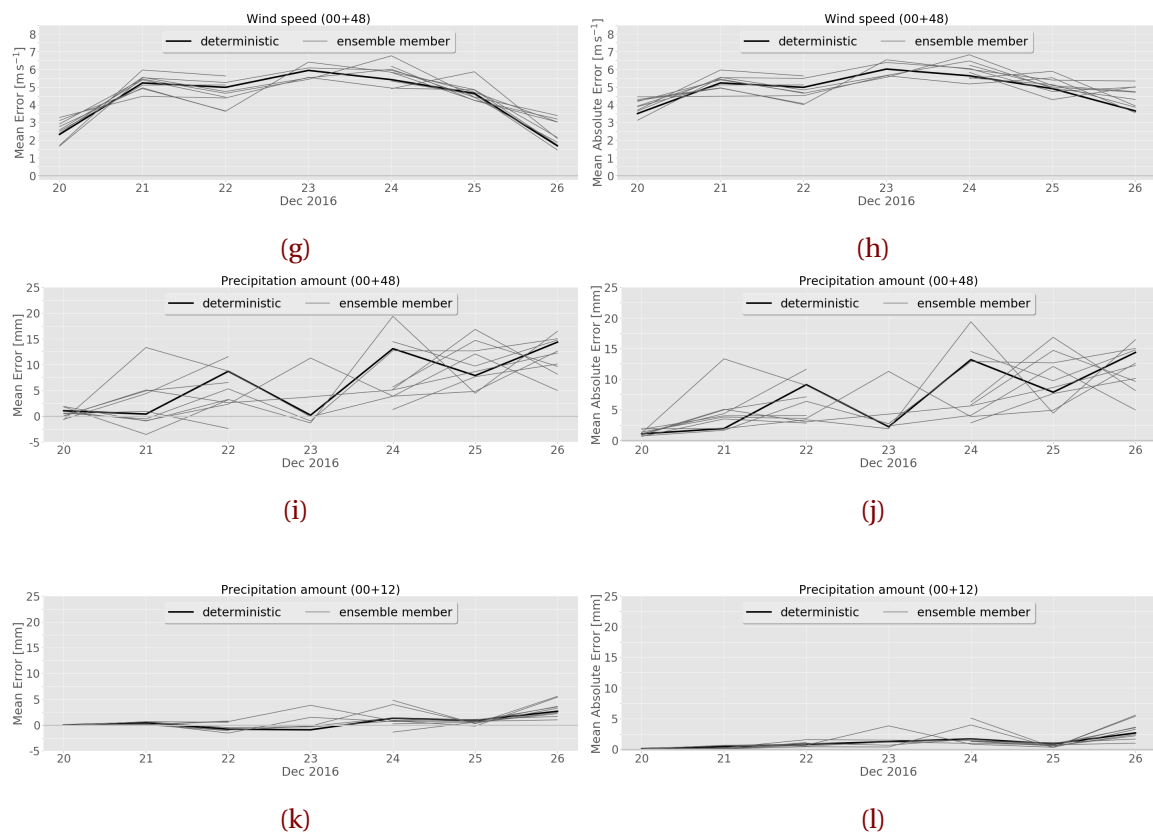


Figure C.2.1: (Continued from previous page.) , 10 m wind speed (g, h), precipitation accumulation for 48 h (i, j) and 12 h surface accumulation (k, l).

C.3 HOURLY AVERAGES ENSEMBLE MEMBER ZERO AND ONE

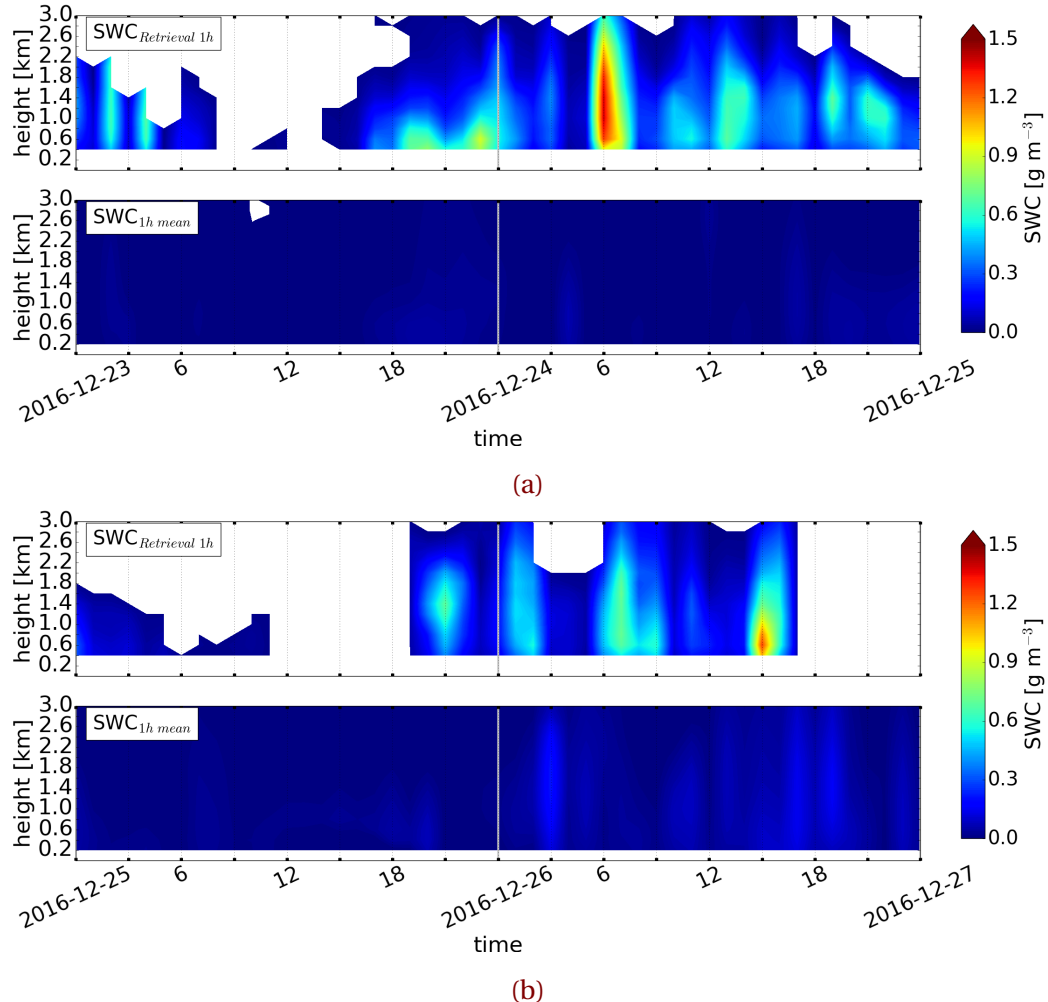
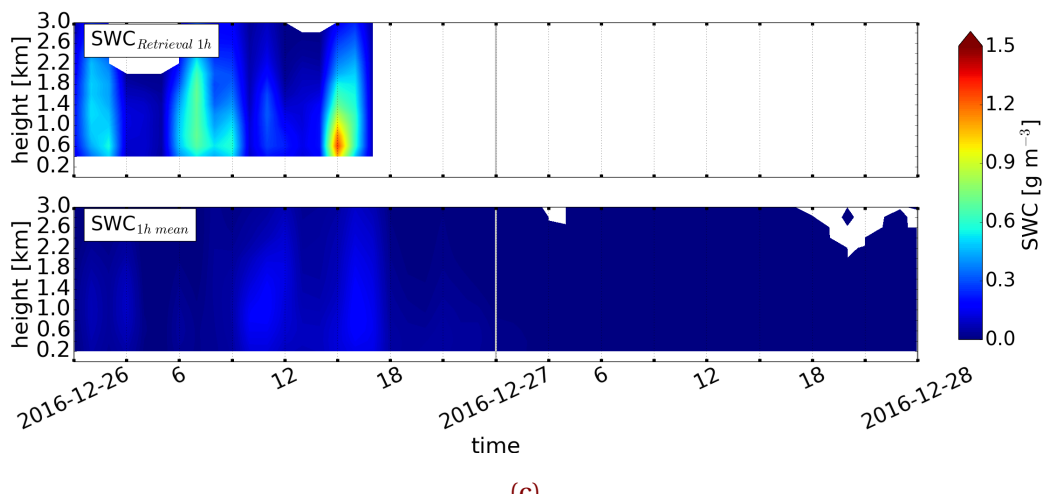


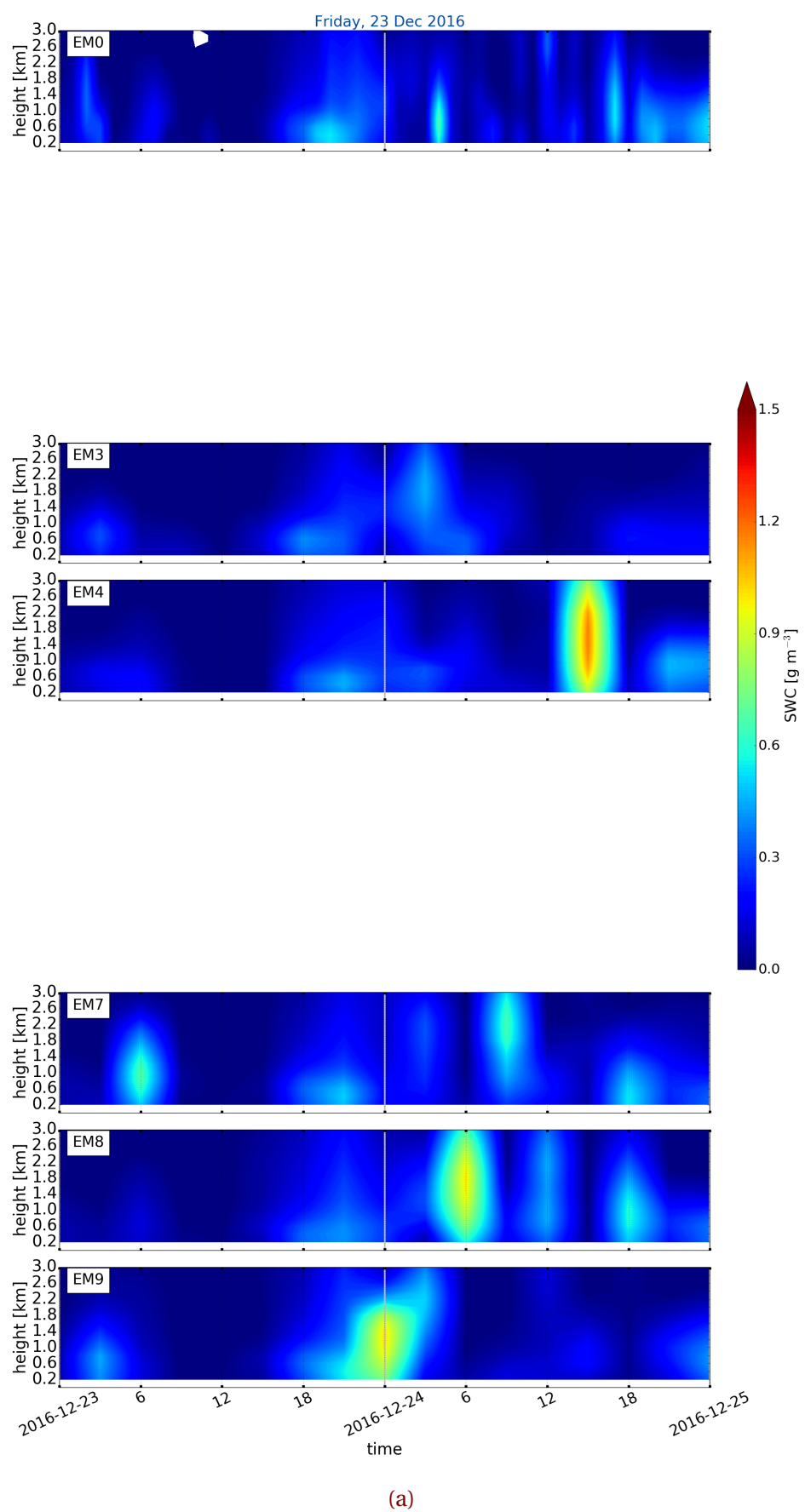
Figure C.3.1: Upper panel: hourly averaged retrieved SWC, lower panel instantaneous hourly averaged SWC forecast of deterministic and first ensemble member. Initialised 23 December 2016 and 25 December 2016 at 0 UTC.



(c)

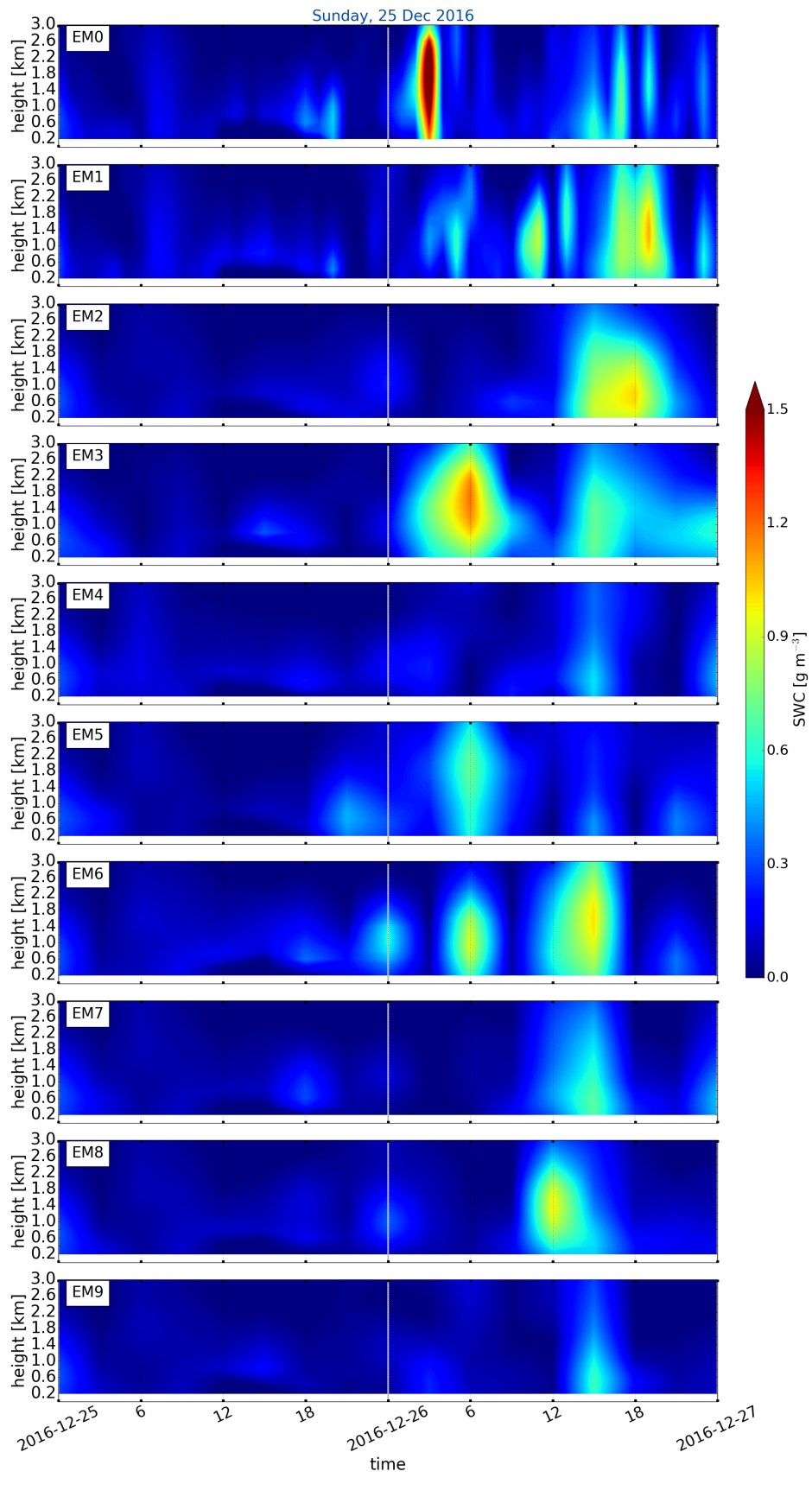
Figure C.3.1: (Continued from previous page.) Initialised 26 December 2016 at 0 UTC.

C.4 VERTICAL SWC - ENSEMBLE MEMBER 0 TO 9



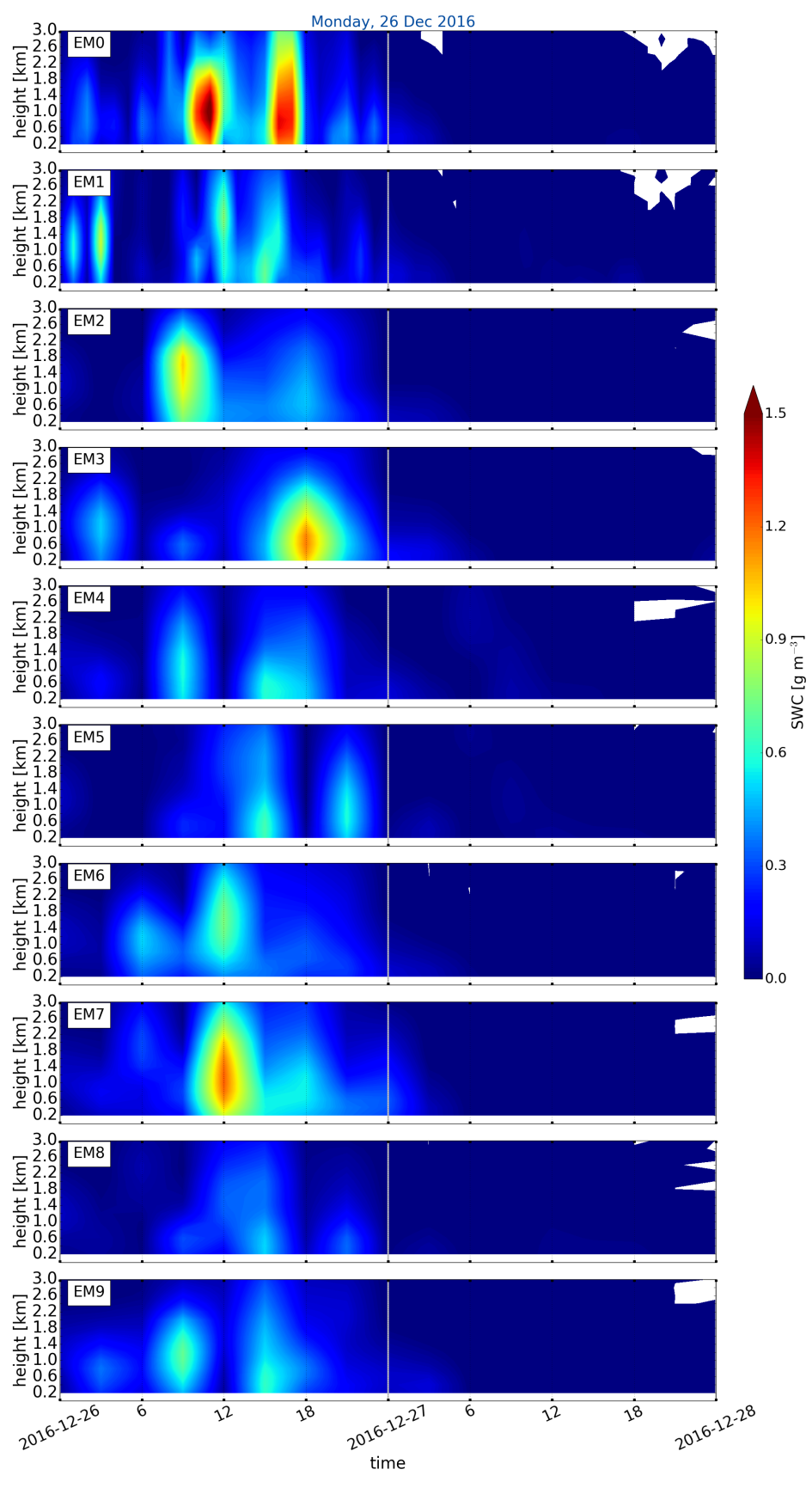
(a)

Figure C.4.1: Vertical SWC of each individual ensemble member from 0 to 9 forecast for 48 h. Initialised 23 December 2016 at 0 UTC.



(b)

Figure C.4.1: (Continued from previous page.) Initialised 25 December 2016 at 0 UTC.



(c)

Figure C.4.1: (Continued from previous page.) Initialised 26 December 2016 at 0 UTC.